Astronomy Letters, Vol. 28, No. 10, 2002, pp. 651–655. Translated from Pis'ma v Astronomicheskiĭ Zhurnal, Vol. 28, No. 10, 2002, pp. 723–727.

The Halo-to-Disk Mass Ratio in Late-Type Galaxies

A. V. Khoperskov*

Sternberg Astronomical Institute, Universitetskiĭ pr. 13, Moscow, 119992 Russia

Received April 14, 2001; in final form, May 15, 2002

Abstract—Dynamical modeling of stellar disks without bulges is used to derive the dependence of the central stellar radial-velocity dispersion on the dark-halo mass. A sample of late-type galaxies with known central stellar velocity dispersions and maximum gas rotation velocities was drawn from the LEDA database. The sample-averaged ratio of the halo mass within four radial disk scale lengths to the disk mass is 80%. Objects whose halo mass can be a factor of 2 or more larger than the disk mass were identified.
© *2002 MAIK "Nauka/Interperiodica".*

Key words: *late-type galaxies, dynamical modeling, halo mass.*

INTRODUCTION

The mass of the disk component of a spiral galaxy (M_d) is one of the fundamental parameters that determine the physics of the system. The total mass of a galaxy within a fixed radius can be estimated from the rotation curve of the gaseous subsystem. One of the ways of decomposing a galaxy into a disk and spherical subsystem is by analyzing the radial distribution of stellar velocity dispersion and constructing dynamical models of stellar disks at the threshold of gravitational stability (Bottema and Geritsen 1997 ; Khoperskov *et al.* 2001; Zasov and Khoperskov 2002).

The radial dependence of stellar velocity dispersion in the disk is known for a small number of objects; therefore, it is of interest to estimate the halo mass based on the observed central velocity dispersion c_obs exclusively. Such estimates are, in principle, possible if the galaxy lacks a bulge. In this case c_obs can be attributed to the disk component and late-type galaxies (Sc, Sd, and Sm) can be used to this end.

RATIO OF THE CENTRAL STELLAR VELOCITY DISPERSION TO THE MAXIMUM ROTATION VELOCITY

Let us assume that in stellar disks, the stellar velocity dispersion is equal to the minimum level required for gravitational stability (Toomr e 1964). This analysis is based on the dependence of the ratio of the dispersion of radial velocities $c_r(r=0)$ to the maximum rotation velocity $\beta \equiv c_r(0)/V^{(m)}$ on the halo mass fraction $\mu = M_\mathrm{h}/M_\mathrm{d}$ obtained via dynamic modeling (numerical integration of equations of motion for gravitationally interacting N bodies that make up a disk). We use the quasi-isothermal halo model with volume density

$$\varrho_\mathrm{h} = \frac{\varrho_0}{1+(r/a)^2}, \qquad (1)$$

where ϱ_0 is the central density, r is the distance from the disk center, and a is the halo scale length. The halo mass M_h was computed within radius $r \le 4L$, which, as a rule, corresponds to the optical radius of the disk (van der Kruit and Searle 1981).

Surface density in the disk is described by the following exponential law:

$$\sigma(r) = \sigma(0)\exp(-r/L), \qquad (2)$$

with radial scale length L. This law follows from the observed radial surface brightness profiles of stellar disks computed assuming that the mass-to-luminosity ratio remains constant at all radii (Baggett *et al.* 1998).

The rotation curves of galaxies without large bulges have, as a rule, an extended portion of monotonic increase in rotation velocity in the region $r \lesssim 2L$, which can be easily explained by the mass distribution in disk (2) provided that the condition $a \gtrsim L$ is satisfied. Another characteristic feature of the rotation curves is an extended plateau in the region $r \gtrsim 2L$, which can often be seen well beyond the optical radius. If $a \gtrsim 3L$ and $M_\mathrm{h} = M_\mathrm{d}$, then circular rotation velocity V_c is not constant in the region $r = 2L$–$8L$ but increases with radius (Fig. 1a). This effect becomes stronger with increasing halo mass μ (Fig. 1b). Thus for bulgeless models to have a circular velocity plateau, we must restrict ourselves to $a = (1\text{–}3) \times L$. With the fractional mass $M_\mathrm{h}/M_\mathrm{d}$

*E-mail: khopersk@sai.msu.ru

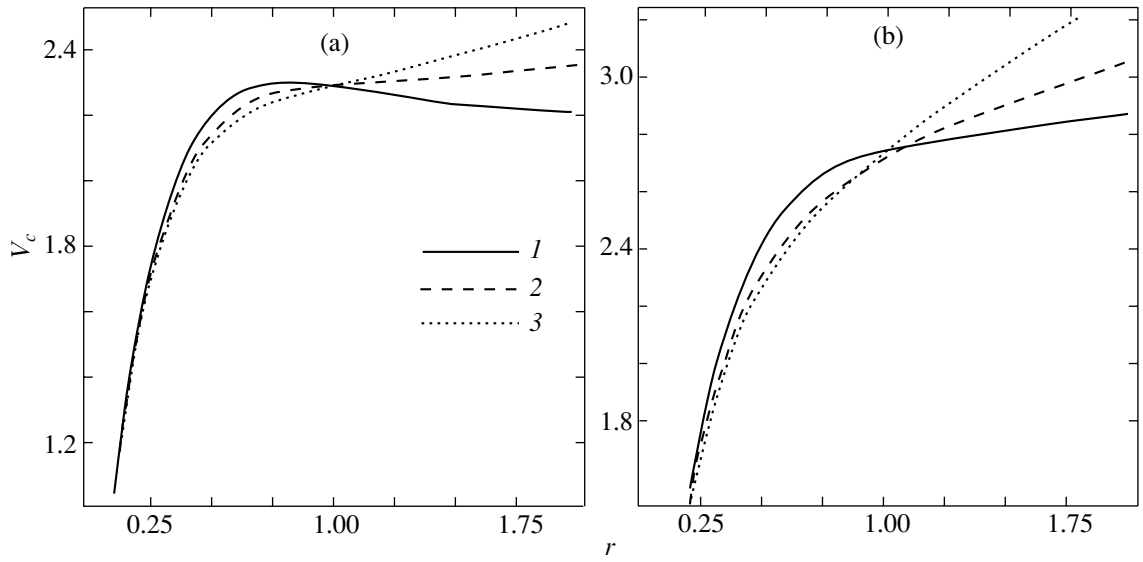

Fig. 1. Radial dependence of circular rotation velocity $V_c(r)$ in models with a disk (2) and vertical scale height $h = 0.2L$ for $L = 0.25$ and a halo with different values of parameters a and M_h for $M_\mathrm{h} = M_\mathrm{d}$ (a): (*1*) $a = 2L$, (*2*) $a = 3L$, (*3*) $a = 4L$; (b) Same for $M_\mathrm{h} = 2M_\mathrm{d}$.

being fixed, the role of the halo in the central region decreases with increasing a. As a result, the disk at the threshold of gravitational stability has higher velocity dispersion c_r.

Morozov (1981) found the ratio of stellar velocity dispersion to rotation velocity $V_\star$ to decrease with increasing halo mass fraction at the disk periphery.

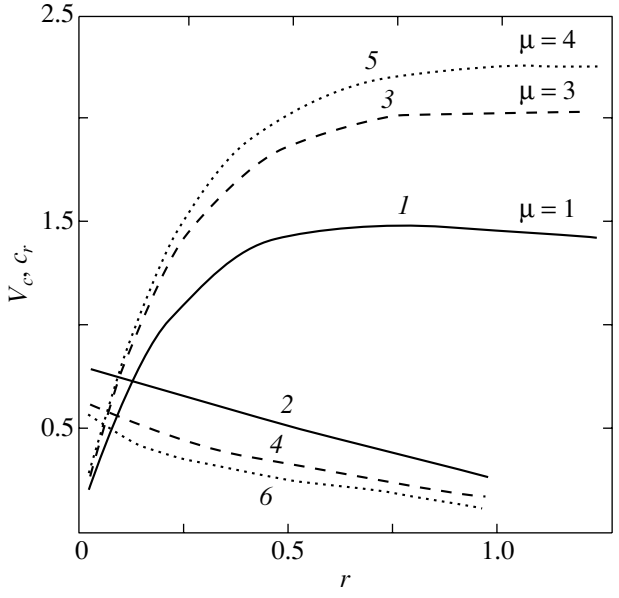

Fig. 2. Radial dependences of circular rotation velocity V_c and dispersion of radial velocities c_r for different μ according to the results of dynamical modeling: for $\mu = 1$ dependence (*1*) V_c, (*2*) c_r; for $\mu = 3$ curve (*3*) V_c, (*4*) c_r; for $\mu = 4$ dependence (*5*) V_c, (*6*) c_r.

A similar effect is true for the central region (Fig. 2). Figure 3 shows the dependence of $\beta(\mu)$ based on the results of dynamic modeling. The rotation velocity of the stellar component $V_\star$ is smaller than the circular velocity V_c, and this difference increases appreciably in the case of a low-mass halo (see Fig. 3). Therefore, the dependence $\beta(\mu)$ computed using circular rotation velocity should be preferred in making a comparison with observational data.

Function $\beta(\mu)$ depends on the halo scale length a (see Fig. 3). At constant μ the ratio $c_r(0)/V_c^{(m)}$ increases with a. Therefore, inferring μ from known β using curve *1* in Fig. 3 (the case $a = L$) should give a lower estimate of the halo mass. The $\beta(\mu)$ dependences in the case $a > L$ yield overestimated μ, thereby underestimating the disk mass.

When comparing the results with observational data we obtain a lower boundary for the halo mass fraction μ because stellar velocity dispersion is greater in the bulge than in the disk.

We now assume that the maximum rotation velocity $V_c^{(m)}$ is equal to the maximum velocity of rotation of gas measured either at optical wavelengths ($V_\mathrm{opt}^{(m)}$ (Hα)) or based on radio observations ($V_\mathrm{rad}^{(m)}$ (HI)); these values are provided by the LEDA electronic catalog. In addition, the catalog also gives the maximum rotation velocity $V_\mathrm{rot}^{(m)}$ reduced to a single system and the doubled rotation velocity corrected for the inclination of the galaxy $\Delta V^{(m)}$. We selected from the LEDA catalog a sample of late-type galaxies with

morphological types $t \geq 4$[1] according to this catalog with known central stellar velocity dispersion $c_{\rm obs}$ and maximum velocity of gas rotation $V_{\rm gas}^{(m)}$. To determine the relation between $c_{\rm obs}$ and $c_r(0)$, let us assume that the dispersion of azimuthal velocities is equal to $c_\varphi = c_r$ and that of vertical velocities, to $c_z = 0.6c_r$. Given the inclination of the stellar disk i, we obtain $c_r(0) = c_{\rm obs}/\sqrt{0.36\cos^2(i) + \sin^2(i)}$. The β parameter inferred from observational data allows the fractional halo mass to be estimated using relation *1* in Fig. 3.

Note the effect of systematic factors on the halo masses inferred as described above.

(1) In the absence of a massive and/or concentrated bulge the maximum of rotation velocity is achieved at $r > 2L$. Note that with increasing halo mass the maximum shifts toward the periphery of the disk. In a number of cases the observed rotation velocity used by the researchers refers to the regions located closer to the center, i.e., yields an overestimated velocity dispersion to rotation velocity ratio and, consequently, an underestimated halo mass.

(2) In the presence of even a small bulge the observed parameter $c_{\rm obs}$ imposes an upper limit on the velocity dispersion of the disk component and we thus again obtain a lower estimate for the halo mass fraction.

The uncertain factors may include the central depression of the stellar density in the disk (Barabanov and Zasov 1979). Moreover, the central stellar velocity dispersion may characterize the nuclear region, which possibly harbors a black hole (Merritt and Ferrarese 2001). If parameter $c_{\rm obs}$ from the LEDA database obviously referred to the centermost nuclear region, we either excluded the galaxy from consideration or adopted a $c_{\rm obs}$ value taken at a greater galactocentric distance. Thus, e.g., the LEDA database gives for the $r < 3''$ region in M33 a velocity dispersion of $c_{\rm obs} = 21$ km s^{-1} (Kormendy and McClure 1993). For bulge stars, $c_{\rm obs} = 34$ km s^{-1} (Minniti 1996), whereas according to the observations of star clusters in the disk outside the central region, $c_{\rm obs} = 25$ km s^{-1} (Schommer *et al.* 1991). We can therefore assume that $c_{\rm obs} = 25$–34 km s^{-1} at the center for the disk component, yielding $\beta = 0.26$–0.36 for $V^{(m)} = 108$ km s^{-1} and $i = 55°$. We thus have $\mu = 2.3$–3.5 (see Fig. 3). This result as to the presence of a massive halo in M33 agrees with the model of Corbelli and Salucci (2000), according to which the contribution of the halo to circular rotation velocity begins to dominate starting from a galactocentric radius of 2.8 kpc and the halo mass within $r < 4L \simeq 5$ kpc exceeds more than twice the mass of the disk $M_{\rm d}$.

[1]Parameter t corresponds to morphological class as follows: $t = 2$—Sab galaxies, $t = 4$—Sbc galaxies.

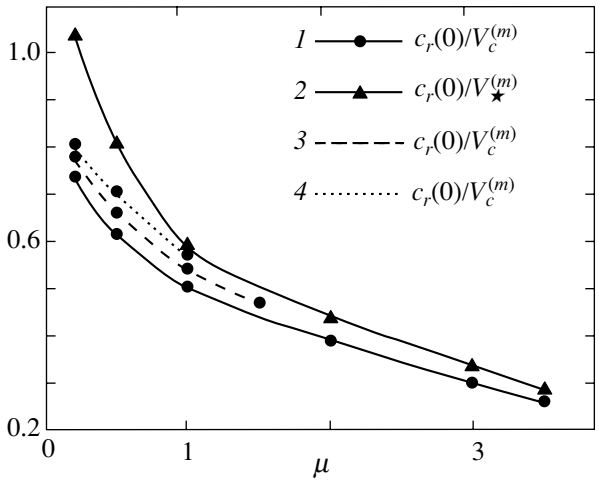

Fig. 3. The ratio of the dispersion of radial velocities at the disk center $c_r(0)$ to the maximum circular radial velocity $V_c^{(m)}$ (*1*) and maximum velocity of stellar rotation $V_\star^{(m)}$ (*2*) for different halo mass fractions $m = M_{\rm h}/M_{\rm d}$ with $a = L$ based on the results of the dynamical modeling of the disk without allowance for the bulge; (*3*) for models with $a = 2L$; (*4*) for $a = 3L$.

ESTIMATION OF THE HALO MASS

There are a total of 89 objects with known stellar velocity dispersions and maximum velocities of gas rotation. We do not consider here the galaxies with $\beta > 0.9$, because the relation shown in Fig. 3 is evidently inapplicable to such objects. Large β may be due to the presence of an appreciable bulge, as, e.g., in NGC 628, 4254, 4536, and 5480 (Baggett *et al.* 1998), preventing halo mass estimates for these objects based on central velocity dispersion exclusively. Figure 4 shows the distributions of fractional halo masses μ of galaxies. The mean values are equal to $\langle c_r(0)/V_{\rm rad}^{(m)}\rangle = 0.54$, $\langle c_r(0)/V_{\rm opt}^{(m)}\rangle = 0.55$, and $\langle c_r(0)/V_{\rm rot}^{(m)}\rangle = 0.56$, yielding an average fractional halo mass of $\langle\mu\rangle \simeq 0.8$.

Other galaxies can be singled out, in addition to the M33 galaxy considered above, which may possess rather massive halos with masses exceeding that of the disk by a factor of two and more. Let us consider such objects in more detail.

(1) For NGC 2998, we obtain, according to LEDA data, $\beta = 0.40$. The galaxy has a very small bulge and therefore is disk dominated in its central part. The observed central velocity dispersion $c_{\rm obs} = 50$–70 km s^{-1} $\simeq 60$ km s^{-1} can be attributed to the disk component (Whitmore *et al.* 1984). The rotation curve is flat at the periphery of the galaxy, and, given the inclination angle of $i = 63°$, we obtain $V^{(m)} \simeq 213$ km s^{-1}. These data allow estimates $\beta = 0.3$ and $\mu = 3$.

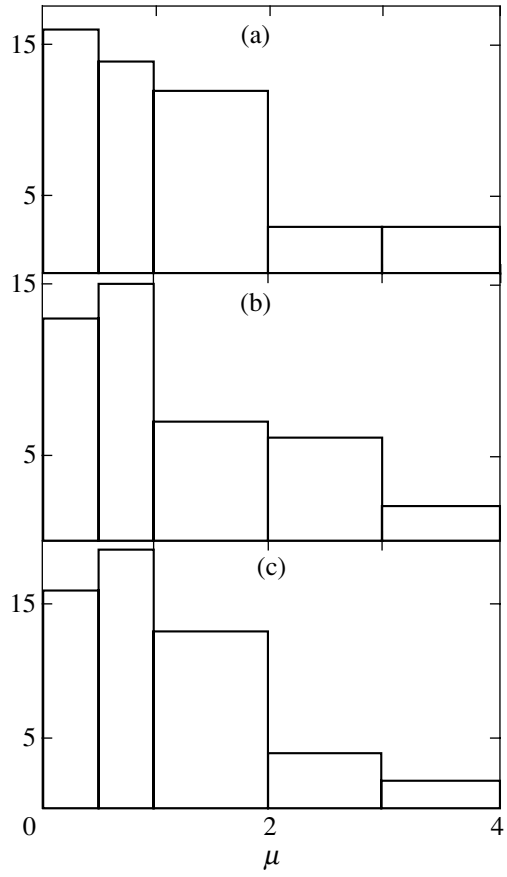

Fig. 4. The distribution of fractional halo masses μ of late-type galaxies ($t \geq 4$) computed using $V_{\rm rad}^{(m)}$ (a), $V_{\rm opt}^{(m)}$ (b), and $V_{\rm rot}^{(m)}$ (c).

(2) The effective bulge radius of NGC 3938, which is equal to $r_{\rm e} = 4''.9$, is significantly smaller than the radial disk scale length $L = 39''.7$ (Baggett *et al.* 1998). We obtain, according to LEDA data, $\beta = 0.28$ ($c_{\rm obs} = 30$ km s^{-1}, $i = 13°$, $V^{(m)} \simeq 170$ km s^{-1}). If we adopt, in line with Bottema *et al.* (1988), the inclination $i = 10°$ for this galaxy, the rotation velocity may be as high as 220 km s^{-1}. The $c_{\rm obs} = 30$ km s^{-1} (LEDA) value does not refer to the center proper, where $c_{\rm obs} = 40$–45 km s^{-1} in the bulge region ($r < 5''$). Given the extreme values, we obtain $\beta = 0.28$–0.44. The mass of the halo can thus be estimated to be within the $\mu = 1.6$–3 interval.

(3) The NGC 5170 galaxy is observed virtually edge-on ($i < 86°$) and LEDA data formally yield $\beta = 89/250 = 0.35$. The observed stellar velocity dispersions refer to the central region $r < 0.3L$ but lie beyond the bulge region. Bottema *et al.* (1987) allowed for the contribution to $c_{\rm obs}$ of the rotating matter located along the line of sight and inferred the radial velocity dispersion at the center of the galaxy $c_r(0) = 75$–115 km s^{-1}. As a result, we have $\beta = 0.3$–0.46, which is indicative of a sufficiently massive halo $\mu = 1.5$–3.

(4) Photometric decomposition of the NGC 7541 galaxy yields no bulge (Baggett *et al.* 1998); however, the rotation curve is not inconsistent with the galaxy having a bulge (Kyazumov 1980). In view of this, the $\beta = 0.32$ value inferred from LEDA data suggests the possibility of a very massive halo.

The fact that such an approach allows one to obtain realistic mass estimates may be proved by applying it to the objects for which dynamical models have been constructed, as in the case of NGC 3198 (Khoperskov *et al.* 2001). For this galaxy, stellar velocity dispersion is known out to great galactocentric distances (Bottema 1988). According to the LEDA catalog, $c_{\rm obs} = 65$ km s^{-1} and $V^{(m)} = 158$ km s^{-1}, yielding $\beta = 0.43$ and $\mu = 1.7$. For the disk component we can adopt $c_{\rm obs} = 52$ km s^{-1} (Bottema 1988), implying $\beta = 0.34$ and, consequently, $\mu = 2.5$. These estimates agree well with the halo mass estimated by constructing a dynamical model of NGC 3198 $\mu = 2.1$ (Khoperskov *et al.* 2001).

Consider, for comparison, a sample of galaxies with $2 \leq t \leq 4$, i.e., of earlier types, which rather often exhibit appreciable bulges. Restricting again our analysis to the objects that obey the condition $\beta < 0.9$, we have, on the average for the sample, $\langle c_r(0)/V^{(m)} \rangle = 0.64$ (87 objects), $\langle c_r(0)/V_{\rm opt}^{(m)} \rangle = 0.61$ (46 objects), and $\langle c_r(0)/V_{\rm rad}^{(m)} \rangle = 0.64$ (84 objects). We cannot formally use the criterion shown in Fig. 3, because the presence of a bulge may change appreciably the relation in question. The objects considered also include the NGC 891 galaxy, whose parameter μ was determined via dynamical modeling, which yielded $\mu = 1.8$ (Khoperskov *et al.* 2001). In this case we have $c_r(0)/V_{\rm opt}^{(m)} = 0.53$ and $\mu = 0.9$ according to the LEDA database, which is indicative of large errors of mass estimates based on central velocity dispersion for galaxies with massive bulges. However, even in this case we can single out four objects (NGC 1353, 4565, 7171, and 7217) where the mass of the halo may exceed significantly that of the stellar disk.

CONCLUSIONS

For bulgeless disks at the threshold of gravitational stability, the ratio of stellar velocity dispersion to the maximum rotation velocity decreases with increasing halo mass fraction $\mu = M_{\rm h}/M_{\rm d}$. It was found for a sample of late-type galaxies with known central

line-of-sight velocity dispersions and maximum rotation velocities that the halo mass is, on the average, comparable to the disk mass within four radial disk scale lengths, which correspond approximately to the optical radius. This result should be considered a lower estimate for the halo mass. The low ratios of dispersions of radial velocities of stars at the disk center to the maximum velocity of gas rotation ($c_r/V^{(m)} \lesssim 0.4$) may provide further evidence of massive halos in S-galaxies.

ACKNOWLEDGMENTS

I am grateful to D.V. Bizyaev, A.V. Zasov, and N.V. Tyurina for their assistance. Special thanks are due to the team of the LEDA electronic catalog of the Observatoire de Lyon (France) for providing access to the extragalactic database. This work was supported by the Russian Foundation for Basic Research (grant no. 01-02-17597) and Federal Research and Technology Program "Research and Development in Priority Fields of Science and Technology" (contract no. 40.022.1.1.1101 of February 1, 2002).

REFERENCES

1. W. E. Baggett, S. M. Baggett, and K. S. J. Anderson, Astron. J. **116**, 1626 (1998).
2. A. V. Barabanov and A. V. Zasov, Astron. Zh. **56**, 252 (1979) [Sov. Astron. **23**, 138 (1979)].
3. R. Bottema, Astron. Astrophys. **197**, 105 (1988).
4. R. Bottema and J. P. E. Gerritsen, Mon. Not. R. Astron. Soc. **290**, 585 (1997).
5. R. Bottema, P. C. van der Kruit, and K. C. Freeman, Astron. Astrophys. **178**, 77 (1987).
6. E. Corbelli and P. Salucci, Mon. Not. R. Astron. Soc. **311**, 441 (2000).
7. A. V. Khoperskov, A. V. Zasov, and N. V. Tyurina, Astron. Zh. **78**, 213 (2001) [Astron. Rep. **45**, 180 (2001)].
8. J. Kormendy and R. D. McClure, Astron. J. **105**, 1793 (1993).
9. G. A. Kyazumov, Pis'ma Astron. Zh. **6**, 398 (1980) [Sov. Astron. Lett. **6**, 220 (1980)].
10. P. C. van der Kruit and L. Searle, Astron. Astrophys. **95**, 105 (1981).
11. D. Merritt and L. Ferrarese, Astrophys. J. **547**, 140 (2001).
12. D. Minniti, Astron. Astrophys. **306**, 715 (1996).
13. A. G. Morozov, Astron. Zh. **58**, 734 (1981) [Sov. Astron. **25**, 421 (1981)].
14. R. A. Schommer, C. A. Christian, N. Caldwell, *et al.*, Astron. J. **101**, 873 (1991).
15. A. Toomre, Astrophys. J. **139**, 1217 (1964).
16. B. C. Whitmore, V. C. Rubin, and W. K. Ford, Astrophys. J. **287**, 66 (1984).
17. A. V. Zasov and A. V. Khoperskov, Astron. Zh. **79**, 195 (2002) [Astron. Rep. **46**, 173 (2002)].

Translated by A. Dambis

Astronomy Letters, Vol. 28, No. 10, 2002, pp. 656–659. Translated from Pis'ma v Astronomicheskiĭ Zhurnal, Vol. 28, No. 10, 2002, pp. 728–731.

WSRT Observations of the Quasar OH 471

N. S. Nesterov[1], A. E. Volvach[1*], and S. V. Pogrebenko[2]

[1] *Crimean Astrophysical Observatory, Katsiveli, Crimea, 98688 Ukraine*

[2] *Joint Institute for VLBI in Europe (JIVE), Dwingeloo, the Netherlands*

Received February 21, 2002

Abstract—The 325-MHz observations of the quasar OH 471 ($z = 3.4$) in 1985–1996 revealed variability of its radio emission. Over this period, its radio flux density increased by a factor of 1.6. A steep-spectrum radio source was identified 2.′5 north of the quasar. Its radio flux density is 1.46 mJy at 5 GHz and 14.5 mJy at 350 MHz. © *2002 MAIK "Nauka/Interperiodica".*

Key words: *active galactic nuclei, quasars, and radio galaxies.*

INTRODUCTION

The radio source 0642+449 (OH 471) is a high-redshift ($z = 3.406$) quasar (Carswell and Strittmatter 1973). Its recession velocity is 90% of the speed of light, and its visual magnitude is $18^m.5$ (Polatidis *et al.* 1995). OH 471 is one of the most intense radio sources at millimeter wavelengths.

OH 471 has been studied at the Crimean Astrophysical Observatory since the beginning of 1978 by Efanov *et al.* (1981). The quasar was found to have a large high-frequency excess at millimeter wavelengths and to be variable at a frequency of 22 GHz. To investigate the spectrum and low-frequency variability of OH 471, we carried out observations in 1996 with the Westerbork Synthesis Radio Telescope (WSRT) at 307–385 MHz and analyzed the archival WSRT observations at 323–327 and 4874 MHz for 1985–1990.

OBSERVATIONS

We observed the quasar OH 471 in 1996 with the WSRT using a digital correlator at eight frequencies in the range 307–385 MHz with a reception bandwidth of 5 MHz each. The WSRT consists of thirteen 25-meter parabolic antennas forming 78 radio interferometers. The hour angles at which the source was observed varied between $-57.^\circ5$ and $+79.^\circ5$. The pointing center corresponded to the position of OH 471. The calibration source 3C 48 was observed one hour before the beginning of our observations. The system temperature for the frequency range 307–385 MHz was 140 K; the synthesized beam size was $33'' \times 50''$.

We also analyzed the archival observations of sky fields that included OH 471 at 322.8 MHz in 1985, 1987, and 1988 and at 4874 MHz in 1990. The 1987–1988 data were calibrated by using the total flux density from the sources within a $2.5^\circ \times 2.5^\circ$ field and the improved total flux density obtained for this field in 1996. In the observing session of 1985, the flux density was calibrated using the source 3C 295.

The results of our observations are presented in Table 1. Its columns give, respectively, (1) dates of observations (year and day), (2) observation frequencies ν, (3) observation bandwidths $\Delta\nu$, (4) and (5) coordinates of the pointing field center, (6) recorded flux densities from the source F, and (7) their measurement errors ΔF; the calibration error did not exceed 5%. Column 8 lists the calibration sources. The flux densities of the calibration sources 3C 48 and 3C 295 were taken from Baars *et al.* (1977).

DATA PROCESSING

The 1996 Observations

We used the SELFCAL and ALIGN self-calibration algorithms to model and map the fields under study. This processing method was described in detail by Kolkman (1993). Figure 1 shows a map of the central region that includes OH 471 and a source 2.′5 north of it. The minimum isophotal level of the map corresponds to the minimum detection level of 5 mJy.

The 1987–1988 Observations

The center of the field under study in 1987–1988 was displaced by 0.3° relative to the field observed in 1996. Therefore, we adjusted the mapping data to the 1996 data. Assuming that the number of sources

*E-mail: volvach@crao.crimea.ua

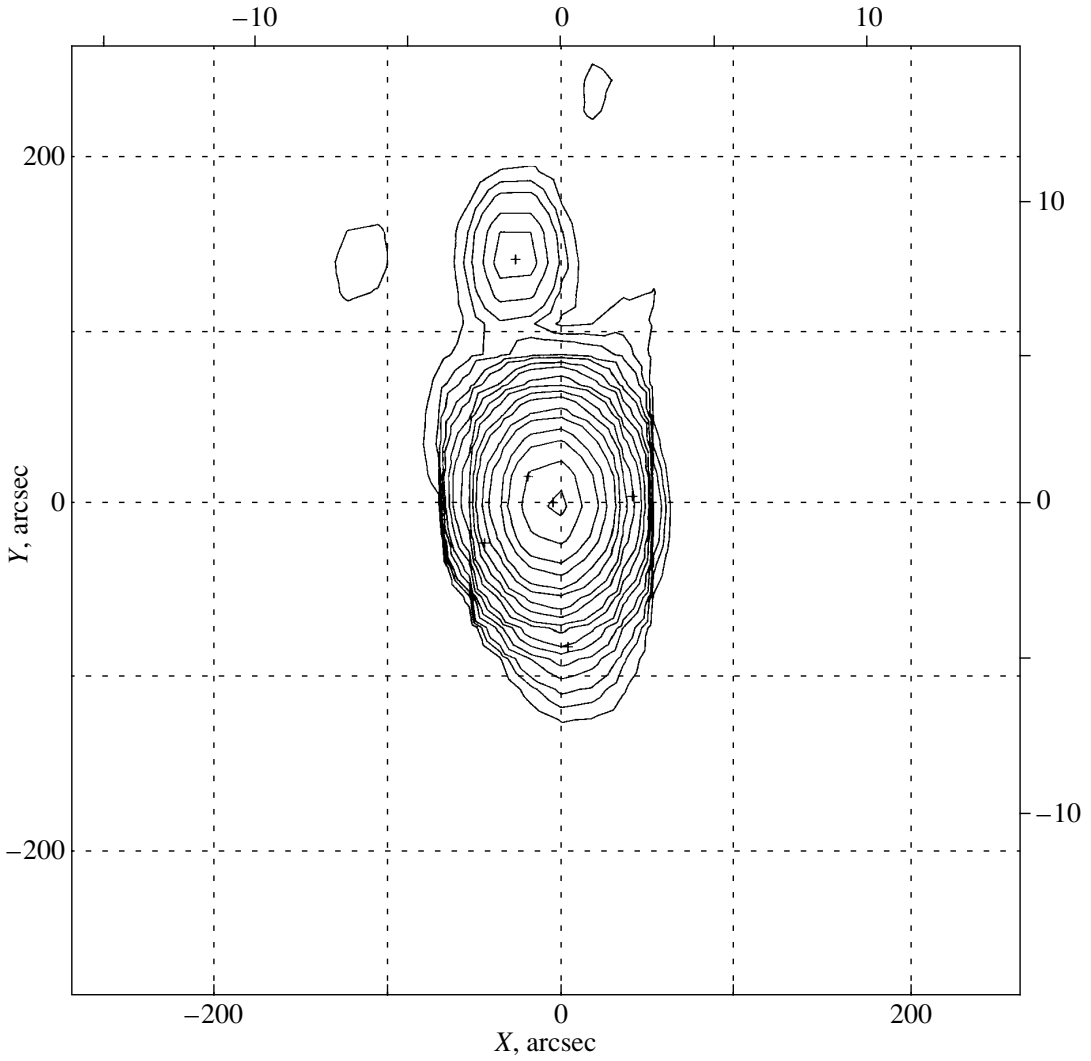

Fig. 1. The 325-MHz map of the object field at 1996.017.

within this field remained the same between 1987 and 1996, we can determine the flux density of each of them from the total flux density of all sources, provided that the flux density from these sources was calibrated at one of the epochs.

We used the 325-MHz map obtained during the 1996 observations as a calibration map, with the total flux density from the sources equal to 20.530 Jy. The field size near OH 471 is $2.5^\circ \times 2.5^\circ$. We did not correct the flux densities from the calibration source 3C 48 for the spectrum slope when comparing the 325-MHz data of 1996 with the 322.8-MHz data of 1987–1988. The introduced error is less than 0.5%.

The 1985 Observations

Since the quasar was at the field center during this period, we can directly subtract the 1985 map from the 1996 map. The total flux density from all the other sources within a $1.25^\circ \times 1.25^\circ$ field is 3.3 Jy. The 60-mJy difference is distributed between more than ten other bright sources in this field.

The 1990 Observations

During this period, the observations were carried out at 4874 MHz with a frequency band of 80 MHz. The system noise temperature was 55 K, and the synthesized beam size was $3.44'' \times 4.88''$. The observational data were processed by using the NEWSTAR software package (Noordam 1992). Figure 2 shows a $10' \times 10'$ map of the sky field around OH 471. Table 2 lists parameters of the sources detected in this field at 6 cm: columns 1, 2, 3, and 4 give source names, measured flux densities F, and source coordinates, respectively.

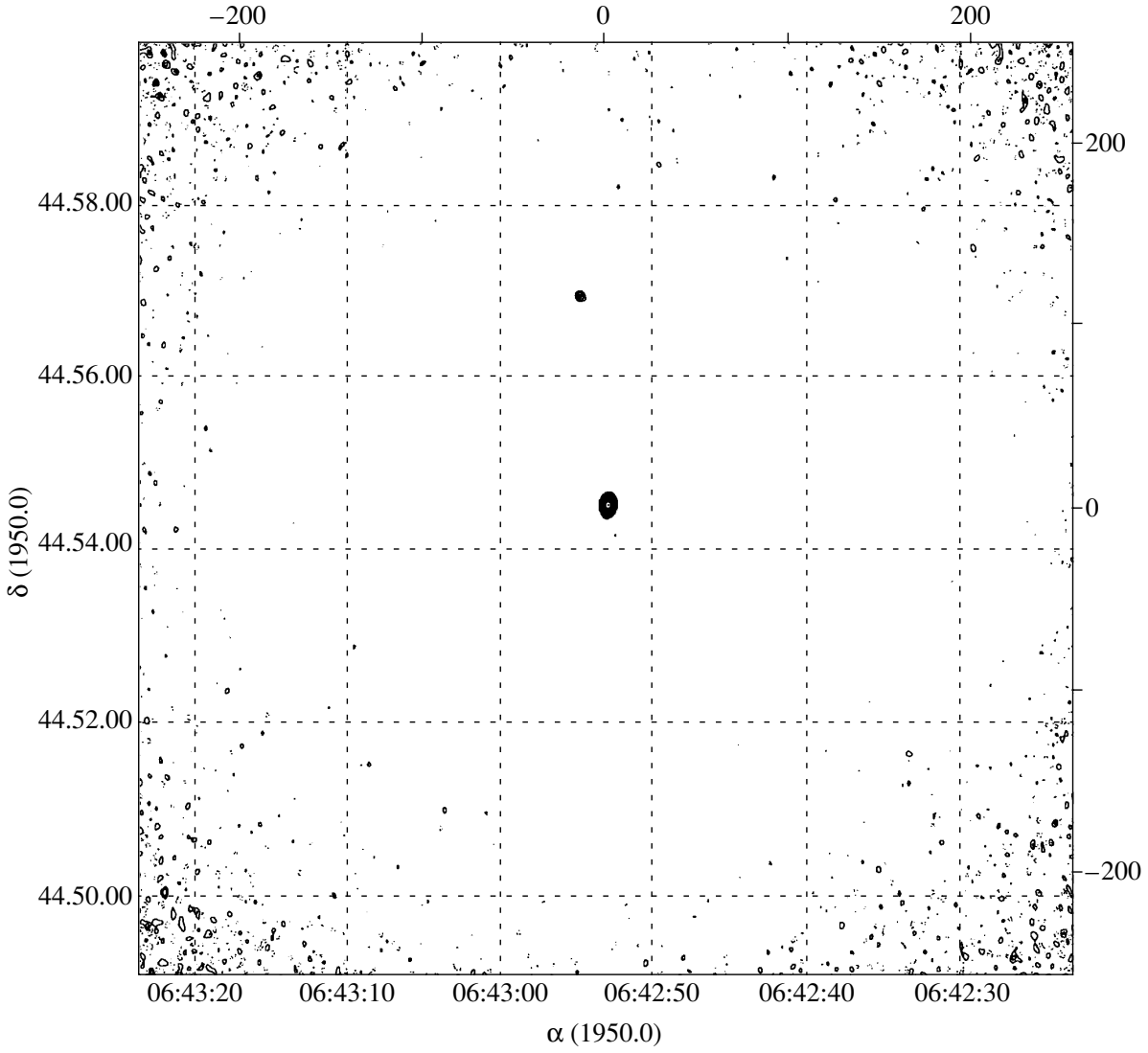

Fig. 2. The 5-GHz map of the object field at 1990.140.

The calibration source was not observed. We estimated the measurement error from the WSRT stability to be ≈3%. The relative calibration was made by using a noise generator. The measurement error of the flux density for OH 471 is determined by the accuracy of the flux scale, being 40 mJy. The second, weak source with a flux density of 1.46 mJy is real. The measurement error of its flux density is 0.07 mJy; it is mainly determined by noise. This source has a counterpart observed on low-frequency maps (Fig. 1).

RESULTS

As follows from the data in Table 1, the flux density of OH 471 at low frequencies significantly changed between 1985 and 1996. The flux difference in the frequency range 307–385 MHz was 265 mJy. Its spectral index is 0.9 in the frequency range 307–385 MHz. The observations by Riley and Green (1998) and Minns and Riley (2000) confirm the low-frequency variability of the quasar OH 471.

At 6 cm (Table 2, Fig. 2), a source with a flux density of 1.46 mJy is observed 2.′5 north of OH 471. The flux density of the source at 350 MHz is 14.5 mJy. It has a steep spectrum with a spectral index of −0.87. The expected flux density at 22 GHz must be less than 0.5 mJy; hence, it has no significant effect on the single-dish monitoring data for OH 471 at high frequencies. However, because of the confusion effect, it may be the cause of error in the single-dish data obtained at earlier epochs of observation.

Table 1

Date, year, day	ν, MHz	$\Delta\nu$, MHz	Pointing position (deg, 1950)		F, mJy	ΔF, mJy	Calibration source
1985, 091	327.0	0.6	100.7208	44.9086	445	5	3C 295 ($F = 60.6$ Jy)
1987, 341	322.8	2.3	101.2000	45.0000	489	6	Field sources
1987, 355	322.8	2.3	101.2000	45.0000	484	6	"
1988, 023	322.8	5.0	101.2000	45.0000	488	6	"
1996, 017	307.5	5.0	100.7208	44.9086	671	9	3C 48 ($F = 44.9$ Jy)
	325.0	5.0	100.7208	44.9086	710	8	"
	341.0	5.0	100.7208	44.9086	765	8	"
	349.0	5.0	100.7208	44.9086	736	8	"
	355.0	5.0	100.7208	44.9086	754	8	"
	360.0	5.0	100.7208	44.9086	782	9	"
	375.0	5.0	100.7208	44.9086	801	9	"
	385.0	5.0	100.7208	44.9086	827	9	"

Table 2

Source	F, mJy	α	δ
OH 471	1338	06:42:52.98	44.54.31.27
Field source	1.46	06:42:54.75	44.56.56.46

CONCLUSIONS

In 1996, we found an increase in the 325-MHz flux density of the quasar by a factor of 1.6 compared to the observational data of 1985. Consequently, the quasar OH 471 is variable at low frequencies.

We detected a steep-spectrum source 2′.5 north of the quasar OH 471 with a flux density of 1.46 mJy at 5 GHz and 14.5 mJy at 350 MHz.

REFERENCES

1. J. W. M. Baars, I. I. K. Pauliny-Toth, and A. Witzel, Astron. Astrophys. **61**, 99 (1977).
2. R. F. Carswell and P. A. Strittmatter, Nature **242**, 396 (1973).
3. V. A. Efanov, I. G. Moiseev, N. S. Nesterov, *et al.*, Izv. Krym. Astrofiz. Obs. **64**, 103 (1981).
4. O. M. Kolkman, *The Westerbork Synthesis Radio Telescope User Documentation, Version 1.0.0.* (Netherlands Foundation for Research in Astronomy, Dwingeloo, 1993).
5. A. R. Minns and J. M. Riley, Mon. Not. R. Astron. Soc. **315**, 839 (2000).
6. J. E. Noordam, *NEWSTAR Cookbook* (Netherlands Foundation for Research in Astronomy, Dwingeloo, 1992).
7. A. G. Polatidis, P. N. Wilkinson, W. Xu, *et al.*, Astrophys. J., Suppl. Ser. **98**, 1 (1995).
8. J. M. Riley and D. A. Green, Mon. Not. R. Astron. Soc. **301**, 203 (1998).

Translated by G. Rudnitskii

Astronomy Letters, Vol. 28, No. 10, 2002, pp. 660–668. Translated from Pis'ma v Astronomicheskiĭ Zhurnal, Vol. 28, No. 10, 2002, pp. 732–740.

The Soft X-ray Novae, Black-Hole Candidates XTE J2012+381 and XTE J1550−564

N. L. Aleksandrovich* and V. A. Aref'ev

Space Research Institute, Russian Academy of Sciences, Profsoyuznaya ul. 84/32, Moscow, 117810 Russia

Received May 15, 2002

Abstract—In 1998−1999, the X-ray transients XTE J2012+381 and XTE J1550−564 were observed with the TTM X-ray telescope onboard the Mir−Kvant astrophysical module. Spectral properties of these sources on the descent of the light curve after the secondary maxima of their outbursts are studied. Upper limits on the off-state flux are given. Comparison with other X-ray novae observed with the TTM telescope leads us to conclude that XTE J2012+381 and XTE J1550−564 are soft X-ray novae. XTE J2012+381 probably belongs to the subclass of long-period X-ray transients. © *2002 MAIK "Nauka/Interperiodica"*.

Key words: *Mir−Kvant, TTM, RXTE, black holes, X-ray binaries, X-ray novae, transients, XTE J2012+381, XTE J1550−564.*

INTRODUCTION

The Roentgen astrophysical observatory onboard the Kvant module of the Mir Space Station had been in operation since April 1987. Only one Roentgen instrument had an X-ray imaging capability — the coded-mask TTM telescope with a position-sensitive detector. The TTM was sensitive to X-ray emission in the energy range 2−27 keV, with the highest efficiency in the soft region. The TTM total field of view and angular resolution were, respectively, $15^\circ \times 15^\circ$ and $\sim 2'$ (Brinkman *et al.* 1985). Because of the significant orbital inclination of Mir (52°) and its low altitude (350−400 km), only the equatorial segment of its orbit, where the radiation background was at a minimum, was used for the Roentgen operation. Therefore, the duration of a single observing session did not exceed 30 min.

When weak sources were studied, observing sessions were added to increase the significance of source detection and to reduce the measurement errors of the fluxes (or to decrease the upper limits on the fluxes from sources whose signals could not be picked out during one session). The flux detection efficiency also depends on the position of the source being studied within the TTM field of view and on the positions and intensities of other sources within its field of view. Here, we analyze all of the series of TTM sessions in which the sources XTE J2012+381 and XTE J1550−564 were observed. New TTM software allowed the upper limits on the off-state fluxes from these sources to be significantly reduced.

*E-mail: nick@hea.iki.rssi.ru

XTE J2012+381

XTE J2012+381 was discovered in May 1998 by the All-Sky Monitor onboard the RXTE satellite as a transient source in a region with coordinates $\alpha = 20^{\rm h}12^{m}.6 \pm 0^{m}.7$ and $\delta = +38^\circ 11' \pm 4'$ (epoch 2000.0). Its intensity rapidly increased from 23 mCrab (2−12 keV) on May 24 to 88 mCrab on May 27, which was accompanied by an enhancement of the soft part of the spectrum (Remillard *et al.* 1998a). On May 29, the RXTE team improved the error region to $1'$ and reported a rise in the source intensity to 110 mCrab (Marshall and Strohmayer 1998).

According to the ASCA observations on May 29−30, the flux from the source increased with time in the energy range 0.7−4 keV and was constant in the range 4−10 keV; the mean 2−10-keV intensity reached 150 mCrab. The ASCA spectrum consists of blackbody and power-law components at the temperature of the inner accretion-disk regions $kT = 0.76 \pm 0.01$ keV, photon index $\gamma = 2.9 \pm 0.1$, and hydrogen column density (for the assumed solar heavy-element abundance) $N_{\rm H} = (1.29 \pm 0.03) \times 10^{22}$ cm^{-2}. Such an ultrasoft spectrum with a hard power-law tail is a distinctive feature of black-hole candidates (White *et al.* 1998).

PCA/RXTE observations (Vasiliev *et al.* 2000) showed that the 3−20-keV flux reached 220 mCrab at the primary maximum. The source spectrum was well described by the composite model of a multicolor accretion disk and a power law with the inclusion of a broad Gaussian emission line at an energy of 6.4 keV. The source spectrum evolved with time, becoming

1063-7737/02/2810-0660$22.00

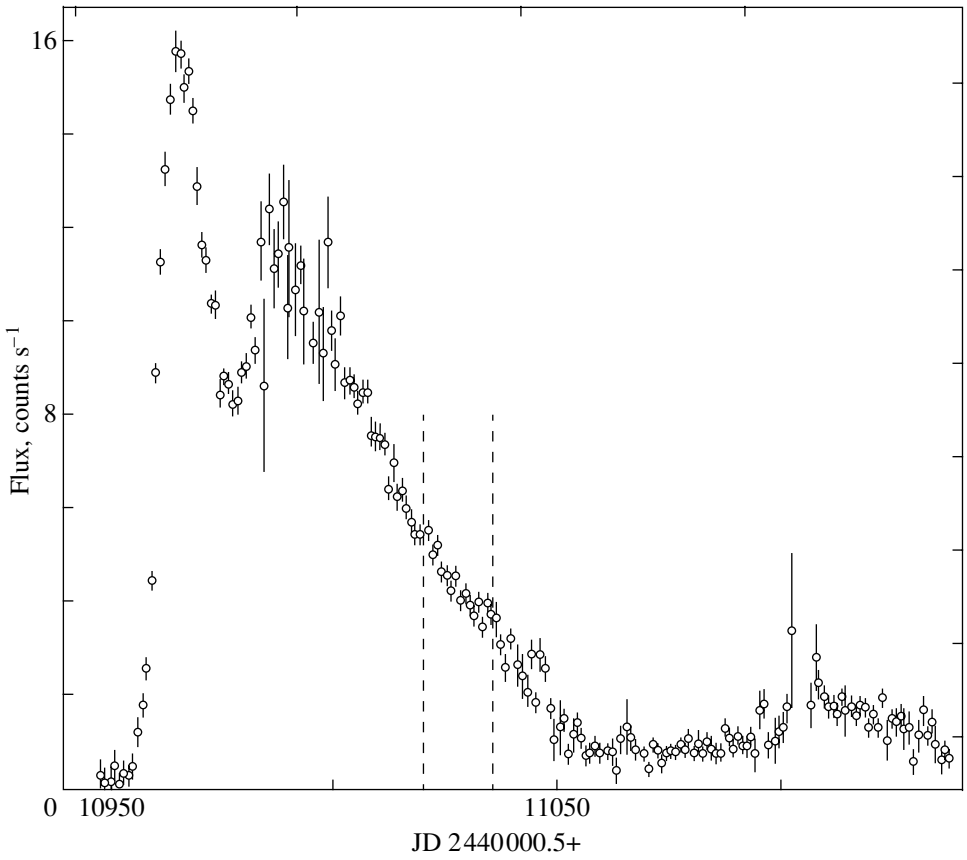

Fig. 1. The 2–12-keV light curve of XTE J2012+381 constructed from archival ASM/RXTE data. The time interval during which the Roentgen observations were carried out is highlighted by dashed lines.

increasingly soft. The soft component was relatively weak before the primary maximum (May 27) and significantly strengthened near the maximum (June 1), while the hard component significantly weakened at the time of quasi-linear decline after the secondary maximum (July 7–29). During the decline after the secondary maximum, the temperature of the blackbody component decreased by ~10% to 0.65 keV; the photon index erratically varied over the range 1.6–4.9. The emission was similar in frequency parameters to the emission from black-hole candidates in a very high state (VHS).

Initially, the star UNSO A1.0 1275.13846761 ($V = 18\overset{m}{.}1 \pm 0\overset{m}{.}1$, $B-V = +1\overset{m}{.}25$), presumably an F3 dwarf at a distance of 3 kpc or an F0 giant at a distance of 6 kpc (similar to the counterpart of Cyg X-2, an F giant) (Garcia *et al.* 1998), was considered as a possible optical counterpart. However, more detailed studies (Hynes *et al.* 1999) showed a faint red star ($V = 21\overset{m}{.}33 \pm 0\overset{m}{.}10$, $R = 19\overset{m}{.}90 \pm 0\overset{m}{.}15$, $I = 18\overset{m}{.}64 \pm 0\overset{m}{.}10$) at less than 1″ from the UNSO star to be the optical counterpart; it lies behind the bright UNSO star.

Radio observations (Hjellming *et al.* 1998) revealed a variable source with the coordinates $\alpha = 20^{\rm h}12^{\rm m}37\overset{\rm s}{.}67$ and $\delta = +38°11'01\overset{''}{.}2$ (epoch 2000.0) that is closer to the faint red star than to the UNSO star.

The ASM/RXTE 2–10-keV light curve of the source is shown in Fig. 1. It is characterized by a fast rise in the flux during the outburst, by the presence of primary and secondary maxima, and by a slow quasi-linear decline after the secondary maximum. The Roentgen observations cover a segment of the source light curve after the secondary maximum.

ROENTGEN DATA

The X-ray transient XTE J2012+381 is located in Cygnus roughly halfway between Cyg X-3 and the black-hole candidate Cyg X-1 (Fig. 2). This sky region was regularly observed with the Roentgen instruments, which allowed TTM data to be used to determine the upper limits on the flux from XTE J2012+381 in 1989–1995. The source itself was not detected in these sessions, which indirectly confirms the assumption that it belongs to X-ray novae. Upper limits (at 3σ confidence) on the photon

Table 1. The 2–27-keV fluxes from XTE J2012+381 during the 1989–1998 TTM sessions

Date of observation	MJD	Accumulation time, min	R, deg	Flux, mCrab
June 8–15, 1989	7689.052	298.5 (17 sessions)	4.49–5.87	<3.8
July 6–11, 1989	7715.835	546.8 (30 sessions)	1.76–4.86	<1.8
Aug. 19, 1989	7757.375	113.8 (6 sessions)	5.47–5.98	<5.5
Dec. 30–31, 1991	8620.922	35.5 (3 sessions)	4.01–4.05	<7.5
Sep. 4–Nov. 23, 1992	8909.598	118.7 (7 sessions)	4.33–4.82	<5.2
Nov. 19–Dec. 18, 1993	9324.711	53.7 (3 sessions)	4.00–4.09	<6.7
Apr. 11–12, 1994	9453.473	34.4 (2 sessions)	4.00–4.04	<9.3
Oct. 31, 1995	10021.786	16.8	4.71	<7
July 25, 1998	11019.606	16.5	5.10	31 ± 3
July 26, 1998	11020.755	16.0	4.81	33 ± 5
July 27, 1998	11021.776	16.0	4.78	32 ± 4
Aug. 8, 1998	11033.841	15.9	3.21	24 ± 4

Note. R is the angular distance of the source from the center of the TTM field of view. In the 1989–1995 sessions when the source was invisible, (3σ) upper limits on its flux are given.

fluxes in the sessions and series of sessions from 1989 to 1995 are given in Table 1 and shown in Fig. 3. The upper limits (2–7 mCrab) on the flux from the source are seen to be lower than the X-ray plateau of ~12 mCrab that the source reached ~100 days after its detection and below which it did not sink until ~220 days.

During the 1998 observations, XTE J2012+381 was within the TTM/Roentgen field of view in two series of three sessions each (July 25–27 and August 6–9); in the second series, it was detected only in one session. We managed to obtain a statistically significant spectrum only during the first series. The TTM flux from XTE J2012+381 varied between 20 and 30 mCrab. Information on these sessions is also given in Table 1. The source spectrum summed over the three TTM sessions on July 25–27, 1998, is satisfactorily fitted by the model of a multicolor disk with a hard power-law component typical of X-ray novae: $kT_{\rm in} = 0.55 \pm 0.04$ ($T_{\rm in}$ is the temperature of the inner disk edge) and $\alpha = 1.2 \pm 0.8$ ($\chi^2 = 0.5$). A simple power law yields the photon index $\alpha = 4.4 \pm 0.6$ with the hydrogen absorption column density $N_{\rm H} = (2.8 \pm 1.7) \times 10^{22}$ cm^{-2} ($\chi^2 = 0.8$), but it poorly describes the spectrum in the hard energy range. The parameters of the standard model are in good agreement with the PCA/RXTE data obtained approximately at the same time (Vasiliev *et al.* 2000).

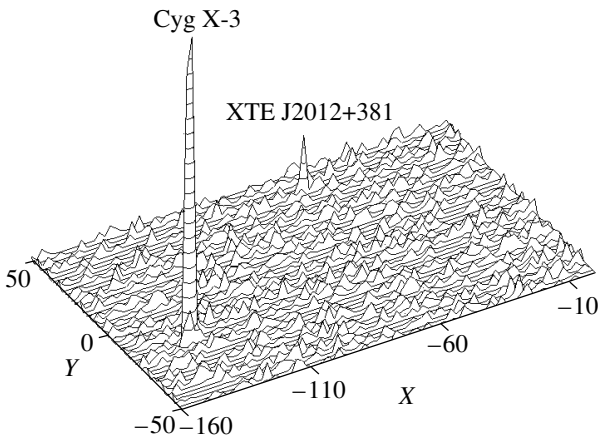

Fig. 2. A part ($4.^{\circ}8 \times 3^{\circ}$) of the TTM image of the sky region near Cyg X-3 obtained from July 25 until July 27, 1998 (the sum of three sessions). The peak height is proportional to the significance of detection. The numbers along the X and Y axes are the coordinates in detector pixels (1 pixel corresponds to $1.'82$).

XTE J1550–564

The X-ray nova XTE J1550–564 was discovered on September 7, 1998, by the All-Sky Monitor onboard the RXTE satellite as a transient source of intensity ~70 mCrab (2–12 keV) with the coordinates $\alpha = 15^{\rm h}50^{\rm m}41^{\rm s}$ and $\delta = -56^{\circ}27.'6$ (epoch 2000.0) (Smith 1998). According to BATSE/GRO data, the 20–100-keV flux from the source did not exceed 0.1×10^{-8} erg cm^{-2} s^{-1} before September 7 and was $(2.42 \pm 0.11) \times 10^{-8}$ erg cm^{-2} s^{-1} on September 9

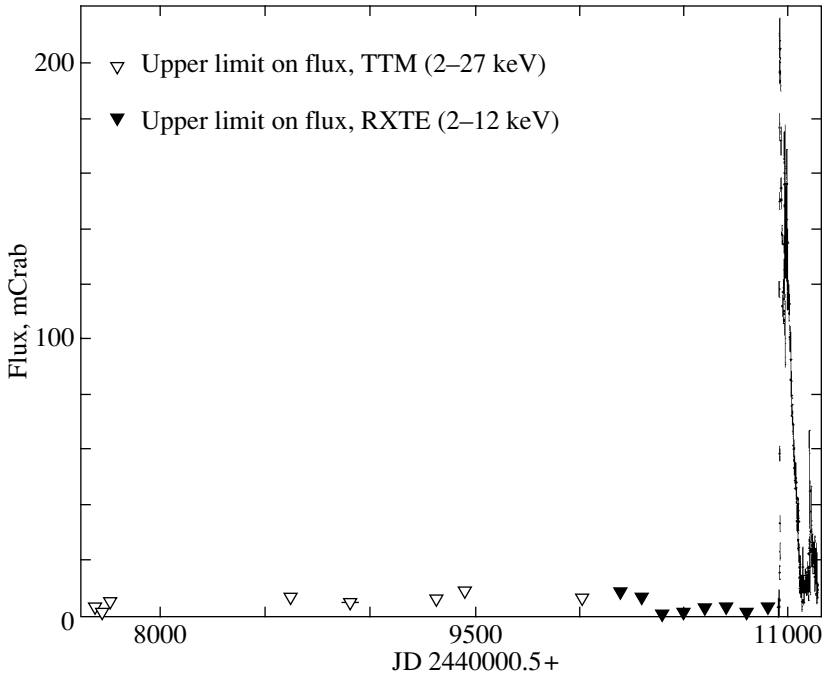

Fig. 3. The 2–12-keV light curve of XTE J2012+381 constructed from archival ASM/RXTE data and ASM/RXTE and TTM (2–27 keV) upper limits on the flux.

(Wilson *et al.* 1998). These data also revealed quasi-periodic oscillations with a centroid frequency of 271 ± 2 mHz and a FWHM of 30 ± 5 mHz (Finger *et al.* 1998).

According to ASM/RXTE data, the flux from the source reached 1.7 Crab (2–12 keV) on September 15 while being highly variable. A strong outburst was recorded on September 19–20, during which the source intensity reached 6.8 Crab; on September 20–21, its flux decreased to 2.7–3.6 Crab (Remillard *et al.* 1998b). During the outburst, high-frequency quasi-periodic oscillations (in the energy range 2–30 keV) were also detected at a frequency of 183.6 Hz with a FWHM of 46 Hz (McClintock *et al.* 1998).

The BATSE instruments recorded a recurrent outburst on January 21–23, 1999. During this outburst, the mean 20–100-keV photon flux reached 300 mCrab, with the spectrum being a power law with $\alpha = -2.3 \pm 0.2$ (Harmon *et al.* 1999).

Between March 4 and 5, 1999, the RXTE satellite observed an unexpected transition of the source to a high state. This transition manifested itself in an increase of the flux in the soft (2–20 keV) energy range, in a hardening of the power-law spectral component, and in another appearance of high-frequency quasi-periodic oscillations (Homan *et al.* 1999).

A star of magnitude $V = 16^m.7 \pm 0^m.1$ with broad and intense emission lines (Hα, Hβ, He II) typical of soft X-ray transients during outbursts is believed to be the most probable optical counterpart of the source (Castro-Tirado *et al.* 1999).

A year later, in April 2000, yet another strong recurrent outburst was recorded from XTE J1550–564. It was detected by RXTE on April 6–10 (Smith *et al.* 2000) and by BATSE on April 6–8 (McCollough *et al.* 2000). This outburst was accompanied by a rise in the optical brightness of the source (Masetti and Soria 2000; Jain and Bailyn 2000).

The (ASM/RXTE) 2–10-keV and (BATSE) 20–100-keV light curves of the source are shown in Fig. 4. In the soft energy range, we clearly see a narrow primary maximum on September 20, 1998, and a less intense but broad secondary maximum in January–March 2000. A transition of the source to a soft (high) state was recorded on March 5 on the descent of the latter maximum. The time interval of the Roentgen observations for XTE J1550–564 indicated by dashed lines is located on the descent of the secondary maximum after the change of the source state.

ROENTGEN DATA

The source XTE J1550–564 lies in the sky a short distance from the well-known burster Circinus X-1, which was repeatedly observed by the Roentgen instruments in different years. However, the absence of other bright X-ray sources nearby prevents the orientation of the TTM field of view from being

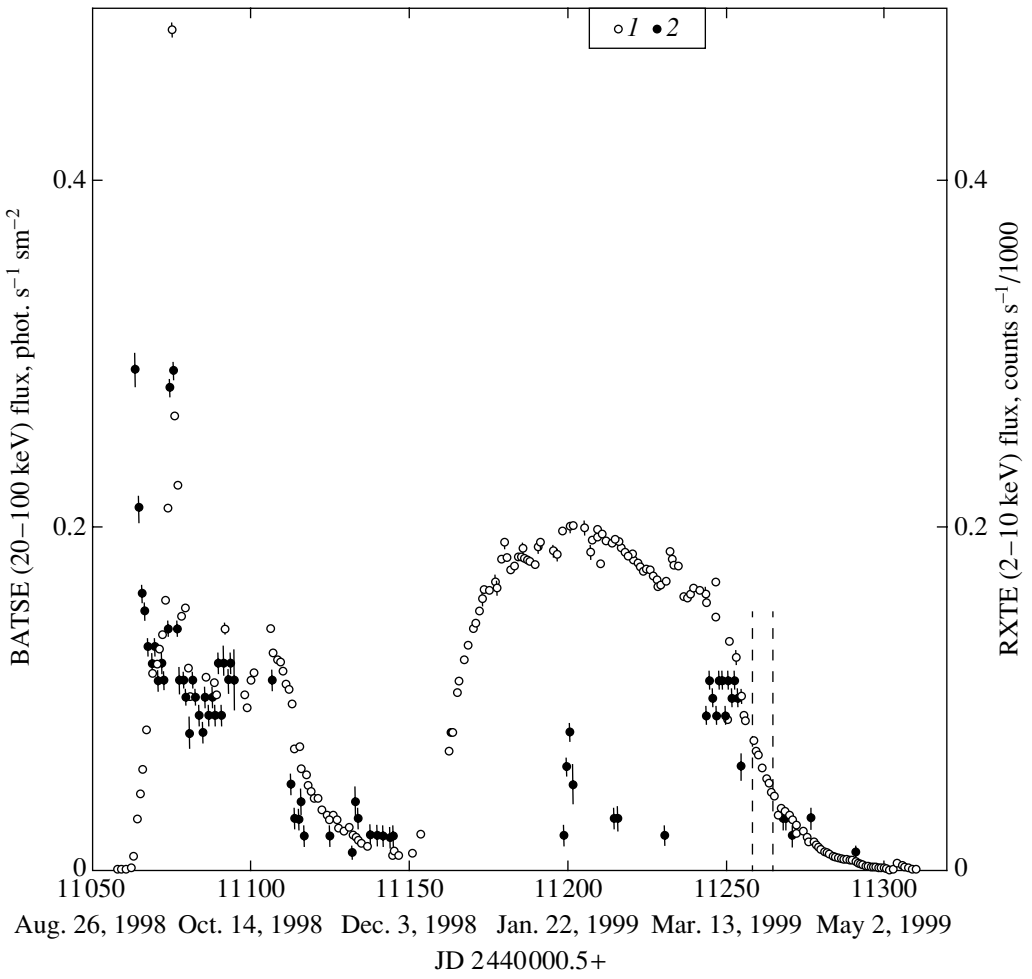

Fig. 4. The light curves of XTE J1550–564 in the energy range 2–12 keV constructed from archival ASM/RXTE data (*1*) and in the energy range 20–100 keV constructed from archival BATSE/GRO data (*2*). The time interval during which the Roentgen observations were carried out is highlighted by dashed lines.

completely restored in those sessions in which the TTM telescope did not detect XTE J1550–564 or another known source simultaneously with Circinus X-1. Thus, in several 1989 sessions, we managed to restore the orientation using the sources 4U1563–624 and 4U1538–522. Therefore, upper limits on the fluxes from XTE J1550–564 in early Roentgen observations can be reliably determined only from eight sessions of early 1989. Upper limits on the photon flux and accumulation times in these sessions, as well as source fluxes in the 1999 sessions are given in Table 2.

In the sessions of March 21, 22, 27, and 28, 1999, the source was bright enough for the TTM telescope to obtain high-quality spectra in individual sessions. In the sessions of March 23, 24, and 26, we managed to construct a satisfactory spectrum only from their sum. Parameters of the power-law fit to the spectrum are given in Table 3. We can only conclude from these data that the source spectrum became slightly softer by the end of the series of TTM observations.

More interesting results are obtained when the spectrum is described by the standard (for X-ray novae) two-component model: a multicolor disk with a hard power-law tail. Parameters of this model for different sessions are given in Table 4. In the three most significant sessions, this model better describes the spectral shape than does a simple power law. The session of March 27, in which the temperature of the blackbody spectral component decreased sharply and significant absorption appeared, is particularly noteworthy. The spectrum in this session is compared with the TTM spectrum of March 21 in Fig. 5. A day later, on March 28, the source returned to the state in which it was in the remaining sessions being described. Thus, it seems likely that TTM recorded a short-time change in the state of XTE J1550–564 on March 27.

Table 2. The TTM sessions for XTE J1550−564 in 1989 and 1999

Date of observation	MJD	Accumulation time, min	R, deg	Flux, mCrab
Jan. 27−Feb. 2, 1989	7556.826	142.4 (8 sessions)	3.97−4.68	<3.9
Mar. 21, 1999	11258.834	16.0	1.04	461 ± 6
Mar. 22, 1999	11259.787	16.0	1.03	133 ± 4
Mar. 23, 1999	11260.805	20.0	1.08	36 ± 3
Mar. 24, 1999	11261.502	20.0	1.08	25 ± 3
Mar. 26, 1999	11263.725	15.1	1.08	47 ± 5
Mar. 27, 1999	11264.425	23.7	0.34	436 ± 6
Mar. 28, 1999	11265.507	19.2	0.70	447 ± 8

Note. R is the angular distance of the source from the center of the TTM field of view. In the 1989 sessions when the source was invisible, (3σ) upper limits on its flux are given.

Table 3. The TTM sessions for XTE J1550−564 in 1999 and parameters of the power-law fit to its spectrum as inferred from TTM data

Date, 1999	Confidence level, σ	α	N, $\times 10^{22}$ cm^{-2}	χ^2
Mar. 21 (3062)	73.8	3.9 ± 0.1	3.2 ± 0.4	1.9
Mar. 22 (3063)	32.2	3.7 ± 0.3	2.7 ± 1.3	1.6
Mar. 23 (3064)	10.3	4.1 ± 0.7	3.6 ± 2.9	1.1
Mar. 24 (3065)	8.4	–	–	–
Mar. 26 (3067)	8.7	–	–	–
Mar. 27 (3068)	76.1	4.6 ± 0.2	4.9 ± 0.8	1.3
Mar. 28 (3069)	54.9	4.5 ± 0.2	4.3 ± 0.8	1.8

DISCUSSION

The sources XTE J2012+381 and XTE J1550−564 are undoubtedly soft X-ray novae, black-hole candidates. This is suggested by the following. Both sources are transient; i.e., they have not been recorded previously but were detected during a sharp rise in the X-ray flux. The TTM data confirm the absence of a significant flux from these sources in the past. Both sources have quite similar light curves, which are also typical of other X-ray novae: a fast rise at the initial stage, a narrow primary maximum, a slow quasi-exponential decline after the primary maximum, and recurrent outbursts. A hard power-law component in the spectra is also a characteristic feature, and it was recorded in all of the X-ray novae studied by the Mir−Kvant module (Sunyaev *et al.* 1994). A soft blackbody spectral component with a characteristic temperature of $\leq$1 keV was also observed in GS 2000+25 (Sunyaev *et al.* 1988) and GRS 1009−45 (Sunyaev *et al.* 1994), representatives of the subclass of soft X-ray novae. The spectra of XTE J2012+381 and XTE J1550−564 in the TTM energy range when compared with the spectra of other novae observed previously by this instrument give grounds to place them into the subclass of soft X-ray novae (Fig. 6). State-to-state transitions (for XTE J1550−564, from a hard state to a softer state) were also observed in other X-ray novae. For example, spectral changes similar to the transition from a hard state to a soft state in the best-known black-hole candidate Cyg X-1 were found in GRS 1124−648 (Grebenev *et al.* 1992) and KS 1730−312 (Borozdin *et al.* 1995).

Hynes *et al.* (1999) suggested that XTE J2012+381 belonged to the subclass of long-period X-ray transients. Good coverage of the sky region near XTE J2012+381 with TTM observations (Table 1, Fig. 3) makes it possible to estimate the minimum period between its two X-ray outbursts. If the second outburst is assumed to have had similar parameters (i.e., its flux was $\geq$10 mCrab over $\sim$200 days), then the probability that it occurred between 1989 and 1998 is $\leq$28%. An estimate based on the sample of TTM and ASM/RXTE data for these years, when there was no statistically significant

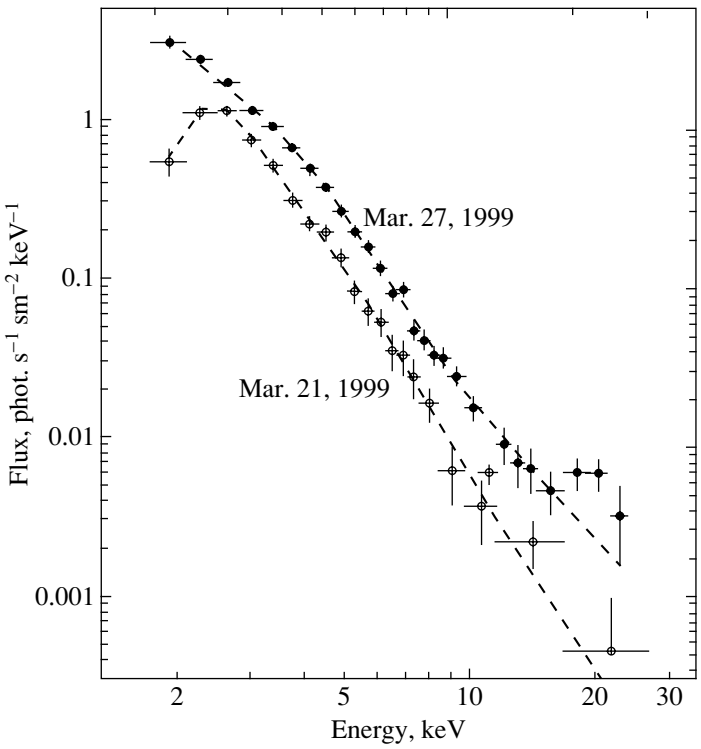

Fig. 5. The TTM 2–27-keV photon spectra of XTE J1550–564 on March 21 and 27, 1999.

detection of emission from the source, suggests that the most likely hypothesis is the absence of a second outburst over this period. Consequently, we can say with reasonable confidence that the period between the two X-ray outbursts for XTE J2012+381 is no less than nine years.

The outbursts of X-ray transients are commonly explained by accretion-disk instability. King and Ritter (1998) showed that the disk irradiation by X-ray photons from the central source should be taken into account for soft X-ray transients. If the irradiation is strong enough to completely ionize the disk, then the X-ray light curve must fall off exponentially. If, alternatively, the central X-ray source is not strong enough or the disk is too large and only part of the disk is ionized, then the light curve falls off linearly. In the former case, almost all of the matter in the disk is accreted during outburst, whereas in the latter case, part of the matter is not accreted during outburst. XTE J2012+381 exhibits a light curve (Fig. 1) characterized by the following: there is evidence of an exponential decline after the primary maximum, while after the secondary maximum, a linear decline in the X-ray flux is observed. The critical luminosity at which such a transition takes place (Shahbaz *et al.* 1998) is $L_{\rm crit} \sim 10^{37} \times (R_{\rm ion}/R_{11})^2$ erg s^{-1}, where $R_{\rm ion}/R_{11}$ is the radius of the ionized disk zone in 10^{11} cm. In that case, assuming the source luminosity at maximum to be close to the Eddington luminosity (see below), the transition to a linear regime occurs (see Fig. 1) at $L_{\rm crit} \sim 10^{38}$ erg s^{-1} and $R_{\rm ion} \sim 3 \times 10^{11}$ cm $\leq R_{\rm disk}$. A large accretion disk may, in turn, imply a long orbital period of the binary. This result agrees with the data of Shahbaz *et al.* (1998), who observed a linear fall-off of the light curve only in long-period binaries.

Table 4. Parameters of the blackbody fit with a hard power-law tail to the spectrum of XTE J1550–564 as inferred from TTM data.

Date, 1999	kT, keV	α	N, $\times 10^{22}$ cm^{-2}	χ^2
Mar. 21	0.76 ± 0.02	2.9 ± 0.1	–	1.4
Mar. 22	0.94 ± 0.02	3.2 ± 0.3	–	1.7
Mar. 23–26	0.72 ± 0.08	1.5 ± 1.1	–	0.6
Mar. 27	0.23 ± 0.04	4.8 ± 0.4	11 ± 4	1.2
Mar. 28	0.66 ± 0.02	1.5 ± 0.5	–	1.4

Note. The sessions of March 23, 24, and 26 were added.

A minimum upper limit on the off-state flux from XTE J2012+381 can be estimated from TTM data. The 2–20-keV luminosity of the source is 3.6×10^{33} [erg s^{-1}] $\times D_0^2$ [kpc] $\times K$ [mCrab], where D_0 is

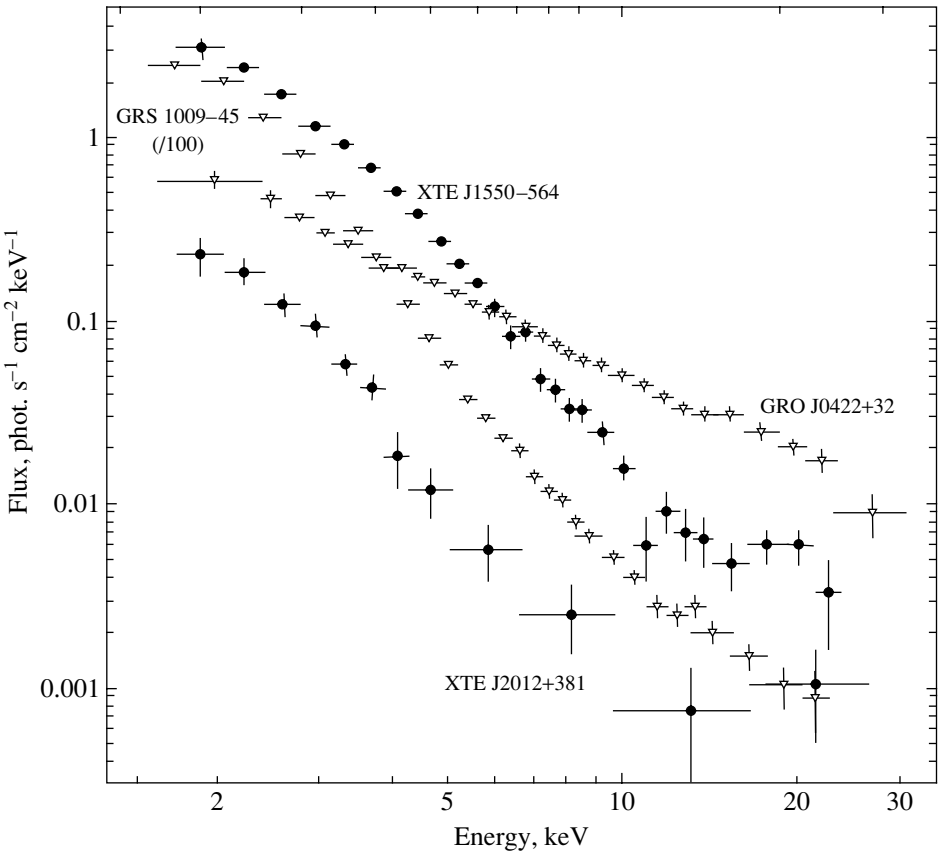

Fig. 6. Comparison of the energy spectra for XTE J2012+381 and XTE J1550−564 with the spectra of two other sources from this class: the soft X-ray nova GRS 1009−45 (1993) and the hard X-ray nova GRO J0422+32 (1992). For better perception, the spectrum of GRS 1009−45 was displaced vertically. All data were obtained with TTM in different years.

the distance to the source and K is its intensity. Since the optical counterpart is no closer than 3 kpc away (Garcia *et al.* 1998; Hynes *et al.* 1999) and since the (3σ) upper limits on the flux are 2–7 mCrab, the minimum (3σ) upper limit on the source luminosity is 6.5×10^{34}–2.3×10^{35} erg s^{-1}. This value is consistent with estimates for the off-state luminosities of X-ray transients, 10^{31}–10^{34} erg s^{-1}. The peak luminosity of the source was 6.3×10^{36} erg s^{-1}. On the other hand, since the source during its primary maximum exhibited a behavior that corresponded to the behavior of a black-hole candidate in a very high state (Vasiliev *et al.* 2000), the source luminosity must have been close to the Eddington luminosity, i.e., $\sim 10^{38}$–10^{39} erg s^{-1}. In that case, the distance to the source is $\sim$15 kpc. Thus, we have failed to obtain stringent constraints on the source distance from X-ray observations.

ACKNOWLEDGMENTS

We wish to thank M.R. Gilfanov and E.M. Churazov for the permission to use their TTM data processing software. We are also grateful to V.G. Rodin, A.V. Prudkoglyad, and the staff of the Flight Control Center, who controlled the instrumentation, and to A.N. Ananenkova for preliminary archival Roentgen data preparation. This study was supported in part by the Program of the Presidium of the Russian Academy of Sciences "Astronomy: Nonstationary Astronomical Objects" and the Russian Foundation for Basic Research (project no. 00-15-96649).

REFERENCES

1. K. N. Borozdin, N. L. Aleksandrovich, V. A. Aref'ev, *et al.*, Pis'ma Astron. Zh. **21**, 243 (1995) [Astron. Lett. **21**, 212 (1995)].
2. A. C. Brinkman, J. Dam, W. A. Mels, *et al.*, in *Non-thermal and Very High Temperature Phenomena in X-ray Astronomy,* Ed. by G. C. Perola and M. Salvati (Institute Astronomico, Rome, 1985), p. 263.
3. A. J. Castro-Tirado, H. W. Duerbeck, and I. Hook, IAU Circ., No. 7013 (1998).
4. M. H. Finger, S. W. Dieters, and R. B. Wilson, IAU Circ., No. 7010 (1998).
5. M. R. Garcia, J. E. McClintock, E. Barton, *et al.*, IAU Circ., No. 6931 (1998).

6. S. A. Grebenev, R. A. Syunyaev, and M. N. Pavlinskiĭ, Pis'ma Astron. Zh. **18**, 11 (1992) [Sov. Astron. Lett. **18**, 5 (1992)].
7. B. A. Harmon, M. H. Finger, M. L. McCollough, *et al.*, IAU Circ., No. 7098 (1999).
8. R. M. Hjellming, M. P. Rupen, and A. J. Mioduszewski, IAU Circ., No. 6932 (1998).
9. J. Homan, R. Wijnands, and M. van der Klis, IAU Circ., No. 7121 (1999).
10. R. I. Hynes, P. Roche, P. Charles, *et al.*, Mon. Not. R. Astron. Soc. **49**, 305L (1999).
11. R. Jain and C. Bailyn, IAU Circ., No. 7400 (2000).
12. A. King and H. Ritter, Mon. Not. R. Astron. Soc. **293**, L42 (1998).
13. F. E. Marshall and T. Strohmayer, IAU Circ., No. 6922 (1998).
14. N. Masetti and R. Soria, IAU Circ., No. 7399 (2000).
15. J. McClintock, G. Sobczak, R. Remillard, *et al.*, IAU Circ., No. 7025 (1998).
16. M. L. McCollough, C. A. Wilson, and X. Sun, IAU Circ., No. 7400 (2000).
17. R. Remillard, A. Levine, and A. Wood, IAU Circ., No. 6920 (1998a).
18. R. Remillard, E. Morgan, J. McClintock, *et al.*, IAU Circ., No. 7019 (1998b).
19. D. A. Smith, IAU Circ., No. 7008 (1998).
20. D. A. Smith, A. M. Levine, R. Remillard, *et al.*, IAU Circ., No. 7399 (2000).
21. R. A. Syunyaev, K. N. Borozdin, N. L. Aleksandrovich, *et al.*, Pis'ma Astron. Zh. **20**, 890 (1994) [Astron. Lett. **20**, 777 (1994)].
22. R. A. Syunyaev, I. Yu. Lapshov, S. A. Grebenev, *et al.*, Pis'ma Astron. Zh. **14**, 771 (1988) [Sov. Astron. Lett. **14**, 327 (1988)].
23. T. Shahbaz, P. Charles, and A. King, Mon. Not. R. Astron. Soc. **301**, 382 (1998).
24. L. Vasiliev, S. Trudolyubov, and M. Revnivtsev, Astron. Astrophys. **362**, L53 (2000).
25. N. E. White, Y. Ueda, T. Dotani, *et al.*, IAU Circ., No. 6927 (1998).
26. C. A. Wilson, B. A. Harmon, W. S. Paciesas, *et al.*, IAU Circ., No. 7010 (1998).

Translated by V. Astakhov

Astronomy Letters, Vol. 28, No. 10, 2002, pp. 669–675. Translated from Pis'ma v Astronomicheskiĭ Zhurnal, Vol. 28, No. 10, 2002, pp. 741–747.

Cooling of Neutron Stars: Two Types of Triplet Neutron Superfluidity

M. E. Gusakov[1]* and O. Yu. Gnedin[2]

[1] *State Polytechnical University, St. Petersburg, 198005 Russia*

[2] *Space Telescope Science Institute, Baltimore, USA*

Received May 14, 2002

Abstract—We consider the cooling of neutron stars with superfluid cores composed of neutrons, protons, and electrons (for singlet proton pairing and triplet neutron pairing). The emphasis is on triplet neutron pairing with the component of the total moment of neutron pairs along the quantization axis $|m_J| = 2$. This case stands out in that it leads to power-law rather than exponential suppression of the main neutrino processes by neutron superfluidity. For the chosen critical neutron temperatures $T_{\rm cn}$, the cooling with $|m_J| = 2$ proceeds either almost in the same way as the commonly considered cooling with $m_J = 0$ or appreciably faster. The cooling with variable (over the core) critical temperatures $T_{\rm cn}(\rho)$ and $T_{\rm cp}(\rho)$ can generally be described by the cooling with some effective constant temperatures $T_{\rm cn}$ and $T_{\rm cp}$. The hypothesis of strong neutron superfluidity with $|m_J| = 2$ is in conflict with the observational data on the thermal radiation from isolated neutron stars; the hypothesis of weak neutron superfluidity of any type is consistent with the observations. © *2002 MAIK "Nauka/Interperiodica".*

Key words: *pulsars, neutron stars, black holes.*

INTRODUCTION

The cooling of neutron stars (NSs) strongly depends on the properties of the matter in their cores, primarily on the equation of state for the matter (Lattimer and Prakash 2001) and on the critical temperatures of NS nucleon superfluidity (Lombardo and Schulze 2001). At present, both are known incompletely, because there is no reliable microscopic theory. The available knowledge on the properties of matter in NS cores can be improved by comparing observational data with NS cooling models.

Here, we consider some cooling models. For definiteness, we assume the standard composition of NS cores: neutrons (n), protons (p), and electrons (e).

It is well known that the neutrons and protons in NS cores can be in a superfluid state (Yakovlev *et al.* 1999; Lombardo and Schulze 2001). Model calculations of superfluid gaps show that proton pairing takes place in the singlet ($^1S_0$) state of the proton pair. Neutron pairing can take place in the singlet and triplet ($^3P_2$) states; singlet pairing generally arises in matter of moderate density ($\rho \lesssim \rho_0$, where $\rho_0 = 2.8 \times 10^{14}$ g cm^{-3} is the nuclear density), and triplet pairing arises in denser matter. The triplet pairing, in turn, can be of several types differing in the component of the total moment of their nucleon pair along the quantization axis ($|m_J| = 0, 1, 2$). Following the review articles by Yakovlev *et al.* (1999, 2001), we call the singlet pairing case A, the triplet pairing with $m_J = 0$ case B, and the triplet pairing with $|m_J| = 2$ case C. Case C stands out among the remaining cases in that the superfluid gap in the dispersion relation for neutrons becomes zero at some points on the Fermi surface (at its poles). This leads to a fundamentally different (power-law rather than exponential) dependence of the NS neutrino energy losses on the gap amplitude (Yakovlev *et al.* 1999). The type of superfluidity with a minimum free energy occurs in nature. The A-type proton pairing in the NS core, the A-type neutron pairing in the crust and in the outer core, and the B-type pairing in the inner core are commonly considered in cooling calculations. The C-type neutron pairing in the NS core seems less realistic, but it is not ruled out by current microscopic theories.

Up until now, virtually nobody has modeled NS cooling with C-type neutron superfluidity. We know only the recent paper by Schaab *et al.* (1998), who attempted to take into account the effect of such pairing on the main processes of neutrino energy emission in NS cores and on the NS cooling. Unfortunately, the authors failed to completely consider all of the factors that determine the thermal evolution of NSs. Thus, for example, when considering one of the most important neutrino processes, the neutrino emission during Cooper neutron pairing, the authors used an

*E-mail: gusakov@astro.ioffe.rssi.ru

exponential dependence instead of the correct power-law dependence of the energy loss rate on $T/T_{\rm cn}$ ($T_{\rm cn}$ is the critical neutron temperature).

Here, we analyze the NS cooling for the C-type neutron pairing more rigorously. We compare the coolings for the B- and C-type superfluidities. Our results are compared with observations .

NS COOLING FOR THE C-TYPE NEUTRON PAIRING

For the cooling to be adequately modeled, we must know the rate of neutrino energy emission in superfluid NS interiors and the heat capacity of the NS matter. Recall that the main neutrino processes in NS cores are the direct Urca process, the modified Urca process, the nucleon–nucleon scattering reactions, and the Cooper pairing of nucleons. The first process, the most powerful mechanism of neutrino energy emission, is a threshold process. The direct Urca process is open if $p_{Fn} \le 2p_{Fp}$, where p_{Fn} and p_{Fp} are the neutron and proton Fermi momenta, respectively.

The neutrino processes and heat capacity for cases A, B, and C have been studied extensively. The results can be found in the review article by Yakovlev *et al.* (2001) and in Gusakov (2002). Yakovlev *et al.* (2001) considered the neutrino processes with the A- or B-type neutron and A-type proton superfluidities; they took into account the effect of the C-type superfluidity on the direct Urca process, the neutrino energy emission during Cooper neutron pairing, and the neutron heat capacity. Gusakov (2002) investigated the modified Urca process during the C-type pairing and the nn- and np-scattering reactions. He also rigorously took into account the effect of combined A- or B-type nucleon superfluidity on the modified Urca process.

Here, we use the relativistic nonisothermal NS cooling code (see Yakovlev *et al.* 2001) adapted for the model with C-type neutron superfluidity. This code allows us to construct the *cooling curves,* i.e., to determine the dependence of the surface temperature of a star, T_e^∞, (as detected by a distant observer) on its age, t. Following Kaminker *et al.* (2002), we use the equation of state by Negele and Vautherin (1973) in the NS crust and the equation of state by Prakash *et al.* (1988) in the NS core with the compression modulus $K = 240$ MeV for symmetric nuclear matter at $\rho = \rho_0$ (model I from their paper for the symmetry energy). For this equation of state, the direct Urca process opens at $\rho \ge \rho_D = 7.851 \times 10^{14}$ g cm^{-3}, i.e., at $M \ge 1.358 M_\odot$. In this case, the maximum NS mass is $M = 1.977 M_\odot$. In the cooling code used, the effective proton and neutron masses in the inner NS layers renormalized with allowance made for multiparticle effects were assumed to be 0.7 of the mass of the free particles. The relationship between the NS effective surface temperature and the temperature at the bottom of the outer heat-blanketing envelope was taken from Potekhin *et al.* (1997).

To better understand at which critical nucleon temperatures the C-type neutron superfluidity in NS cores differs from case B, we mentally replace the NS under consideration by a sphere with a radially constant density characteristic of this star. In that case, after the completion of thermal relaxation and before the beginning of the photon NS cooling stage, the time derivative of the internal NS temperature can be estimated as $dT/dt \sim -Q/C$, where Q is the energy released in the form of neutrinos per unit volume per unit time and C is the heat capacity per unit volume. This formula holds for both B- and C-type neutron superfluidities. Since the C-type superfluidity suppresses the NS energy emission more weakly and since the energy released via Cooper pairing is higher than that in case B, we may say that $Q_C > Q_B$ always. Similarly, $C_C > C_B$; therefore, it is not clear in advance which stars cool down faster: with the C- or B-type neutron superfluidity in the NS core. If we introduce the critical nucleon temperatures $T_{\rm cn}$ and $T_{\rm cp}$ for the characteristic density under consideration, then, depending on $T_{\rm cn}$ and $T_{\rm cp}$, the function $\log[Q_C C_B/(Q_B C_C)]$ will be convenient for understanding when the cooling for cases C and B proceeds almost identically and when the differences are at a maximum.

Let us examine Fig. 1. It consists of six pictures, each corresponding to a certain temperature ($T = 10^8, 3 \times 10^8$, or 10^9 K) and density ($\rho = 2\rho_0$, $5\rho_0$). The direct Urca process is forbidden at $\rho = 2\rho_0$ and permitted at $\rho = 5\rho_0$. Our calculations show that when the temperatures and densities are varied, the pictures do not change fundamentally until the threshold density ρ_D at which the direct Urca process switches on (or off) is crossed. The logarithms of the critical proton and neutron temperatures at a fixed density are plotted along the vertical and horizontal axes of each picture, respectively. The critical nucleon temperatures lower than 10^7 K (weak superfluidity) have virtually no effect on the NS cooling and, hence, are not considered. In the figure, the function $\log[Q_C C_B/(Q_B C_C)]$ is indicated by different shades of gray. The shade of gray for the region of critical temperatures to the left from the vertical dashed line (nonsuperfluid neutrons) corresponds to the zero of this function. The darker the shade of gray, the larger $\log[Q_C C_B/(Q_B C_C)]$. For example, for $T = 10^8$ K, the maximum of this function reaches 6–7

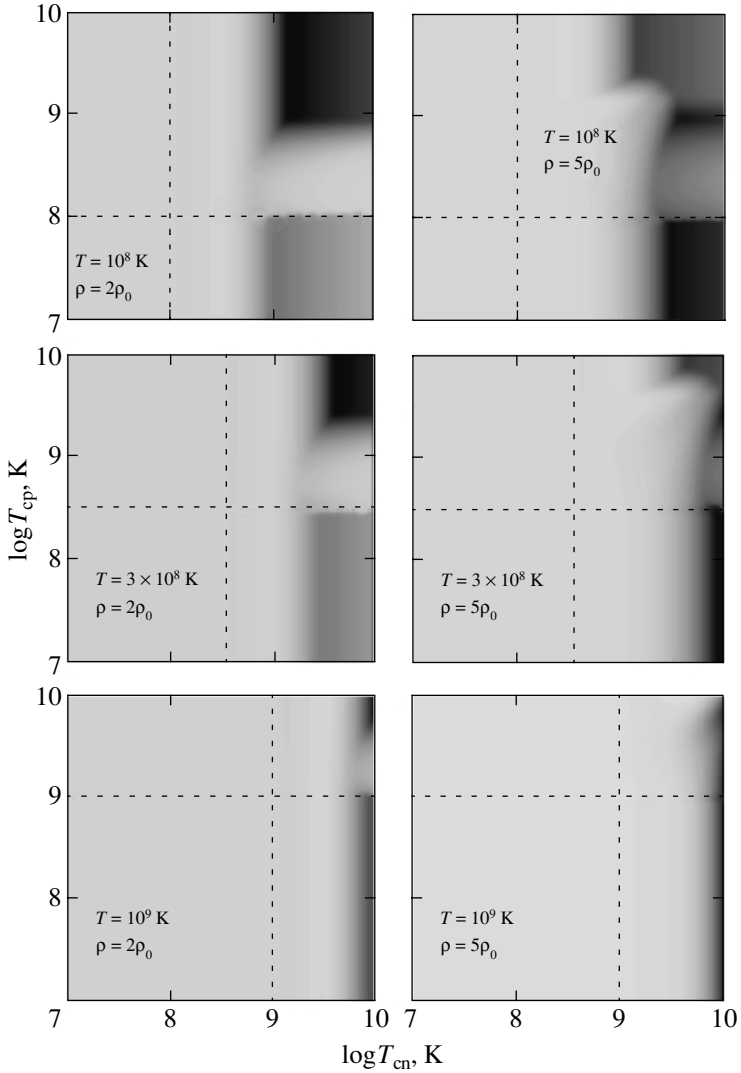

Fig. 1. The function $\log[Q_C C_B/(Q_B C_C)]$ over a wide range of T_{cn} and T_{cp} is indicated by different shades of gray. The larger the value of the function, the darker the shade.

for critical proton and neutron temperatures $T_{cp,cn} \sim 10^9$–10^{10} K at $\rho = 2\rho_0$ and 8–9 for $T_{cp} \sim 10^7$–10^8 K, $T_{cn} \sim 3 \times 10^9$ –10^{10} K at $\rho = 5\rho_0$. Conversely, the lighter the shade of gray relative to the "zero" shade, the smaller the function. The region with the shade of gray lighter than the "zero" shade is narrow and lies near $T_{cn} \sim 3T$. In this region, the minimum value of the function is of the order of -1 for both densities. A further increase in the internal NS temperature causes the differences between the B- and C-type neutron superfluidities to be smoothed out; the smoothing occurs faster for the densities at which the direct Urca process is open. Thus, for $T = 10^9$ K, the maximum of $\log[Q_C C_B/(Q_B C_C)]$ is (3–3.5) for $\rho = 2\rho_0$ and (1–1.2) for $\rho = 5\rho_0$, while its minimum is nearly zero for both densities. Summing up our results, we may say that the inequality $(dT/dt)_C \geq (dT/dt)_B$ holds for any T, T_{cn}, T_{cp}, and ρ. Therefore, one can hardly expect the NS cooling curve for case C to pass well above the cooling curve for case B (at fixed T_{cn} and T_{cp}). Clearly, the reverse can be easily realized by appropriately (see above) choosing the critical temperatures.

Let us now turn directly to an examination of the NS cooling curves. For simplicity, the neutrons in the stellar crust are assumed to be nonsuperfluid. This assumption has no effect on the difference between the cooling curves for the B- and C-type neutron superfluidities in the NS core. Although the critical nucleon temperatures $T_{cn}(\rho)$ and $T_{cp}(\rho)$ are actually functions of the density and vary along the stellar radius, it was noticed that following certain semiempirical recipes, constant (over the core) critical temperatures can be matched to them. In this case, the

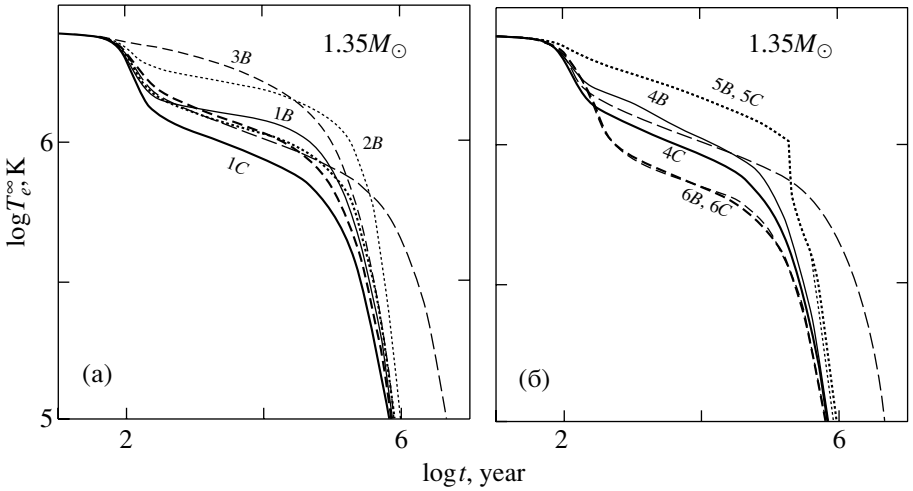

Fig. 2. The cooling curves constructed for the B- and C-type neutron superfluidities in NS cores for various critical nucleon temperatures. The curves with identical $T_{\rm cn}$ and $T_{\rm cp}$ but for different superfluidities, B or C, are represented by the same type of lines (solid, dotted, and dashed lines). The long dashes correspond to the cooling without superfluidity. The NS mass is $M = 1.35M_\odot$.

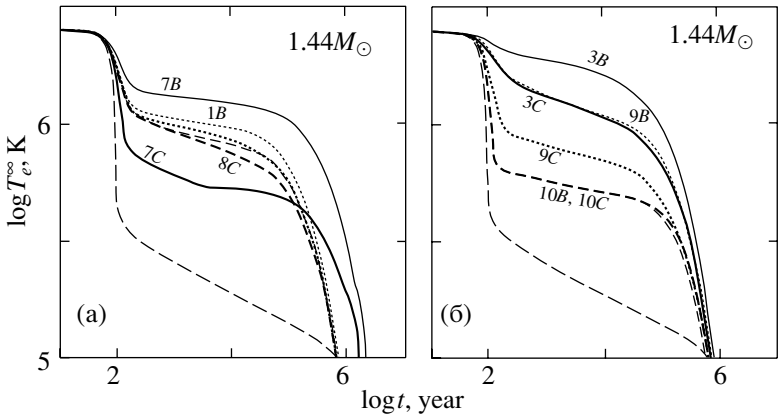

Fig. 3. Same as Fig. 2 for $M = 1.44M_\odot$.

cooling curves remain the same as when we take into account the exact dependence $T_{\rm cn}(\rho)$ and $T_{\rm cp}(\rho)$ (e.g., for protons, a constant effective temperature $T_{\rm cp}$ close to $T_{\rm cp}(\rho_c)$, where ρ_c is the central density of the star, always corresponds to the temperature profile $T_{\rm cp}(\rho)$). Therefore, for simplicity, we assume the critical nucleon temperatures to be density-independent.

Figures 2 and 3 show the cooling curves constructed for two NS masses: $M = 1.35M_\odot$ (Fig. 2) and $M = 1.44M_\odot$ (Fig. 3). The direct Urca process is forbidden for $M = 1.35M_\odot$ and permitted for $M = 1.44M_\odot$. Below, we give the various critical nucleon temperatures $T_{\rm cn}$ and $T_{\rm cp}$ for which the cooling curves were constructed.

Number	1	2	3	4	5	6	7	8	9	10	11	12
$T_{\rm cn}/10^9$, K	2.5	5.0	10.0	3.2	0.2	0.5	7.0	0.85	9.5	0.2	0.1	5.0
$T_{\rm cp}/10^9$, K	2.5	0.25	10.0	0.6	5.0	1.0	0.01	3.0	0.85	0.7	5.0	0.01

Each pair of critical temperatures in the table has its own number. In Figs. 2–4, the cooling curves are marked by these numbers. The letter B or C near the number specifies the type of neutron superfluidity. For example, $3C$ means that the cooling curve was constructed for the C-type neutron superfluidity for

the critical temperatures $T_{\rm cn}$ and $T_{\rm cp}$ under number 3. We see from analysis of Figs. 2 and 3 that all our main conclusions drawn from an examination of Fig. 1 are confirmed. For $M = 1.35M_\odot$, the largest differences are observed for the $3B$ and $3C$ curves in Fig. 2a (high critical temperatures). At critical proton temperatures $T_{\rm cp} \sim 5 \times 10^8$ K, the neutrino emission during Cooper proton pairing is the most powerful process in the NS core. Accordingly, the differences between the cooling curves for cases B and C decrease. This can be verified by comparing the $4B$ and $4C$ curves in Fig. 2b. As the critical proton temperatures decrease to $T_{\rm cp} \lesssim 3 \times 10^8$ K and for $T_{\rm cn} \gtrsim 10^9$ K (but $T_{\rm cn} \lesssim 10^{10}$ K), the differences again increase (the $2B$ and $2C$ curves in Fig. 2a). When $T_{\rm cn} \gtrsim 10^{10}$ K and increases, the differences gradually decrease and the cooling curves for the B- and C-type neutron paring coincide for $T_{\rm cn} \sim 10^{11}$ K. At moderately high critical temperatures $T_{\rm cn} < 10^9$ K, the curves for case B almost coincide with those for case C (see, e.g., Fig. 2b: $5B$, $5C$ or $6B$, $6C$). The kink in the $5B$ and $5C$ curves occurs at $T = T_{\rm cn}$ and stems from the fact that the neutrino emission due to Cooper neutron pairing switches on. Note that the critical temperatures of the $6B$ and $6C$ curves exactly fall within the region where the temperature for the B-type neutron superfluidity decreases faster than that for case C ($\log[Q_C C_B/(Q_B C_C)] < 0$). This actually leads to the fact that the $6B$ curve initially passes slightly below the $6C$ curve. Subsequently, as the internal temperature T decreases, the situation is reversed, because we reach the regions with faster cooling for the C-type superfluidity (see Fig. 1).

For $M = 1.44M_\odot$, the differences are largest for the $7B$ and $7C$ curves in Fig. 3a, i.e., at high critical neutron temperatures and at low critical proton temperatures. As $T_{\rm cn}$ decreases, the differences between the cooling curves for the B- and C-type superfluidities gradually disappear (see Fig. 3a: $8B$ and $8C$; Fig. 3b: $10B$, $10C$). The remaining remarks almost completely repeat those for $M = 1.35M_\odot$.

Our results can be of use in explaining observational data. The NS cooling with weak B-type neutron superfluidity was considered by Kaminker *et al.* (2002). The authors showed that the available observational data on the thermal radiation from eight isolated NSs could be explained by assuming strong proton ($T_{\rm cp,max} \gtrsim 5 \times 10^9$ K) and weak neutron ($T_{\rm cn,max} \lesssim 10^8$ K) superfluidities. In this case, the critical temperatures $T_{\rm cp}$ and $T_{\rm cn}$ must depend on density ρ [have a maximum at $\rho \sim (2\text{–}3)\,\rho_0$, as predicted by microscopic theories of superfluidity; see, e.g., Lombardo and Schulze (2001)]. Strong proton and weak neutron superfluidities are primarily needed to interpret the observations of

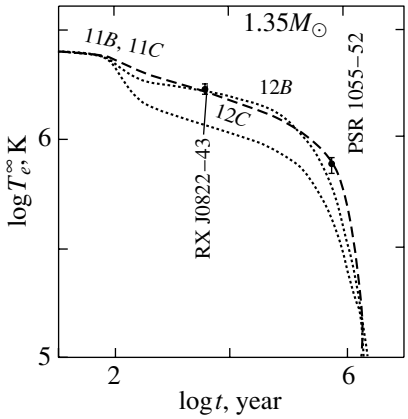

Fig. 4. The cooling curves for the models with the B- and C-type neutron superfluidities in the core of a NS with $M = 1.35M_\odot$ and observational data on the surface temperatures of two sources. The dashed curves are for $T_{\rm cn} = 10^8$ K and $T_{\rm cp} = 5 \times 10^9$ K; the dotted curves are for $T_{\rm cn} = 5 \times 10^9$ K and $T_{\rm cp} = 10^7$ K.

two sources, RX J0822–43 (Zavlin *et al.* 1999) and PSR 1055–52 (Ögelman 1995), which are the hottest for their age. The observational data on these sources are shown in Fig. 4 [we took the same T_e^∞ and t as those used by Kaminker *et al.* (2002)]. Until recently, in addition to these two sources, yet another source, RX J185635–3754, had to be considered (Pons *et al.* 2002; Burwitz *et al.* 2001; Gänsicke *et al.* 2001; Kaplan *et al.* 2001). However, in the just published paper by Walter and Lattimer (2002), the age of RX J185635–3754 was revised (reduced by almost half) and is now estimated to be $t \approx 5 \times 10^5$ yr, which is attributable to a decrease in the distance to this source.

When comparing observations with cooling models, we should take into account the fact that the surface temperatures and ages of isolated cooling NSs are determined with a low accuracy [for the reasons discussed, e.g., by Pavlov and Zavlin (1998) and Yakovlev *et al.* (1999)]. The NS age t is probably known to within a factor $\sim$2.

Since the determination of T_e^∞ and t is ambiguous, we can offer an alternative interpretation of the observations to that offered by Kaminker *et al.* (2002). More specifically, if we take the lowest possible values of T_e^∞ and t for PSR 1055–52, then the observations of the eight NSs considered by Kaminker *et al.* (2002) can be interpreted by assuming strong neutron superfluidity and weak proton superfluidity in the stellar cores. Although this interpretation is less plausible than that offered by Kaminker *et al.* (2002) (according to microscopic calculations of $T_{\rm cn}(\rho)$ and $T_{\rm cp}(\rho)$, the triplet neutron pairing is generally weaker than the single proton

pairing), it cannot be ruled out in advance and should be studied. It actually requires lower values of T_e^∞ and t of the fairly old and hot source PSR 1055–52, because strong neutron superfluidity significantly reduces the NS heat capacity and speeds up the NS cooling at the late photon cooling stage [implying that the models by Kaminker *et al.* (2002) can describe older and hotter sources].

A detailed discussion of the hypothesis of strong neutron superfluidity and weak proton superfluidity in NS cores is beyond the scope of this paper and will be given in the future publication. Here, we only illustrate the possibility of this interpretation of observations for the two hottest sources (RX J0822–43 and PSR 1055–52) by using simplified models of cooling NSs with critical temperatures $T_{\rm cn}(\rho)$ and $T_{\rm cp}(\rho)$ constant over the stellar core. The dotted lines in Fig. 4 represent the cooling curves for $T_{\rm cn} = 5 \times 10^9$ K and $T_{\rm cp} = 10^7$ K. For comparison, a dashed line was drawn for strong proton superfluidity and weak neutron superfluidity ($T_{\rm cp} = 5 \times 10^9$ K, $T_{\rm cn} = 10^8$ K). It virtually coincides with the cooling curve obtained by Kaminker *et al.* (2002) to interpret the above two sources. We see that the upper dotted line (B-type neutron superfluidity) almost coincides with the dashed line for $t \lesssim 10^5$ yr and passes slightly below the dashed line for $t \gtrsim 10^5$ yr (because of the above suppression of the neutron heat capacity by strong neutron superfluidity). Nevertheless, given the inaccurate determination of T_e^∞ and t, the upper dotted line could be assumed to satisfactorily explain these two sources. At the same time, the lower dotted line for strong C-type neutron superfluidity passes well below (because of the weaker suppression of neutrino emission by the C-type superfluidity) and cannot be considered to be acceptable. Therefore, the observations can (with the above reservations) be explained by strong B-type neutron superfluidity but cannot be explained by the C-type neutron superfluidity with the same $T_{\rm cn} = 5 \times 10^9$ K. With a further increase in $T_{\rm cn}$, the upper dotted line would not change at all (strong B-type neutron superfluidity with $T_{\rm cn} \sim 5 \times 10^9$ K almost completely switched off the neutrino reactions involving neutrons and made the neutron heat capacity equal to zero), while the lower dotted line would slowly approach the upper curve (the C-type neutron superfluidity increasingly suppresses the neutrino luminosity and heat capacity), reaching it at $T_{\rm cn} \sim 10^{11}$ K. Thus, the interpretation of the observations in the model of strong C-type neutron superfluidity is possible in principle but is implausible, because it requires unrealistically high values of $T_{\rm cn} \sim 10^{11}$ K.

CONCLUSIONS

The cooling of NSs with C-type neutron superfluidity in their cores has been consistently studied for the first time. The critical nucleon temperatures were assumed to be constant over the stellar core. A comparison with B-type neutron superfluidity was made. We found that the cooling curves for case C can pass well below the cooling curves for case B (faster cooling). Otherwise, the curves differ only slightly. The cooling with variable (over the core) critical temperatures $T_{\rm cn}(\rho)$ and $T_{\rm cp}(\rho)$ can generally be described by the cooling with some effective constant temperatures $T_{\rm cn}$ and $T_{\rm cp}$.

The model with C-type neutron superfluidity can account for the observational data on the thermal radiation from isolated NSs by assuming strong proton superfluidity ($T_{\rm cp} \gtrsim 5 \times 10^9$ K) and weak neutron superfluidity ($T_{\rm cn} \lesssim 10^8$ K). The interpretation of the observations in terms of the model with strong neutron superfluidity and with weak proton superfluidity ($T_{\rm cp} \lesssim 10^8$ K) is unlikely (in contrast to the same model for case B), because it requires exceedingly high critical neutron temperatures, $T_{\rm cn} \sim 10^{11}$ K. Our results can be useful in understanding which type of superfluidity (B or C) occurs in nature.

ACKNOWLEDGMENTS

One of us (M.E. Gusakov) is grateful to D.G. Yakovlev and A.D. Kaminker for helpful discussions and attention to the work. This study was supported in part by the Russian Foundation for Basic Research (project nos. 02-02-17668 and 00-07-90183).

REFERENCES

1. V. Burwitz, V. E. Zavlin, R. Neuhäuser, *et al.*, Astron. Astrophys. **379**, L35 (2001).
2. B. T. Gänsicke, T. M. Braje, and R. W. Romani, astro-ph/0110130 (2001).
3. M. E. Gusakov, astro-ph/0204334 (2002).
4. A. D. Kaminker, D. G. Yakovlev, and O. Y. Gnedin, Astron. Astrophys. **383**, 1076 (2002).
5. D. L. Kaplan, M. H. van Kerkwijk, and J. Anderson, astro-ph/0111174 (2001).
6. J. M. Lattimer and M. Prakash, Astrophys. J. **550**, 426 (2001).
7. U. Lombardo and H.-J. Schulze, in *Physics of Neutron Star Interiors,* Ed. by D. Blaschke, N. Glendenning, and A. Sedrakian (Springer-Verlag, Berlin, 2001), p. 30.
8. J. W. Negele and D. Vautherin, Nucl. Phys. A **207**, 298 (1973).

9. H. Ögelman, in *Proceedings of the NATO Advanced Study Institute on The Lives of Neutron Stars, Kemer, 1993,* Ed. by M. A. Alpar, Ü. Kiziloğlu, and J. van Paradijs (Kluwer, Dordrecht, 1995), p. 101.
10. G. G. Pavlov and V. E. Zavlin, in *Neutron Stars and Pulsars,* Ed. by N. Shibazaki, N. Kawai, S. Shibata, and T. Kifune (Universal Academy Press, Tokyo, 1998), Vol. 24, p. 327.
11. J. Pons, F. Walter, J. Lattimer, *et al.*, Astrophys. J. **564**, 981 (2002).
12. A. Y. Potekhin, G. Chabrier, and D. G. Yakovlev, Astron. Astrophys. **323**, 415 (1997).
13. M. Prakash, T. L. Ainsworth, and J. M. Lattimer, Phys. Rev. Lett. **61**, 2518 (1988).
14. Ch. Schaab, F. Weber, and M. K. Weigel, Astron. Astrophys. **335**, 596 (1998).
15. F. M. Walter and J. Lattimer, astro-ph/0204199 (2002).
16. D. G. Yakovlev, K. P. Levenfish, and Yu. A. Shibanov, Usp. Fiz. Nauk **169**, 825 (1999).
17. D. G. Yakovlev, A. D. Kaminker, O. Y. Gnedin, and P. Haensel, Phys. Rep. **354**, 1 (2001).
18. V. E. Zavlin, J. Trümper, and G. G. Pavlov, Astrophys. J. **525**, 959 (1999).

Translated by V. Astakhov

Astronomy Letters, Vol. 28, No. 10, 2002, pp. 676–690. Translated from Pis'ma v Astronomicheskiĭ Zhurnal, Vol. 28, No. 10, 2002, pp. 748–763.

Analysis of HST Ultraviolet Spectra for T Tauri Stars: DR Tau

A. S. Kravtsova and S. A. Lamzin*

Sternberg Astronomical Institute, Universitetskiĭ pr. 13, Moscow, 119992 Russia

Received April 24, 2002

Abstract—We analyze the spectra of DR Tau in the wavelength range 1200 to 3100 Å obtained with the GHRS and STIS spectrographs from the Hubble Space Telescope. The profiles for the C IV 1550 and He II 1640 emission lines and for the absorption features of some lines indicate that matter falls to the star at a velocity ≈300 km s^{-1}. At the same time, absorption features were detected in the blue wings of the N I, Mg I, Fe II, Mg II, C II, and Si II lines, suggesting mass outflow at a velocity up to 400 km s^{-1}. The C II, Si II, and Al II intercombination lines exhibit symmetric profiles whose peaks have the same radial velocity as the star. This is also true for the emission features of the Fe II and H_2 lines. We believe that stellar activity is attributable to disk accretion of circumstellar matter, with matter reaching the star mainly through the disk and the boundary layer. At the time of observations, the accretion luminosity was $L_{ac} \simeq 2L_\odot$ at an accretion rate $\simeq 10^{-7} M_\odot$ yr^{-1}. Concurrently, a small (< 10%) fraction of matter falls to the star along magnetospheric magnetic field lines from a height $\sim R_*$. Within a region of size $\simeq 3.5R_*$, the disk atmosphere has a thickness $\sim 0.1R_*$ and a temperature $\simeq 1.5 \times 10^4$ K. We assume that disk rotation in this region significantly differs from Keplerian rotation. The molecular hydrogen lines are formed in the disk at a distance <1.4 AU from the star. Accretion is accompanied by mass outflow from the accretion-disk surface. In a region of size $<10R_*$, the wind gas has a temperature ~7000 K, but at the same time, almost all iron is singly ionized by H I L_α photons from inner disk regions. Where the warm-wind velocity reaches ≃400 km s^{-1}, the gas moves at an angle of no less than 30° to the disk plane. We found no evidence of regions with a temperature above 10^4 K in the wind and leave open the question of whether there is outflow in the H_2 line formation region. According to our estimate, the star has the following set of parameters: $M_* \simeq 0.9M_\odot$, $R_* \simeq 1.8R_\odot$, $L_* \simeq 0.9L_\odot$, and $A_V \simeq 0^m.9$. The inclination i of the disk axis to the line of sight cannot be very small; however, $i \leq 60°$. © *2002 MAIK "Nauka/Interperiodica"*.

Key words: *T Tauri stars, disk accretion, stellar wind, DR Tau.*

INTRODUCTION

Here, we continue to analyze the ultraviolet (UV) spectra for T Tauri stars from the Hubble Space Telescope (HST). We deal with DR Tau, a classical T Tauri star (CTTS): the equivalent width of the Hα line in its spectrum varies over the range 60 to 100 Å (Smith *et al.* 1999). Since the distance to the star is not known with certainty, we take it to be equal to the mean distance to the Tau–Aur star-forming region, i.e., 140 pc (Elias 1978).

The brightness of DR Tau varied greatly throughout the 20th century. Before the early 1970s, the star smoothly faded from $B \simeq 12^m.5$ to $B \simeq 16^m$; subsequently, it brightened by $\Delta B \simeq 3$–5^m in several months. Since the early 1980s, the star has exhibited erratic variability with an amplitude up to 2^m at a mean magnitude $B \simeq 11^m.8$) [see Chavarria-K (1979) and the database at ftp://www.astro.wesleyan.edu/pub/ttauri (Herbst *et al.* 1994)]. Attempts to distinguish a periodicity in the variability yielded periods from 2.8 to 9.0 days [see Bouvier *et al.* (1995) and references therein].

Joe (1949) estimated the spectral type of the star to be K5 Ve. Appenzeller *et al.* (1988) specially emphasized that there were no TiO bands in the spectrum of DR Tau and that the continuum dip near 6159 Å was attributable to a blend of Ca I, Fe I, and Na I lines rather than to TiO, which probably rules out a spectral type appreciably later than K5. Nevertheless, several papers appeared in the 1990s (see, e.g., Guenther and Hessman 1993; Valenti *et al.* 1993) after which the spectral type of the star is commonly assumed to be K7–M0, although no TiO bands have ever been detected.

The problem stems from the fact that the photospheric spectrum of DR Tau is strongly veiled by the emission continuum, whose intensity can exceed the intensity of the photospheric emission by more than an order of magnitude at optical wavelengths (Beristain *et al.* 1998) and by more than

*E-mail: lamzin@sai.msu.ru

a factor of 5 in the infrared ($\lambda = 2.2$ μm) (Johns-Krull and Valenti 2001). The star's light variability is attributable to intensity variations of the veiling continuum and is accompanied by variations in the equivalent widths of not only absorption lines but also emission lines (Smith *et al.* 1999; Alencar *et al.* 2001).

The uncertainty in the spectral type of the star leads to a large spread in the estimates of interstellar extinction A_V toward DR Tau: White and Ghez (2001), Basri and Bertout (1989), and Hartigan *et al.* (1995) obtained $0\overset{m}{.}5$, $0\overset{m}{.}95$, and $3\overset{m}{.}2$, respectively. The spread in the estimates of the stellar mass (from 0.4 to 1.0 $M_\odot$) and radius (from 1.6 to 2.6 $R_\odot$) is also large.

The optical spectrum of DR Tau shows more than a hundred emission lines of hydrogen, neutral and singly ionized metals, and He I and He II (Joe 1949; Bertout *et al.* 1977). The profile shape for these lines can change greatly on a time scale of the order of an hour (Smith *et al.* 1999). Quasi-periodic variations in line shapes and equivalent widths on a time scale of the order of several days were recorded but no single period was found (Alencar *et al.* 2001). The appearance and disappearance of absorption features in the blue and red wings have been repeatedly observed in the hydrogen and Na D lines [see Alencar *et al.* (2001) and references therein]. Absorption features are occasionally also seen in the red wings of the Fe II and He I lines (Guenther and Hessman 1993; Beristain *et al.* 1998). The profile of the He II 4686 line is asymmetric and appreciably redshifted (Lamzin 1991).

These results are unanimously interpreted as evidence for unsteady accretion of circumstellar matter accompanied by gas outflow from the neighborhoods of the star. Estimates of the accretion rate differ greatly: 9×10^{-8} $M_\odot$ yr^{-1} (Basri and Bertout 1989), 3×10^{-7} $M_\odot$ yr^{-1} (Gullbring *et al.* 2000), and 9×10^{-6} $M_\odot$ yr^{-1} (Hartigan *et al.* 1995). The differences are attributable not so much to the variability of DR Tau as to the uncertainty in estimates of the stellar parameters and interstellar extinction.

The bulk of the radiation from DR Tau is emitted in the infrared. If judged by a single IRAS measurement (Weaver and Jones 1992), then even the flux in the wavelength range 12–100 μm exceeds the visible flux at the star's mean brightness (Kenyon and Hartmann 1995). The variability amplitude decreases with increasing λ, but the light variations in the range 0.4 to 3.4 μm are correlated (Kenyon *et al.* 1994). At a distance $>0\overset{''}{.}02$, i.e., more than $\simeq$3 AU, DR Tau has no infrared companion comparable in brightness to the primary star (Leinert *et al.* 1993; Simon *et al.* 1999; White and Ghez 2001).

The low-resolution ($\Delta\lambda \sim 6$ Å) IUE UV spectra of the star in the range 1200 to 3100 Å were described by Appenzeller *et al.* (1980), Gómez de Castro and Franqueira (1997), and Valenti *et al.* (2000). Apart from the C IV 1550, He II 1640, and other emission lines, strong Fe II and Mg I absorption lines were detected in the UV spectrum of the star. When our work was nearing completion, the papers by Ardila *et al.* (2002a, 2002b) appeared. These authors investigated separate portions of the UV spectrum for DR Tau obtained with the GHRS spectrograph from the HST. We mainly analyze the UV spectrograms taken with the more sophisticated STIS spectrograph, which was installed on the HST to replace GHRS in 1996.

OBSERVATIONAL DATA

The spectra analyzed below were taken from the HST archival database (http://archive.stsci.edu/hst/target_descriptions.html). They were reduced by means of the IRAF v2.11 (http://archive.stsci.edu/hst/target_descriptions.html) and STSDAS/TABLES v2.0.2 (http://ra.stsci.edu/STSDAS.html) software packages. We applied the standard procedures described in Chapters 21 and 36 of the HST Data Handbook (http://www.stsci.edu/documents/data-handbook.html); the files recommended in the archival database were used for calibration.

We analyzed all of the archival UV spectra for DR Tau observed before 2001. The first group of spectra were taken on August 5, 1993, and September 7, 1995, with the GHRS spectrograph (Ardila *et al.* 2002a, 2002b). Unfortunately, the signal-to-noise (S/N) ratio for these spectra is comparatively high only near 2800 Å.

The second group of spectra were taken with the STIS spectrograph in intermediate-resolution echelle mode on August 29, 2000. The spectra were obtained in accumulation mode with a $0\overset{''}{.}2 \times 0\overset{''}{.}2$ aperture. In this mode, STIS has approximately the same resolution as GHRS but its spectral range is almost a factor of 30 larger. The quality of the STIS spectra for DR Tau is appreciably higher than that of the GHRS spectra but it still leaves a lot to be desired. The errors near the edges of echelle orders are particularly large.

The table provides information on the STIS spectra taken on August 29, 2000; similar information on the GHRS spectra is available in Table 2 from Ardila *et al.* (2002a). The table gives the following: exposure start times, to within a minute (UT); spectrum codes in the archive; diffraction gratings used; and spectral ranges covered. Part of the observational time was

Information on the HST/STIS observations of DR Tau on August 29, 2000

t_0, UT	Spectrum code	Grating	$\Delta\lambda$, Å	Object
14:35	o5cf02010	E230M	1574–2382	W_Cal
14:36	o5cf02010	E230M	1574–2382	DR Tau
14:58	o5cf02020	E230M	2303–3111	W_Cal
15:00	o5cf02020	E230M	2303–3111	DR Tau
16:01	o5cf02030	E140M	1140–1735	W_Cal
16:02	o5cf02030	E140M	1140–1735	DR Tau
16:53	o5cf02040	E140M	1140–1735	W_Cal
17:39	o5cf02040	E140M	1140–1735	DR Tau

spent on taking calibration spectra, designated as W_Cal. The wavelengths are everywhere given for a vacuum at $\lambda < 2000$ Å and for air at $\lambda > 2000$ Å. To improve the S/N ratio and for better clarity, the data in the figures were generally smoothed by a 4-to-16 point moving average. Therefore, the formal resolution of these spectrograms is lower than that of the original spectrograms, for which $\Delta V \simeq 4$ km s^{-1}, by the corresponding number of times. Only for the molecular hydrogen lines did the smoothing appreciably change the profile width (see below).

THE CLASSIFICATION OF SPECTRAL LINES BY THE SHAPE OF THEIR PROFILES

Since the STIS spectra are much more informative than the GHRS spectra (Ardila *et al.* 2002a, 2002b), we deal only with the former.

Figure 1 shows the star's spectrum in the wavelength range 1200–3000 Å, except for the portions with a low S/N ratio. The spectral flux density, in units of 10^{-14} erg s^{-1} cm^{-2} Å^{-1}, is along the y axis. In general, the echelle orders slightly overlap, but occasionally there are small gaps between the orders. The solid line represents the continuum level; the technique for its determination is described below.

In total, we identified more than a hundred emission and absorption lines in the spectrum of DR Tau. For convenient interpretation, let us consider successively the groups of lines with similar profiles. The profiles of all the lines discussed in this section are shown in Fig. 2. They were all normalized to the continuum level and corrected for the radial velocity of the star, $V_r = 23$ km s^{-1} (Appenzeller *et al.* 1988; Edwards 2000). An exception was made only for the L_α line.

The emission lines of the "high-temperature" C IV and He II ions with highly redshifted profiles form the first group. We constructed the profiles of the C IV $\lambda = 1548.20$ and 1550.77 Å lines by averaging two spectra taken 1.5 h apart (our analysis indicates that the differences between the individual profiles are statistically insignificant). The profile of the He II 1640.4 line is also redshifted, although to a much lesser extent than for the carbon line. To all appearances, the lines of this group originate in the matter falling to the star; judging by the C IV lines, the infall velocity slightly exceeds 300 km s^{-1} (see also Ardila *et al.* 2002a). Note that the Si IV 1393.75 and 1402.77 lines are very weak in the spectrum of DR Tau: they are virtually indistinguishable against the background of the H_2 lines (Fig. 1).

The emission lines whose profiles are almost symmetric with the peaks near zero velocity relative to the star form the second group. This group includes the following lines : Al II] 2669.35, C II] 2325 (the $2s^2\ 2p\ ^2P–2s\ 2p^2\ ^4P$ multiplet), Si II] 2350 (the $3s^2\ 3p\ ^2P–3s\ 3p^2\ ^4P$ multiplet), Si II 1810 (the uv 1 triplet), S I] 1471.83, and all molecular hydrogen lines. Figure 2 shows the profiles of the strongest lines from this group: C II 2325.40, Si II 1808.01, and H_2 1504.76; in contrast to the ion lines, the molecular hydrogen line profile is shown without smoothing and its intensity was reduced by a factor of 3 for clarity. We see that while the profiles are identical in shape, the line full widths at half maximum (FWHM) differ markedly: FWHM $\simeq$ 80–100 km s^{-1} for the ions and FWHM $\simeq$ 20 km s^{-1} for the H_2 lines.

Because of the low S/N ratio even after 16-point smoothing, we cannot judge whether the O III] 1666.15, Si III] 1892.03, and C III] 1908.73 lines, whose profiles are also shown in Fig. 2, belong to this group. Nevertheless, we may assert that the red and blue wings of these lines extend to no less than 150 km s^{-1}.

As in the optical wavelength range, there are lines in the UV spectra of DR Tau that originate in the matter moving away from the star. The h and k lines of the Mg II 2800 (uv 1) resonance doublet can serve as the clearest illustration: using the h line as an example, we see that, apart from the comparatively narrow absorption feature attributable to interstellar extinction, these lines exhibit a broad absorption feature that spans the radial-velocity range up to 400 km s^{-1}. For comparison, the dotted line represents the h-line profile in the star's spectrum observed on September 7, 1995. The decrease in the intensity of the emission feature was accompanied by a reduction in the extent of the absorption feature by approximately 50 km s^{-1}. The profiles of the absorption features in the h and k lines are identical but the emission feature in the h line is less intense.

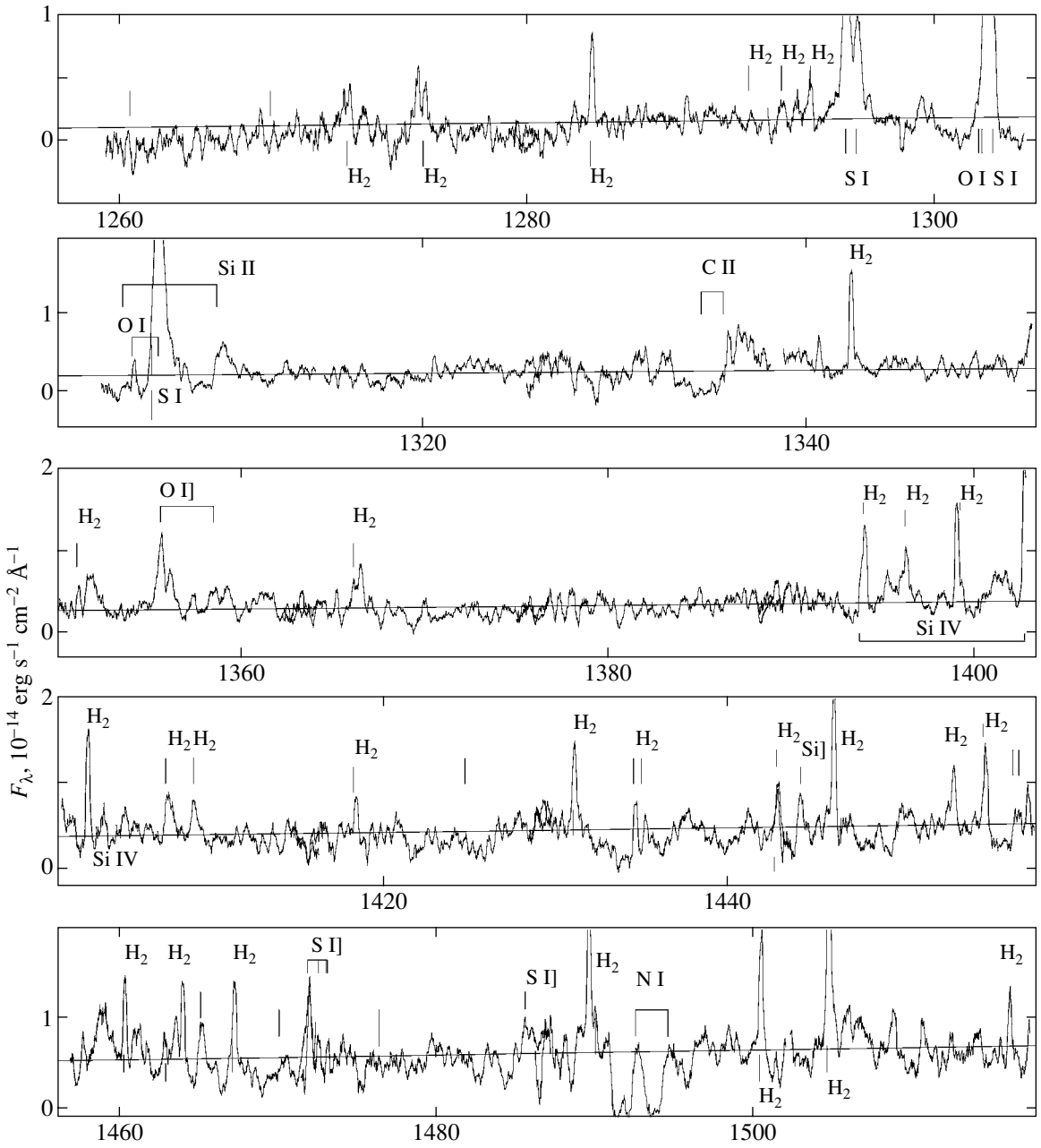

Fig. 1. The STIS spectrum of DR Tau in the wavelength range 1200–3000 Å taken in 2000. The spectral flux density, in units of 10^{-14} erg s^{-1} cm^{-2} Å^{-1}, is along the y axis. The positions of the identified lines are marked, and the numerous unlabeled vertical bars correspond to Fe II lines. The continuum level is indicated by the solid line.

Apart from the Mg II h and k lines, the Si II 1309.28 and C II uv1 ($\lambda \simeq 1335$ Å) doublet resonance lines also have P Cyg profiles (see Fig. 1). The extent of the absorption features in these lines is ≥ 300 km s^{-1}.

The spectrum of DR Tau exhibits yet another Mg II line with a qualitatively different profile, the $\lambda 2790.84$ Å emission line of the subordinate uv 3 multiplet whose profile is shown in Fig. 2. The intensity of this line is abnormally high: it is more than an order of magnitude higher than the intensities of the other two uv 3 triplet lines and only several times weaker than the h and k resonance lines. The blue wing of the line appears more extended than its red wing, but this may result from blending with the absorption wing of the k line.

The Fe II lines are most numerous in the stellar spectrum: we see from Fig. 1 that they fill the entire UV range, often superimposing on one another and

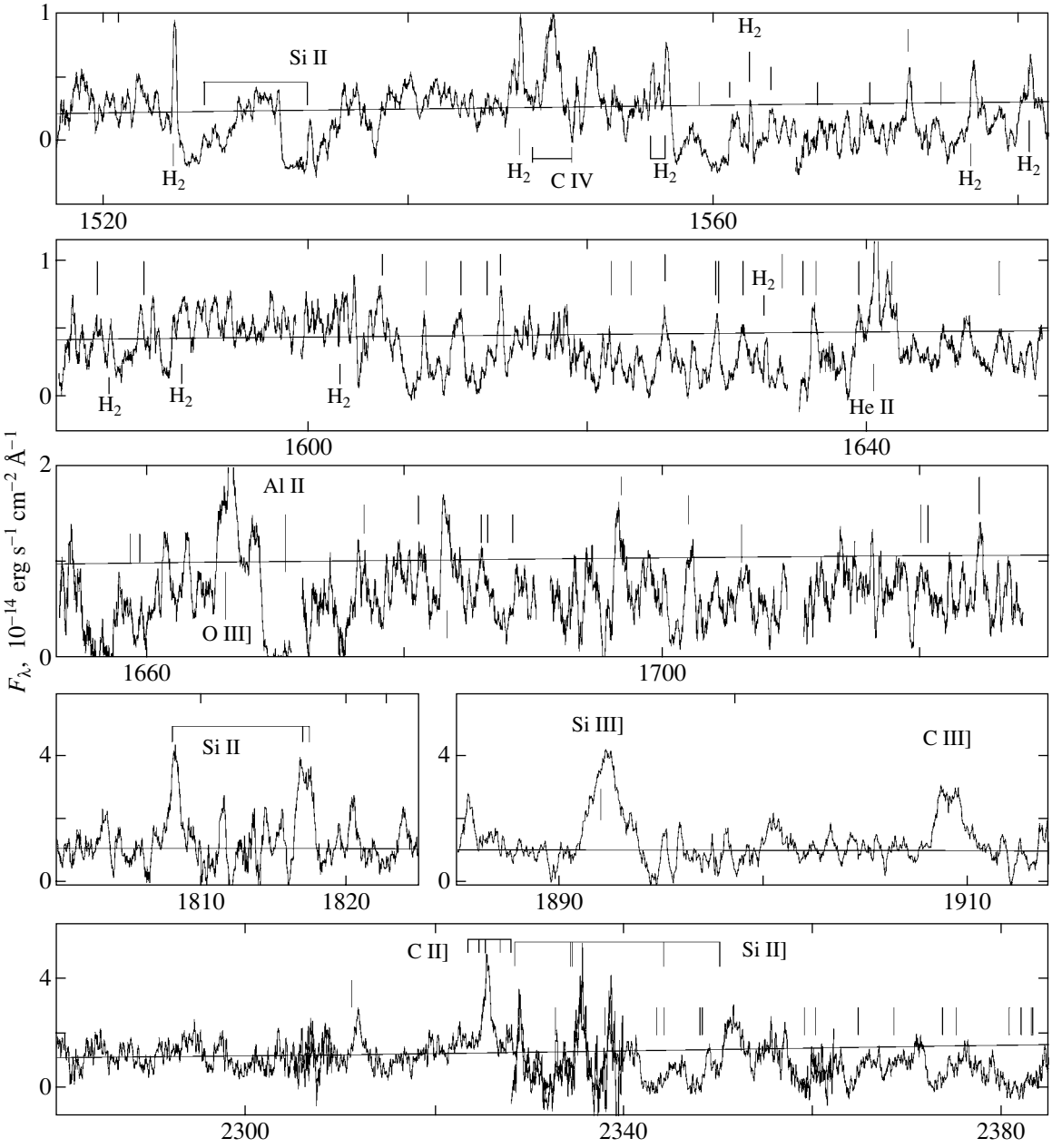

Fig. 1. (Contd.)

on lines of other elements. In general, these are the lines for which the lower-level excitation potential E_i does not exceed 1.7 eV (the a^6D, a^4F, a^4D, and a^4P terms). The strong uv 234 multiplet lines near 2790 Å, for which $E_i \simeq 3.2$ eV, constitute an exception. We were unable to reliably identify any Fe I line, even though neutral iron lines are very intense in the optical wavelength range (Beristain *et al.* 1998).

The Fe II line profiles have a complex structure: in most cases, they show an absorption dip both to the right and to the left from the central wavelength λ_0. We see from the lines at λ2585.88, 2783.69, and 3002.65 Å that the depth of the blue absorption dip in the Fe II lines decreases with increasing λ_0, while the depth of the red absorption dip increases. At the same time, a symmetric emission peak centered at λ_0 emerges in the lines. This tendency is consistent with optical observations: Beristain *et al.* (1998) point out that the visible Fe II lines generally appear as unshifted symmetric emission peaks and only in some of them does the red absorption wing occasionally emerge, while no absorption has ever been observed in the blue wing.

The profiles of the N I 1492.62, 1494.68 doublet

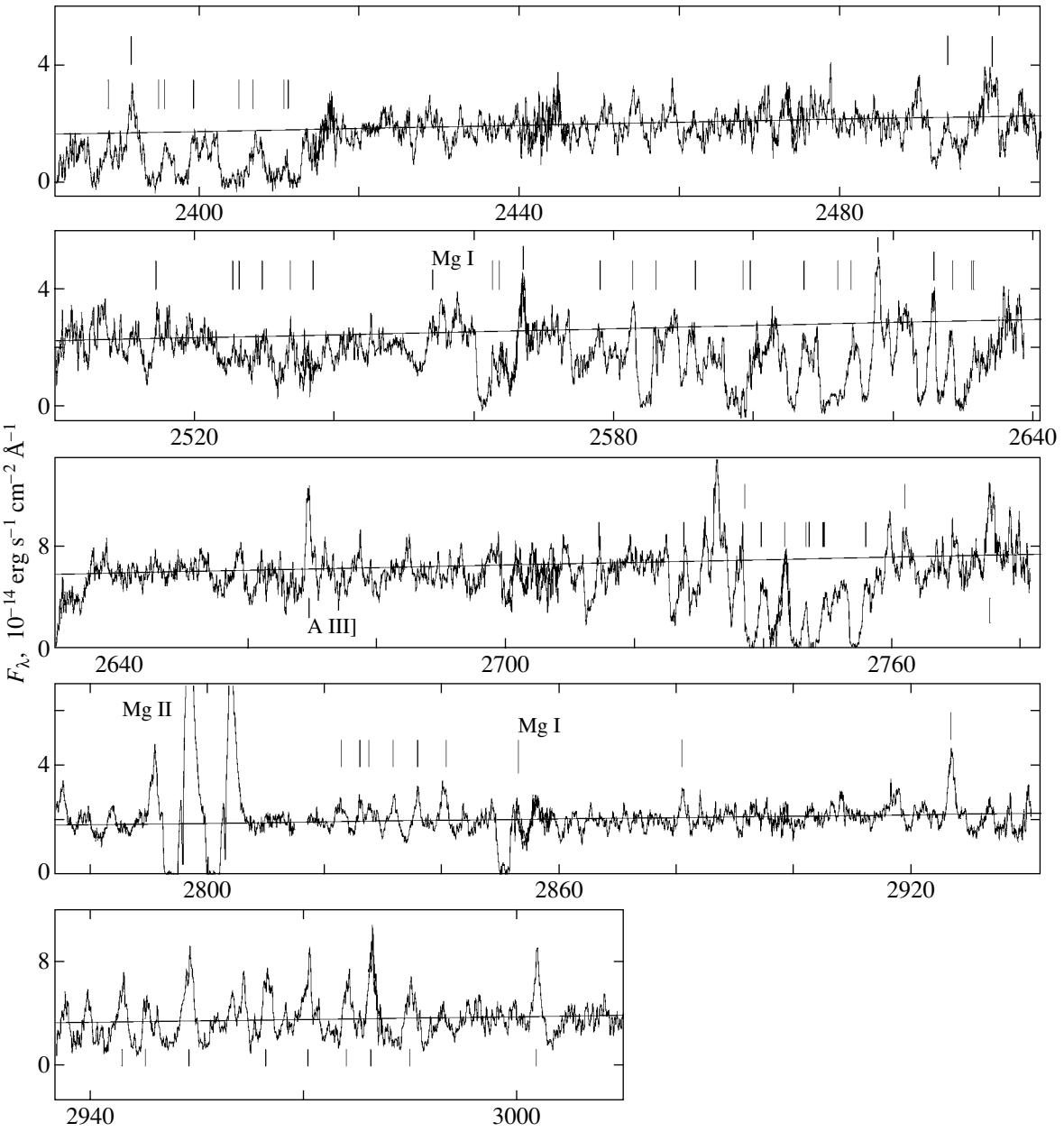

Fig. 1. (Contd.)

lines and the Mg I 2852.13 resonance line are similar to the Fe II line profiles: we see from the figure that, as in the iron lines, the blue and red absorption features extend to $\simeq$50–400 and $\sim$300 km s^{-1}, respectively. There is a symmetric feature attributable to interstellar extinction in the magnesium line at zero velocity. Note that the Fe II 2783.69 Å resonance line also shows a similar feature.

In the wavelength range 1290–1480 Å the spectrum of DR Tau exhibits several O I and S I lines (see Fig. 1). However, these lines are either blended with one another or too weak. Therefore, we can say nothing certain about their profiles.

In conclusion, let us consider the profile of the H I Lα 1215.67 line. In contrast to other lines, its profile is shown in Fig. 2 without any correction for the radial velocity of DR Tau (+23 km s^{-1}) and without normalization to the continuum level, i.e., in absolute units (10^{-14} erg s^{-1} cm^{-2} Å^{-1}). Since the line in these coordinates appears shifted to positive velocities, we may assert that the star rather than the geocorona mainly contributes to the line. To be more precise, we see only the part of the radiation from DR Tau that

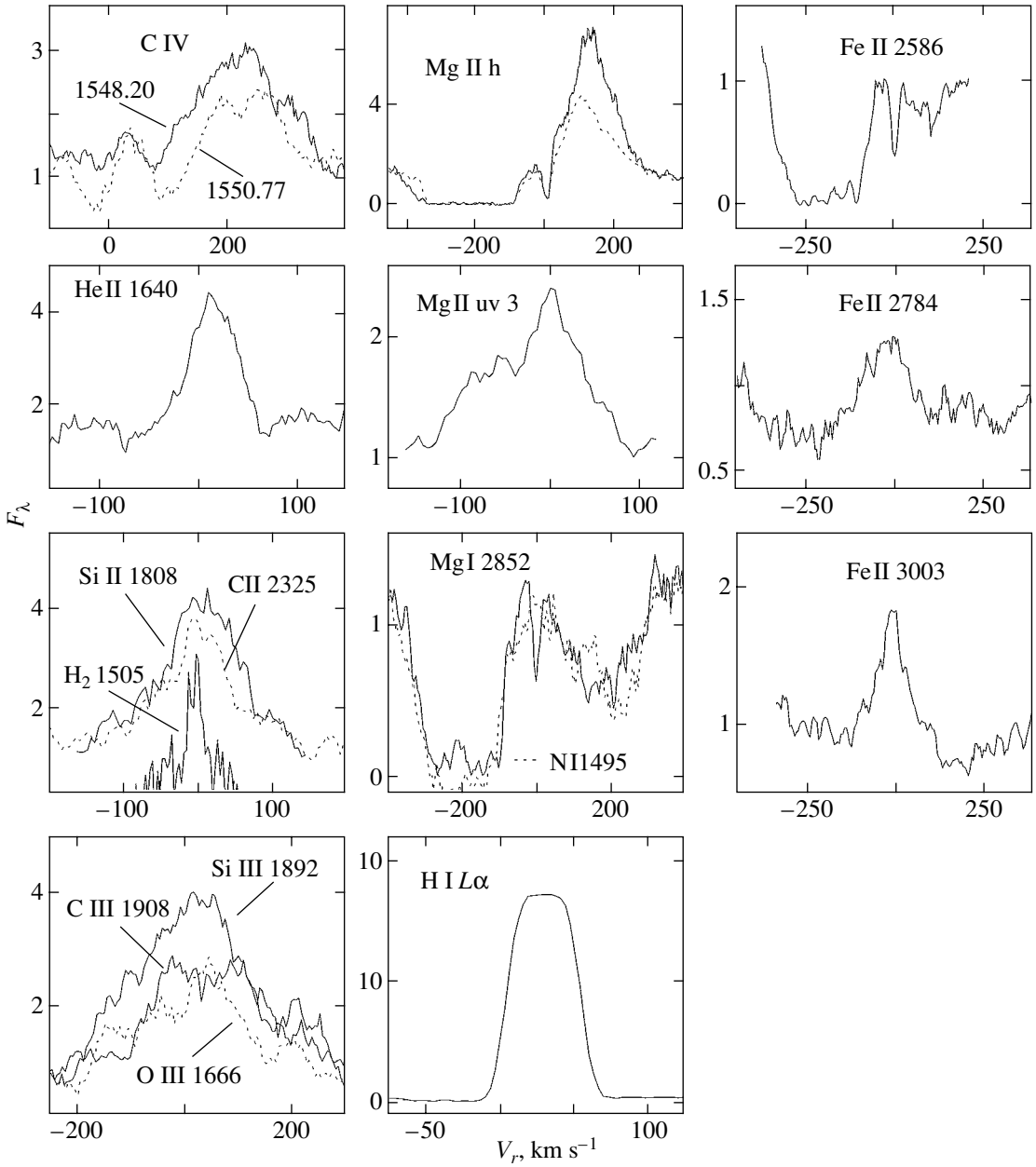

Fig. 2. Line profiles in the spectrum of DR Tau observed on August 29, 2000. The spectral flux density normalized to the continuum level (see the text) is along the y axis.

left after the absorption of Lα photons by interstellar neutral hydrogen (Kurt and Lamzin 1995).

ANALYSIS OF OBSERVATIONAL DATA

The Continuum Energy Distribution for DR Tau and Estimation of Its Integrated Parameters

We estimated the interstellar extinction A_V toward DR Tau by using the observed continuum energy distribution and by assuming that the λ dependence of extinction is described by the so-called normal extinction law (Seaton 1979). The continuum level was determined from the portions of the spectrum with reliably identified absorption and emission lines. We fitted the derived set of $F_\lambda(\lambda)$ values by a cubic spline and took the resulting curve as the continuum level of the star (Fig. 1). This curve is also shown in the upper panel of Fig. 3a together with *rms deviations* for each measured portion of the spectrum (the error of the mean is smaller by approximately an order of magnitude). It would be natural to assume that the nonmonotonic behavior of $F_\lambda(\lambda)$ results from the presence of a sharp peak in the interstellar extinction curve $A_\lambda(\lambda)$ (Bless and Savage 1972). Figure 3b

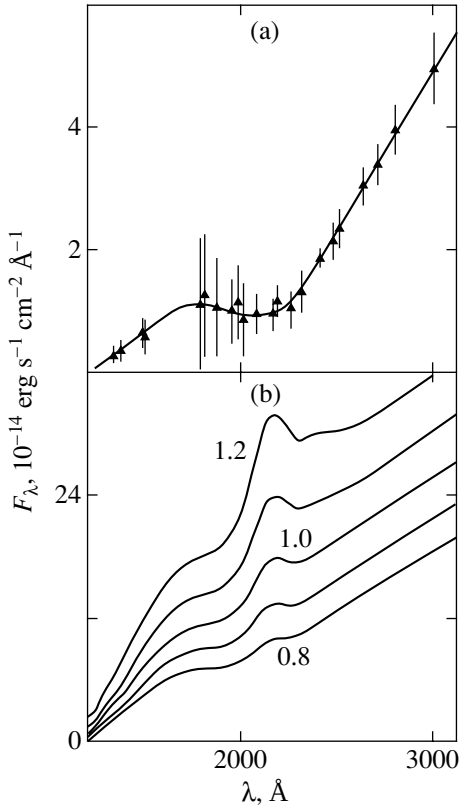

Fig. 3. The continuum energy distribution for DR Tau: (a) a spline fit to the observed energy distribution (the vertical bars indicate the error σ with which the continuum level is determined at a given point); (b) the energy distribution corrected for interstellar extinction with A_V from $0^m.8$ to $1^m.2$ at $0^m.1$ intervals.

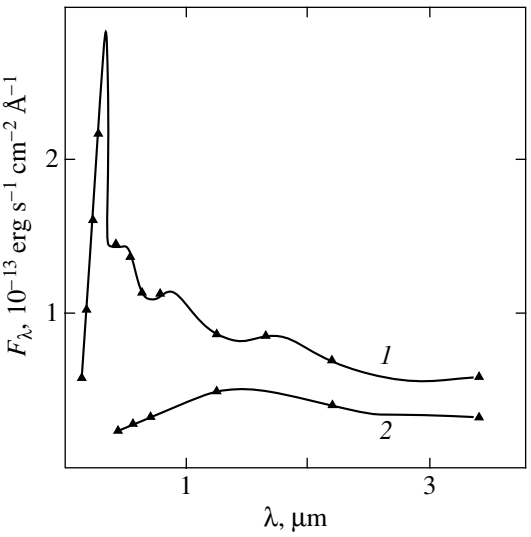

Fig. 4. The extinction-corrected continuum energy distribution for DR Tau on August 29, 2000, (*1*) and at minimum light (*2*) (see the text).

shows how the initial curve appears if it is corrected for interstellar extinction with various A_V. The local minimum near 2200 Å disappears for $A_V > 0^m.8$ and a hump emerges in its place for A_V larger than $1^m.0$. Therefore, we assume that $A_V = 0^m.9 \pm 0^m.1$ for DR Tau .

Using the inferred A_V, let us look at the continuum energy distribution for the star. It follows from Fig. 3 that the observed $F_\lambda(3000\ \text{Å}) \simeq 5 \times 10^{-14}$ erg s^{-1} cm^{-2} Å^{-1} in the August 29, 2000 spectrum. Approximately the same spectral flux density is obtained if we extrapolate the spectral energy distribution of the star shown in Fig. 1 from Valenti *et al.* (1993) to $\lambda = 3000$ Å. In this spectrum, $F_\lambda(5500\ \text{Å}) \simeq 6 \times 10^{-14}$ erg s^{-1} cm^{-2} Å^{-1}, which corresponds to $V = 12^m.0$. Therefore, we assume that the STIS spectra of DR Tau under study were taken when its magnitude was $V \simeq 12^m.0$, which is about $0^m.2$ fainter than the mean magnitude over the last 20 years [see the database in Herbst *et al.* (1994)].

We constructed the continuum energy distribution for DR Tau on August 29, 2000, by taking the B, R_c, I_c, J, H, K, and L magnitudes corresponding to its magnitude $V = 12^m.02$ (JD 2447437.8) from Kenyon *et al.* (1994) and by correcting them for interstellar extinction with $A_V = 0^m.9$ (Fig. 4). The total flux in the range 0.12–3.4 μm was found to be $\simeq 2.8 \times 10^{-9}$ erg s^{-1} cm^{-2}, which corresponds to a luminosity of $1.7L_\odot$. There are no measurements at $\lambda > 3.4$ μm in Kenyon *et al.* (1994). However, judging by the mean magnitudes (Kenyon and Hartmann 1995), in the range 3.4–10 μm, the star emits approximately a factor of 2 to 3 less than at $\lambda < 3.4$ μm. Adding the 12–100-μm flux (9.5×10^{-10} erg s^{-1} cm^{-2}) taken from the IRAS catalog (Weaver and Jones 1992), we find that the bolometric luminosity of DR Tau on August 29, 2000, was $\approx 3L_\odot$, i.e., a factor of 1.5 to 2 higher than our value inferred from Fig. 4.

Figure 4 also shows F_λ derived from the B, V, and R_J magnitudes observed on JD 2450713.47 (Mel'nikov *et al.* 2002). At that time, the star had the lowest known V brightness: $13^m.69$. Since we failed to find infrared brightness measurements at such a faint V magnitude in the literature, we determined the J, K, and L magnitudes for this state by extrapolating the (linear) dependences $J(V)$, $K(V)$, and $L(V)$ from Kenyon *et al.* (1994). This allowed us to determine the luminosity in the range 0.44–3.4 μm, $\simeq 0.7L_\odot$. To estimate the upper limit on the bolometric luminosity of the star, we doubled this value by analogy with the August 29, 2000 spectrum. Note that the B brightness for the state under consideration ($14^m.73$) is not the minimum possible one for DR Tau: judging from photographic observations, the star in the B band can be fainter by a factor of 1.5 to 2 (Chavarria-K 1979; Kurochkin 1980). That is why we consider

$1.4L_\odot$ to be an upper limit on the luminosity of the central star L_*, which yields the following constraint on the radius for the spectral types K5–M0: $R_* < 2$–$2.6\ R_\odot$, respectively (Cohen and Kuhi 1979).

It would be reasonable to assume that the age of such an active young star as DR Tau does not exceed 3×10^6 yr. According to Baraffe *et al.* (1998), the following constraints hold for K5–M0 stars younger than 3 Myr: $0.75 < M/M_\odot < 1.1$, $R/R_\odot > 1.4$, and $q \equiv (M_*/M_\odot)/(R_*/R_\odot) \leq 0.65$. The fact that the gas infall velocity is no less than 300 km s^{-1} allows a lower limit to be placed on q: $q > 0.25$. Given the above constraints, we believe that $M_* = 0.9M_\odot$, $R_* = 1.8\ R_\odot$, and $L_* = 0.9\ L_\odot$ are reasonable estimates of the parameters for DR Tau and are similar to those made by Basri and Bertout (1989). For such M_* and R_*, the escape velocity is $V_\infty = 480$ km s^{-1}.

The Pattern of Accretion

Since the red wings of the C IV 1548.20 and 1550.77 emission lines extend up to a velocity $\simeq$300–350 km s^{-1}, the preshock gas infall velocity V_0 is not less than this value. The red absorption features of the Fe II, Mg I, and N I lines also extend up to 250–300 km s^{-1}, as do those of several optical lines (Appenzeller *et al.* 1988; Beristain *et al.* 1998), including the He I 5875.6 line (Guenther and Hessman 1993). If the gas falls to the star from distance R_f, then we find from the relation $GM_*/R_* - GM_*/R_f = V_0^2/2$ that $R_f/R_* = 1.6$ at $V_0 = 300$ km s^{-1} and $R_f/R_* = 2.1$ at $V_0 = 350$ km s^{-1}. Thus, the gas falls to the star from a height $\sim R_*$.

The profile of the He II 1640.42 line is almost identical to the profile of the He II 4686 line (Lamzin 1991). The difference between the profiles of the He^+ lines and the C IV 1550 doublet lines probably stems from the fact that the helium lines are mostly formed behind the shock front. As for the Si IV 1400 doublet lines, their low intensity in the spectrum of DR Tau can be easily explained: It follows from the calculations by Lamzin (1998) that the flux ratio $F_{\mathrm{Si\,IV}}/F_{\mathrm{C\,IV}} \simeq 0.2$ at $V_0 = 300$ km s^{-1} and interstellar extinction with $A_V = 0^m\!.9$ further decreases this value by a factor of 2.

Let us estimate the accretion rate onto the star and the accretion luminosity attributable to an accretion shock. Let $\mathfrak{F}_{\mathrm{CIV}}$(erg s^{-1} cm^{-2}) be the power emitted in the C IV 1550 doublet lines from a unit surface area by a one-dimensional accretion shock and S_{ac} be the area occupied by the shock on the stellar surface. It follows from our calculations that the ratio δ_{CIV} of the flux $\mathfrak{F}_{\mathrm{CIV}}$ to $\mathfrak{F}/2 \equiv \rho_0 V_0^3/4$ monotonically increases from 5 to 7% as V_0 increases from 250 to 400 km s^{-1}; in the range of densities $-12.7 < \log \rho_0 < -11.3$ typical of accretion onto young stars, δ_{CIV} is virtually independent of ρ_0 (Lamzin 1998).

The luminosity in the doublet lines $\mathrm{L_{CIV}}$, the accretion rate $\dot{M}_{\mathrm{ac}}^{\mathrm{sh}}$, and the accretion luminosity attributable to the accretion shock $\mathrm{L_{ac}^{sh}}$ are related by

$$L_{\mathrm{CIV}} = \mathfrak{F}_{\mathrm{CIV}} S_{\mathrm{ac}} = \delta_{\mathrm{CIV}} \frac{\rho_0 V_0^3}{2} S_{\mathrm{ac}} \qquad (1)$$
$$= \dot{M}_{\mathrm{ac}}^{\mathrm{sh}} \frac{V_0^2}{4} \delta_{\mathrm{CIV}} = \frac{L_{\mathrm{ac}}^{\mathrm{sh}} \delta_{\mathrm{CIV}}}{2}.$$

The total observed flux in the C IV 1550 doublet lines on August 29, 2000, was 1.3×10^{-14} erg s^{-1} cm^{-2}, which, given interstellar extinction, corresponds to a luminosity 2.6×10^{29} erg s^{-1}. We then find from relation (1) that at the time of observations, $\dot{M}_{\mathrm{ac}}^{\mathrm{sh}} \simeq 3 \times 10^{-10}\ M_\odot$ yr^{-1} and $L_{\mathrm{ac}}^{\mathrm{sh}} \simeq 0.002\ L_\odot$. At such an accretion rate and $R_* = 1.8\ R_\odot$, the accretion shock occupies $f \sim 2(\rho_0/2 \times 10^{-13})\%$ of the stellar surface area.

We found above that at the time of observations, the contribution of the central star to the total luminosity of DR Tau was $0.9/3.0 \simeq 30\%$. No less than half of the observed luminosity falls within the range with $\lambda > 1\ \mu$m, which is more than an order of magnitude higher than the photospheric luminosity of M0–K5 stars. The infrared excess cannot be attributed to the cool companion of the star, because the infrared and optical brightness variations are synchronous (Kenyon *et al.* 1994). This implies that the radiation in all spectral bands is correlated and that its primary source, according to current views, is disk accretion, which generates a luminosity $L_{\mathrm{ac}} = L_{\mathrm{bol}} - L_* \simeq 2.1L_\odot$. Meanwhile, according to our estimate, $L_{\mathrm{ac}}^{\mathrm{sh}}$ is, at the same time, three orders of magnitude lower than this value. Let us consider the probable causes of such a large discrepancy.

We may assume that the calculations by Lamzin (1998) are erroneous and $\delta_{\mathrm{C\,IV}}$, which characterizes the relative contribution of the emission in the C IV 1550 doublet lines to the accretion-shock bolometric luminosity, was overestimated by three orders of magnitude. We completely rule out such a large error, if only because test calculations showed good agreement with the corresponding results of other authors. There are alternative calculations of the accretion-shock structure performed by Calvet and Gullbring (1998) made under assumptions that simplify the problem. Based on these calculations, Gullbring *et al.* (2000) reproduced the observed energy distribution in the optical and UV veiling continuum spectra of DR Tau with a reasonable accuracy for the following parameters: $L_{\mathrm{ac}}^{\mathrm{sh}} \simeq 1\ L_\odot$, $\dot{M}_{\mathrm{ac}}^{\mathrm{sh}} \simeq$

310^{-7} $M_\odot$ yr^{-1}, $V_0 \simeq 280$ km s^{-1}, and $\log \mathfrak{F} = 11.5$, $f \simeq 5\%$.

Calvet and Gullbring (1998) provide no information on $\delta_{\rm C\,IV}$, but its lower limit can be estimated. To simplify calculations, it was assumed in this paper that the ion abundance at each point behind the shock front corresponds to the so-called coronal equilibrium at a local temperature. This means that the C IV 1550 doublet lines behind the accretion-shock front originate in a layer where the temperature changes approximately from 8×10^4 to 1.5×10^5 K; in this narrow temperature range ($\Delta T \simeq 7 \times 10^4$ K), the C IV 1550 lines mainly contribute to the cooling function Λ (Raymond and Smith 1977), whence Calvet and Gullbring took the dependence $\Lambda = \Lambda(\rho, T)$. It is easy to show that at $V_0 = 280$ km s^{-1}, the gas in the region under consideration cools down virtually at constant pressure (Zel'dovich and Raizer 1966; Lamzin 1998). Therefore, the expression for the conservation of energy (15) from Calvet and Gullbring (1998) can be rewritten as

$$\frac{\mathrm{d}}{\mathrm{d}z}\left(\rho V \frac{5\mathfrak{R}T}{2\mu}\right) = j\frac{\mathrm{d}}{\mathrm{d}z}\left(\frac{5\mathfrak{R}T}{2\mu}\right) = -\Lambda(\rho, T),$$

where ρ and V are, respectively, the gas density and velocity at the point with coordinate z counted off from the one-dimensional shock front along a streamline and $\mathfrak{R} \simeq 8.3 \times 10^7$ erg g^{-1} K^{-1} and $\mu \simeq 1.3$ are the universal gas constant and the gas molecular weight, respectively. Here, we took into account the fact that $j \equiv \rho V = \rho_0 V_0 = \mathrm{const}$ in a one-dimensional flow. Integrating this relation over the C IV 1550 line formation region yields

$$j\frac{5\mathfrak{R}\Delta T}{2\mu} = \int \Lambda \mathrm{d}z \simeq 2\mathfrak{F}_{\rm C\,IV},$$

if the carbon contribution to the cooling function is assumed to be 50%. Since $\mathfrak{F} = jV_0^2/2$,

$$\delta_{\rm C\,IV} = \frac{\mathfrak{F}_{\rm C\,IV}}{\mathfrak{F}} \simeq \frac{5\mathfrak{R}\Delta T}{2\mu V_0^2} \simeq 0.01.$$

The C^{+3} lines are formed not only behind but also ahead of the accretion-shock front, in a region ionized by short-wavelength radiation from under the front. Consequently, $\delta_{\rm C\,IV}$ in the model by Calvet and Gullbring is approximately the same as that in the model by Lamzin (1998). Therefore, in reproducing the observed continuum energy distribution, Gullbring *et al.* (2000) obtained a flux in the C IV 1550 lines that was three orders of magnitude higher than the observed flux without being aware of it. Hence, the following conclusion can be drawn: the abnormally low observed value of $\delta_{\rm C\,IV}$ cannot be explained as an error in the calculations.

In principle, the low intensity of the carbon and silicon lines in the accretion shock can be attributed to abnormally low abundances of these elements in the accreted gas. However, one can hardly imagine a mechanism that leads to a reduction in the C and Si abundances by a factor of 1000 in the accreted matter. Therefore, we believe that the problem cannot be completely solved in this way.

For RW Aur, Errico *et al.* (2000) showed that the Fe II absorption lines originating in the stellar wind could superimpose on the C IV 1550 doublet lines and could severely distort their profile. The same effect most likely also takes place for DR Tau. We failed to estimate this quantitatively because of the low S/N ratio in the analyzed spectrograms. However, by comparing the profile shape and relative intensity of the C IV 1550 doublet components, we concluded that blending could not reduce the initial intensity of the carbon lines by more than several times.

Another alternative explanation for the low intensity of the UV lines originating in the accretion shock, in particular, the C IV 1550 lines, is the assumption that there is matter along the line of sight whose optical depth τ at $\lambda = 1550$ Å is of the order of $\ln(10^3) \simeq 7$. Given the large infrared excess in DR Tau, the UV radiation may be assumed to be absorbed by a dust envelope. Let us consider this hypothesis quantitatively. We choose a sufficiently narrow spectral range, say, 30 Å, near $\lambda = 1550$ Å, within which the dust absorption coefficient may be assumed to be virtually constant. The spectral flux density corrected for interstellar extinction changes only slightly within this range and $\simeq 6 \times 10^{-14}$ erg s^{-1} cm^{-2} Å^{-1}, which corresponds to a luminosity of $0.008 L_\odot$ in the range 1535–1565 Å. Increasing this value by a factor of 1000, we obtain $8L_\odot$, i.e., a value that exceeds $L_{\rm ac}$. Thus, we cannot completely explain the low $L_{\rm ac}^{\rm sh}/L_{\rm bol}$ ratio in terms of dust absorption of the UV radiation from the accretion shock.

Finally, let us explore the possibility that the disk rather than the accretion shock is the main source of the DR Tau luminosity. In this case, the accretion luminosity is $GM_*\dot{M}_{\rm ac}/R_*$; half of this energy must be released in the disk proper, and the other half must be released in the boundary layer near the stellar surface (Shakura and Syunyaev 1973; Lynden-Bell and Pringle 1974). Basri and Bertout (1989) showed that the continuum energy distribution for DR Tau at $\lambda < 1$ μm could be reproduced in this model for the following parameters: $M_* = 0.85$ $M_\odot$, $R_* = 1.6$ $R_\odot$, $L_{\rm ac} \simeq 1.8$ $L_\odot$, and $\dot{M}_{\rm ac} \simeq 9 \times 10^{-8}$ $M_\odot$ yr^{-1}. Since we obtained virtually the same M_*, R_*, and $L_{\rm ac}$, our accretion rate through the boundary layer at the time in question must also be $\simeq 10^{-7}$ $M_\odot$ yr^{-1}.

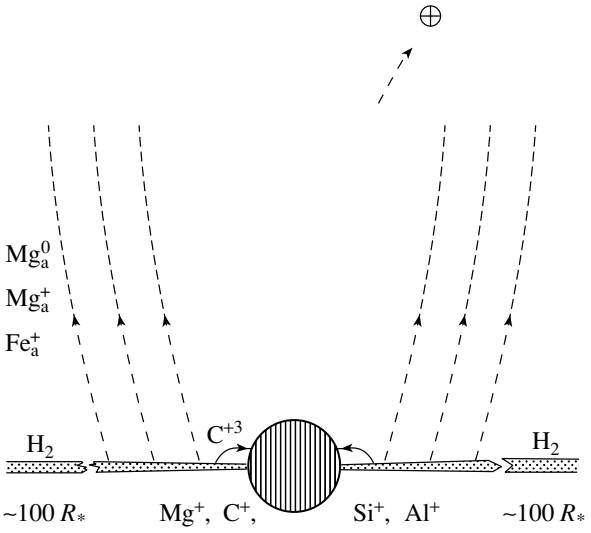

Fig. 5. A schematic view of kinematically distinct regions in the vicinity of DR Tau. The region bounded by the heavy line is the accretion disk; the Mg, C, Si, and Al emission lines originate in inner disk regions, while the H_2 lines originate in outer disk regions at a distance of $\sim 100 R_*$. Part of the matter falls to the star along magnetic field lines (thin lines), producing an accretion shock in which, in particular, the C IV lines are formed. The dashed lines represent streamlines of the disk wind in which the Mg I, Mg II, and Fe II lines arise. The arrow in the upper part of the figure indicates the direction to the observer.

Thus, if the high-temperature lines originate in the accretion shock and if the veiling continuum originates mainly in the disk and the boundary layer, then only $3 \times 10^{-10}/10^{-7} \simeq 0.3\%$ of the accreted matter passes through the accretion shock.

The derived ratio appears unexpectedly low. However, we believe that it cannot be increased by more than a factor of 10 to 30 even if all of the above factors are taken into account. We have to recognize that mass accretion onto DR Tau proceeds mainly through the disk and the boundary layer, with $\dot{M}_{\rm ac}^{\rm sh}/\dot{M}_{\rm ac}$ being definitely $<10\%$. In that case, the presence of absorption features in the red wings of the N I, Fe II, and He I lines implies that part of the preshock zone is projected onto the accretion disk. A possible suitable geometry is shown in Fig. 5.

According to Appenzeller *et al.* (1980), the flux in the carbon doublet lines in 1979 was approximately a factor of 9 higher than that in our case. However, the star was also brighter at that time by approximately $0\overset{m}{.}6$ in V, so the accretion-shock contribution to the accretion luminosity in 1979 was also fairly small.

Mass Outflow from DR Tau

Our data are consistent with the current views that mass outflow in young stars proceeds from the surface of an accretion disk. The wind velocity component along the line of sight reaches 400 km s^{-1}; since this value is close to the parabolic velocity of the star, the wind velocity itself is probably $V_w \simeq 400$ km s^{-1}. This means that some of the streamlines are oriented almost along the line of sight. Consequently, the streamlines are inclined to the disk plane at an angle close to $\pi/2 - i$, where i is the angle between the disk rotation axis and the line of sight. The small rotational broadening of photospheric lines, $v_* \sin i \leq 10$ km s^{-1} (Hartmann and Stauffer 1989), is commonly assumed to indicate that the angle i is small. However, it in no way follows that DR Tau does not rotate about its axis very slowly.

An upper limit on i can be obtained from the following considerations. The extent of the blue wing of the [O I] 6300 Å line, which most likely originates in a jet moving perpendicular to the disk plane, does not exceed $V_j^r \simeq 200$ km s^{-1} (Hirth *et al.* 1997). In that case, $i \leq \arccos(V_j^r/V_w) = 60°$; the sign of the inequality allows for the possibility of shock formation at the jet base. Since the matter in the part of the wind where the Fe II lines are formed moves almost along the line of sight, it thus follows that the streamlines in this region make an angle larger than 30° with the disk plane.

If the veiling continuum of DR Tau originates in the accretion disk, then the presence of absorption in the blue line wings suggests that the corresponding wind region is projected onto the continuum formation region. At the same time, the wind is also projected onto the accretion shock. Indeed, we see from Fig. 1 that one of the C II uv1 doublet lines ($\lambda = 1335.68$ Å) exhibits a redshifted emission feature. However, there is no emission feature in the second line of this doublet ($\lambda = 1334.53$ Å), probably because it is blended with the blue absorption wing of the first line. The O III] 1663 doublet lines illustrate another example: the $\lambda = 1666.15$ Å line is seen in emission, while the second ($\lambda = 1660.81$ Å) line, which shares the upper level with the first line, is absent. This is probably because the blue absorption wing of the Fe II 1663.22 is superimposed on it. To avoid misunderstandings, we note the following: we have no doubt that at least the red wings of the O III] lines are formed in the accretion shock (see below).

As was pointed out above, many Fe II lines originating in the wind are observed at wavelengths shorter than $\simeq 2900$ Å. However, in the optical lines of this ion, no absorption is observed in their blue wings. This can be explained by assuming that the population of the levels with excitation potentials $E_i > 1.5$ eV for Fe II in the wind is low and by taking into account the fact that all levels with $E_i < 4.7$ eV for

Fe^+ have the same parity. The latter implies that the probabilities of transitions between levels with $E_i < 4.7$ eV are low. Therefore, strong absorption lines can emerge only for transitions with $\Delta E > 4.7 - 1.5 = 3.2$ eV, i.e., for lines with $\lambda < 4000$ Å. A more detailed analysis indicates that there is an even more stringent constraint: $\lambda < 2900$ Å. Note that the Fe II lines sharing the lower levels with the uv 234 multiplet lines do not fall within the optical range either. Judging by the significant intensity of the uv 234 multiplet lines, the levels of the $b^2H_{9/2,11/2}$ term ($E_i \simeq 3.2$ eV) have an abnormally large population in the wind matter, whose cause is unclear.

The low population of the Fe II levels with $E_i > 1.5$ eV suggests that although the gas temperature in the wind region where they are formed exceeds 5000 K, it is probably $< 10^4$ K (Errico *et al.* 2000). The absence of Fe I atoms in the wind in the presence of Mg I atoms with almost the same ionization potential (7.9 and 7.6 eV, respectively) becomes clear if the iron ionization is attributable not to electron collisions but to photoionization by H I L_α photons, which are produced in large quantities in the region of main energy release (Kurt and Lamzin 1995). The point is that the photoionization cross section for Fe I at $\lambda \simeq 1216$ Å is a factor of 6 larger than that for Mg I (Verner *et al.* 1996). However, if this is the case, then the stellar-wind region responsible for the formation of blue absorption features is fairly close to the star, probably, at a distance of only several radii from it. This suggestion is also supported by a high wind velocity comparable to V_∞ : in all of the known astrophysical situations, the limiting wind velocity is less than twice the escape velocity. Eventually, the outflowing gas will cool down and iron atoms will emerge in it. In this case, however, the gas will probably fly away far from the star and will no longer be projected onto the emission continuum formation region.

Ardila *et al.* (2002) argue that a feature blueshifted by 250 km s^{-1} is observed in one of the GHRS spectrograms for DR Tau in the C IV 1548.20 line. The authors believe that they managed to observe an occasional outflow of hot ($T \simeq 10^5$ K) matter from the magnetosphere produced by magnetic line reconnection. Meanwhile, this feature emerges after the calculated value obtained from the observed flux in the H_2 P(5) 1562.39 line by assuming that both lines sharing the upper level ($v' = 1$, $J' = 4$) are optically thin was subtracted from the observed flux in the R(3) 1547.33 molecular hydrogen line. However, we will see in the next section that although the H_2 lines are actually optically thin, the observed flux in the P(5) 1562.39 line is half the expected flux. Therefore, we assume that the emission feature in the blue wing of the C IV 1548.20 line is entirely attributable to the H_2 emission and Ardila *et al.* (2002) have no reason to believe that they detected gas outflow with a temperature $\simeq 10^5$ K.

On the other hand, the extent of the blue wings in the optically thin O^{+2}, C^{+2}, and Si^{+2} intercombination lines is ≥ 150 km s^{-1}. These lines can originate both in the hottest disk-wind region ($T \leq 3 \times 10^4$ K) and in the gas that rises from the disk along magnetic field lines to subsequently fall to the star (Errico *et al.* 2001).

The Accretion Disk

Let us now consider almost symmetric emission lines whose peaks have the same radial velocity as the photospheric lines. This group includes the intercombination lines of C II, Si II, and Al II the emission features of Fe II lines and the molecular hydrogen lines. As was pointed out above, the FWHM of these lines ranges from $\simeq 100$ km s^{-1} for the ions to $\simeq 20$ km s^{-1} for the H_2 lines. In other words, the lower the temperature in the line formation region, the smaller the FWHM. This dependence could be expected if the group of lines under consideration originates in an accretion disk.

This hypothesis is consistent with the fact that the symmetric-line formation region is screened by the wind (see Fig. 5). Consider, for example, the Si II] 2340 quintet lines with spontaneous transition probabilities $\leq 3 \times 10^3$ s^{-1} [see the CHIANTI database from Dere *et al.* (1997)]. Therefore, there is no doubt that the quintet lines are optically thin and the absence of the 2344.20 line in the star's spectrum in the presence of strong 2334.41 and 2334.6 lines can be explained only by the fact that the 2344.20-line emission is blended with the absorption wings of several nearby Fe II lines originating in the stellar wind. The abnormally low intensity of the 2328.13 line, one of the C II] 2335 quintet lines, can be probably explained in a similar way.

Let us estimate the physical conditions in the inner disk regions, i.e., where the lines of ions with charge +1 are formed. We assume that the Al II] 2669.15 and Si II 1808.01 lines originate in the same zone; all of the aluminum and silicon are singly ionized and the elements have standard abundances. Taking the corresponding atomic data from Dere *et al.* (1997), we calculated the Si^+ and Al^+ level populations by ignoring photoexcitations and emission thermalization. Note, incidentally, that the transition probabilities for the lines under consideration are low: $\sim 3 \times 10^3$ and 3×10^6 s^{-1}, respectively. The intensity ratio of the Al II] 2669.15 and Si II 1808.01 lines in the spectrum of DR Tau corrected for interstellar extinction is $\simeq 0.6$.

Our calculations indicate that such a ratio is possible if the gas temperature T exceeds 10^4 K. For our subsequent estimates, we take $T = 1.5 \times 10^4$ K and assume that the hydrogen is ionized almost completely. We found the electron density from the intensity ratio of the Si II 1808.01 and 2334.60 lines ($F_{2334}/F_{1808} \simeq 0.6$) to be $N_e \simeq 10^{10}$ cm^{-3}. This value agrees with the observed intensities of the C II] 2335 lines, for which the critical density is $N_e^{cr} \simeq 3 \times 10^9$ cm^{-3}.

For the derived T and N_e, we calculated the volume emission measure of the emitting region first from the Al II] 2669.15 line ($F_{2669} \simeq 2.2 \times 10^{-14}$ erg s^{-1} cm^{-2}) and then from the Si II 1812 triplet lines ($F_{1812} \simeq 5.3 \times 10^{-14}$ erg s^{-1} cm^{-2}). In both cases, we obtained almost the same value: $VN_e^2 \simeq 210^{54}$ cm^{-3}, where V is the volume of the region under study.

Let R_e be the characteristic radius of the disk region in which the lines of the ions in question are formed. We assume that the temperature in the disk atmosphere changes only slightly along the z axis perpendicular to the disk plane. In that case, the density in the atmosphere varies as (Shakura and Sunyaev 1973) $N(z) = N_0 \exp\left[-(z/H_p)^2\right]$, where the scale height is

$$H_p(R_e) = \sqrt{\frac{2\Re T R_e^3}{GM_*\mu}} = 5.610^9 \left(\frac{R_e}{R_*}\right)^{3/2} \text{ cm}. \quad (2)$$

Thus, the characteristic disk thickness in the line formation region is $\sim 0.1R_*$; i.e., the disk is thin. Assuming that $V \simeq \pi R_e^2 H_p$, we find that the lines of the ions in question are formed within a region of radius $R_e \simeq 3.5R_*$.

If the disk were Keplerian at $R \leq R_e$, then the orbital gas velocity near the star would be ~ 300 km s^{-1}. To obtain the observed full width of the profile at zero intensity, $V_{max} \simeq 100$ km s^{-1}, we must assume that the disk is inclined to the line of sight at an angle $i \simeq 20^\circ$. It can be shown that the line profile would then have a double-peaked structure with the separation between the peaks $\Delta V \simeq 2V_{max}/\sqrt{(R_e/R_*)}$, i.e., slightly more than 100 km s^{-1}, which is not however observed. Therefore, if the ion lines actually originate in the inner disk, then the gas motion in this region must differ greatly in pattern from Keplerian motion. A line formed in an axisymmetric disk must have a double-peaked profile for any disk rotation law. However, it is easy to show that if the orbital velocity in the disk is $\propto R^n$, then the separation between the profile peaks at $n > 3/2$ and $R_e = 3.5R_*$ will be <20 km s^{-1}, and, given the low S/N ratio in the analyzed spectra, it is unlikely that the double-peaked structure will be detectable. Note that the disk rotation in the inner regions must differ greatly in pattern from Keplerian rotation, because the disk interacts with the stellar magnetic field [see Romanova *et al.* (2002) and references therein].

Since, to all appearances, the C^+, Si^+, and Al^+ lines are optically thin, their profiles are shaped by large-scale gas motion in the formation region. The situation with the emission features of the Fe II lines, which, in our view, also originate in the disk, is not so clear. We see from Fig. 1 that the width of these lines is proportional to their intensity, as in optical iron lines (Beristain *et al.* 1998). Without a detailed analysis, which is beyond the scope of this paper, we cannot say whether this effect is entirely attributable to broadening through an increase in the optical depth if we have evidence of a significant radial extent of the Fe II line formation region in the disk.

As for the UV Fe I lines, their analysis shows the following. The Fe I lines formed via transitions from several excited levels are observed at optical wavelengths (Beristain *et al.* 1998). For strong optical lines (with equivalent widths >0.3 Å), transitions from the same upper levels produce overly weak lines at $\lambda < 3100$ Å which are undetectable at the available S/N ratio. The corresponding counterparts of weaker optical lines are either also weak or are blended with Fe II lines. This explains why we could not reliably identify any Fe I line in the UV spectrum of DR Tau.

We agree with Ardila *et al.* (2002a) that the molecular hydrogen lines are formed in the disk atmosphere through fluorescent pumping by H I Lα photons of gas with a temperature of no less than 1000 K. The molecules are pumped only by photons from the red wing of the Lα line, whose observed profile has no blue wing. This, probably, implies that the blue wing of the Lα line is absorbed by the wind matter.

Since the H_2 line formation region must be fairly far from the star, the gas motion in it is most likely Keplerian. Given that $\text{FWHM}_{H2} \simeq 20$ km s^{-1}, this allows the region size to be estimated: $R_{H2} \simeq 225R_*\sin^2 i$; since $i \leq 60^\circ$, $R_{H2} \leq 1.4$ AU. Unfortunately, the spectra under study are too noisy to judge with confidence whether the profiles of the H_2 lines have a double-peaked structure for the available spectral resolution.

We found that after the correction for interstellar extinction, the intensity ratios of the H_2 lines sharing the upper level correspond to the optically thin case. In particular, this is also true for the R(3) 1431.01, P(5) 1446.12, R(3) 1489.57, P(5) 1504.76, and R(3) 1547.34 lines—the $v' = 1$, $J' = 4$ upper level of the $2p\sigma B^1\Sigma_u^+$ electron configuration. As was pointed out

above, only the P(5) $\lambda = 1562.39$ Å line whose intensity is half the expected value constitutes an exception. Since it is located near the strong Fe II 1563.79 line, it would be natural to assume that its abnormally low intensity is the result of absorption by the wind matter.

Thus, the system has such a geometry that the wind region where the Fe II lines are formed is projected onto the part of the disk far removed from the star. The size of the warm-wind region is most likely appreciably smaller than $R_{\rm H2}$. Therefore, the wind screens the far edge of the disk, which is possible only if the angle i is not too small.

Because of the low spectral resolution and the moderately high S/N ratio, we have to leave open the question of the centroid position of the H_2 lines, although Ardila *et al.* (2002a) are sure that the centroid is blueshifted by several kilometers per second. Incidentally, these authors took the radial velocity to be +27.6 km s^{-1}, i.e., 4.5 km s^{-1} higher than that obtained by Appenzeller *et al.* (1988) and Edwards (2002). Thus, it would be reasonable to assume that the question of whether a disk wind exists from the H_2 line formation region should be studied further.

CONCLUSIONS

Our analysis of the UV spectra for DR Tau has led us to conclude that mass accretion onto this star proceeds mainly through the disk and the boundary layer, with $\dot{M}_{\rm ac} \simeq 10^{-7}\,M_\odot$ yr^{-1} at the time of observations. Concurrently, a small ($<10\%$) fraction of the matter falls to the star along magnetospheric magnetic field lines from a height $\sim R_*$. The bulk of the accretion energy radiates away in continuum, producing a veiling continuum. The quantitative model for this phenomenon probably corresponds to the calculations by Basri and Bertout (1989). The lines of ions with charge +1 are formed within a $\simeq 3.5R_*$ region in the atmosphere of a $\sim 0.1R_*$-thick disk with a temperature of $\simeq 1.5 \times 10^4$ K. We believe that the bulk of the radiation in the atomic hydrogen lines is also produced here. The molecular hydrogen lines are also formed in the disk at a distance <1.4 AU from the star.

Accretion is accompanied by mass outflow from the accretion-disk surface. Since, in particular, the Mg II h and k lines have P Cyg profiles in all GHRS and STIS spectra of DR Tau, it should be recognized that mass outflow proceeds continuously rather than results from short-duration unsteady-state events [see Romanova *et al.* (2002) for a discussion on this subject]. The wind matter in a region of size $<10R_*$ has a temperature of $\sim$7000 K. In this case, however, almost all of the iron is singly ionized by HI Lα photons from inner disk regions. Where the warm-wind velocity reaches $\simeq$400 km s^{-1}, the gas moves at an angle of $\geq 30°$ to the disk plane. We found no reliable evidence of the existence in the wind of regions with temperatures above $>10^4$ K and leave open the question of whether there is mass outflow in the H_2 line formation region.

The system has such a geometry that part of the matter falling to the star ahead of the accretion shock front is projected onto the disk and the warm-wind region is projected onto both the accretion shock and the accretion disk; the regions up to the H_2 emission zone are screened by the wind. The latter suggests that the inclination of the disk axis to the line of sight cannot be too small, although the rotational broadening of the stellar photospheric lines is small. At the same time, we found that $i \leq 60°$.

The only thing that, in our view, may cast doubt on the validity of our model is that the profiles of the lines that presumably originate in the accretion disk show no double-peaked structure. We hope that this circumstance can be explained by non-Keplerian disk rotation in the line formation region for the ion lines and by the insufficient spectral resolution and low S/N ratio in the spectra under study for the H_2 lines. The determination of i from interferometric observations of the disk not only would allow us to ultimately solve this problem but also would make it possible to obtain quantitative information on the orientation of streamlines in the wind and the stellar magnetosphere.

ACKNOWLEDGMENTS

We wish to thank S.Yu. Melnikov and S. Edwards, who placed their unpublished observations at our disposal; I. Baraffe for quantitative information on the evolutionary tracks of young stars; V.M. Lipunov and V.P. Grinin for fruitful discussions; and the referees for helpful remarks. This study was supported by the Russian Foundation for Basic Research (project no. 02-02-16070).

REFERENCES

1. S. H. P. Alencar, C. M. Johns-Krull, and G. Basri, Astron. J. **122**, 3335 (2001).
2. I. Appenzeller, C. Chavarria, J. Krautter, *et al.*, Astron. Astrophys. **90**, 184 (1980).
3. I. Appenzeller, A. Reitermann, and O. Stahl, Astron. Astrophys. **100**, 815 (1988).
4. D. R. Ardila, G. Basri, F. M. Walter, *et al.*, Astrophys. J. **566**, 1100 (2002a).
5. D. R. Ardila, G. Basri, F. M. Walter, *et al.*, Astrophys. J. **567**, 1013 (2002b).
6. I. Baraffe, G. Chabrier, F. Allard, and P. H. Hauschildt, Astron. Astrophys. **337**, 403 (1998).

7. G. Basri and C. Bertout, Astrophys. J. **341**, 340 (1989).
8. G. Beristain, S. Edwards, and J. Kwan, Astrophys. J. **499**, 828 (1998).
9. C. Bertout, J. Krautter, C. Möllenhoff, and B. Wolf, Astron. Astrophys. **61**, 737 (1977).
10. R. C. Bless and B. D. Savage, Astrophys. J. **171**, 293 (1972).
11. J. Bouvier, E. Covino, O. Kovo, *et al.*, Astron. Astrophys. **299**, 89 (1995).
12. N. Calvet and E. Gullbring, Astrophys. J. **509**, 802 (1998).
13. C. Chavarria-K, Astron. Astrophys. **79**, L18 (1979).
14. M. Cohen and L. V. Kuhi, Astrophys. J., Suppl. Ser. **41**, 743 (1979).
15. K. P. Dere, E. Landi, H. E. Mason, *et al.*, Astron. Astrophys., Suppl. Ser. **125**, 149 (1997).
16. S. Edwards, Private communication (2002).
17. J. H. Elias, Astrophys. J. **224**, 857 (1978).
18. L. Errico, S. A. Lamzin, and A. A. Vittone, Astron. Astrophys. **357**, 951 (2000).
19. L. Errico, S. A. Lamzin, and A. A. Vittone, Astron. Astrophys. **377**, 557 (2001).
20. A. I. Gómez de Castro and M. Franqueira, ESA SP-1205 (Noordwijk, The Netherlands, 1997).
21. E. Guenther and F. Hessman, Astron. Astrophys. **268**, 192 (1993).
22. E. Gullbring, N. Calvet, J. Muzerolle, and L. Hartmann, Astrophys. J. **544**, 927 (2000).
23. P. Hartigan, S. Edwards, and L. Ghandour, Astrophys. J. **452**, 736 (1995).
24. L. Hartmann and J. R. Stauffer, Astron. J. **97**, 873 (1989).
25. W. Herbst, D. K. Herbst, E. J. Grossman, and D. Weinstein, Astron. J. **108**, 1906 (1994).
26. G. A. Hirth, R. Mundt, and J. Solf, Astron. Astrophys., Suppl. Ser. **126**, 437 (1997).
27. A. H. Joe, Astrophys. J. **110**, 424 (1949).
28. C. M. Johns-Krull and J. A. Valenti, Astrophys. J. **561**, 1060 (2001).
29. S. J. Kenyon, L. Hartmann, R. Hewett, *et al.*, Astron. J. **107**, 2153 (1994).
30. S. J. Kenyon and L. Hartmann, Astrophys. J., Suppl. Ser. **101**, 117 (1995).
31. N. E. Kurochkin, Astron. Tsirk. **1134**, 1 (1980).
32. V. G. Kurt and S. A. Lamzin, Astron. Zh. **72**, 364 (1995) [Astron. Rep. **39**, 322 (1995)].
33. C. Leinert, H. Zinnecker, N. Weitzel, *et al.*, Astron. Astrophys. **278**, 129 (1993).
34. S. A. Lamzin, in *Structure and Emission Properties of Accretion Disks: Proceedings of the IAU Colloquium No. 129, Paris, 1990,* Ed. by C. Bertout, S. Collin-Souffrin, and J. P. Lasota, 1991, p. 461.
35. S. A. Lamzin, Astron. Zh. **75**, 367 (1998) [Astron. Rep. **42**, 322 (1998)].
36. D. Lynden-Bell and J. E. Pringle, Mon. Not. R. Astron. Soc. **168**, 603 (1974).
37. S. Yu. Melnikov, K. N. Grankin, and O. V. Ezhkova, Private communication (2002).
38. J. C. Raymond and B. S. Smith, Astrophys. J., Suppl. Ser. **35**, 419 (1977).
39. M. M. Romanova, G. V. Ustyugova, A. V. Koldoba, and R. V. E. Lovelace, Astrophys. J. (2002) (in press).
40. M. J. Seaton, Mon. Not. R. Astron. Soc. **187**, 75 (1979).
41. N. I. Shakura and R. A. Sunyaev, Astron. Astrophys. **24**, 337 (1973).
42. M. Simon, T. L. Beck, T. P. Greene, *et al.*, Astron. J. **117**, 1594 (1999).
43. K. W. Smith, G. F. Lewis, I. A. Bonnell, *et al.*, Mon. Not. R. Astron. Soc. **304**, 367 (1999).
44. J. A. Valenti, G. Basri, and C. M. Jones, Astron. J. **106**, 2024 (1993).
45. J. A. Valenti, C. M. Johns-Krull, and J. L. Linsky, Astrophys. J., Suppl. Ser. **129**, 399 (2000).
46. D. A. Verner, G. J. Ferland, K. T. Korista, and D. G. Yakovlev, Astrophys. J. **465**, 487 (1996).
47. Wm. B. Weaver and G. Jones, Astrophys. J., Suppl. Ser. **78**, 239 (1992).
48. R. J. White and A. M. Ghez, Astrophys. J. **556**, 265 (2001).
49. Ya. B. Zel'dovich and Yu. P. Raizer, *Physics of Shock Waves and High-Temperature Hydrodynamic Phenomena* (Nauka, Moscow, 1966; Academic, New York, 1966).

Translated by V. Astakhov

Astronomy Letters, Vol. 28, No. 10, 2002, pp. 691–700. Translated from Pis'ma v Astronomicheskiĭ Zhurnal, Vol. 28, No. 10, 2002, pp. 764–774.

Nova Monocerotis 2002 (V838 Mon) at Early Outburst Stages

V. P. Goranskii[1]*, A. V. Kusakin[1], N. V. Metlova[1], S. Yu. Shugarov[1], E. A. Barsukova[2], and N. V. Borisov[2]

[1] *Sternberg Astronomical Institute, Universitetskiĭ pr. 13, Moscow, 119992 Russia*

[2] *Special Astrophysical Observatory, Russian Academy of Sciences, Nizhniĭ Arkhys, Karachai-Cherkessian Republic, 369167 Russia*

Received April 8, 2002

Abstract—We obtained $UBVR$ photometric and spectroscopic observations during the outburst of V838 Mon. Before its outburst, the B brightness of the star had been stable ($\sim 15\overset{m}{.}85$) for 45 years. This was a blue star with the color index $(B-V)_0 = -0\overset{m}{.}03 \pm 0\overset{m}{.}1$ and may have been a cataclysmic variable. In the middle of March 2002, the outburst amplitude reached $8\overset{m}{.}1$ in B. The star has the counterpart V1006/7 in M 31 in luminosity at maximum and in spectrum. The unusual spectrum at the premaximum stage originated in the expanding photosphere of a cool K-type giant. The expansion velocity of the photosphere was 150 km s^{-1}; the maximum velocity in the expanding stellar envelope reached 500 km s^{-1}. The absorption components of neutral metal lines were enhanced by a factor of 3 or 4 compared to a normal K-type star. No overabundance of s-process elements was found. One day before the brightness peak, an intense Hα emission line with broad wings, FWZI = 3100 km s^{-1}, and numerous lines of ionized metals appeared in V838 Mon, which is characteristic of normal classical novae. We show light, color, and spectral variations of the object. © *2002 MAIK "Nauka/Interperiodica"*.

Key words: *stars—variable and peculiar, stars—properties and classification, stars—structure and evolution.*

INTRODUCTION

V838 Mon, the peculiar Nova Monocerotis 2002 ($7^{\rm h}04^{\rm m}04\overset{s}{.}85$, $-3°50'51\overset{''}{.}1$, 2000), was discovered by Brown (2002) on January 6, 2002. From January 1999 until December 21, 2001, the star was still fainter than $12\overset{m}{}$ (Bedient 2002). Before its outburst, its brightness was $15\overset{m}{.}5$ in V and it was included in catalogs as GSC 4822.39 and IRAS 07015–0346 (Kato 2002). The star has the following magnitudes in the 2MASS IR sky survey: $J = 13\overset{m}{.}905$, $H = 13\overset{m}{.}480$, and $K = 13\overset{m}{.}347$. The preoutburst IR colors of the star, as inferred from the IRAS and 2MASS data, are unusual for a stellar object.

According to photographic observations (the Stardial archive) before its discovery, the star was visible at $R = 9\overset{m}{.}6$ on December 31, 2001 reached a plateau at $R = 8\overset{m}{.}9$ near January 5, 2002 (JD 2452280) and then gradually faded. Its color indices on January 14, 2002, were very red: $B-V = 1\overset{m}{.}832$ and $V-R = 0\overset{m}{.}916$ (Kimeswenger and Lederle 2002a). The outburst spectrum of the star in January 2002 was an absorption spectrum and unusual for novae. Wagner *et al.* (2002) and Della Valle and Iijima (2002) identified the strongest λ5855, 6142, and 6497 Å lines having P Cyg profiles with Ba II lines and the λ5897 Å line with the Na I D_2 and D_1 doublet. The Hα line was in absorption and weak. There were many Fe, Ca, and O absorption lines characteristic of the photosphere of a late-type star. The photosphere expansion velocity was estimated from absorption features in the P Cyg profiles to be 380–500 km s^{-1}. In addition, there were no TiO and C_2 bands commonly observed in late-type stars. It was noted that V838 Mon was a peculiar slow nova or a post-AGB star rather than a classical nova.

Zwitter and Munari (2002) interpreted the January 26, 2002, spectrum differently. They attributed the intense λ5270, 5857, and 6500 Å lines to Ca I, although it remains unclear why the most intense Ca I λ6717 Å line is not observed. According to their interpretation, there are no Ba lines in the spectrum! They also identified Na I, Si I, S I, Ni I, Y II, Zr II, C I, Cr I, Gd II, Fe I, and Ti I lines. The photosphere expansion velocities measured from the minima of absorption components were -252 km s^{-1}, and the maximum velocities reach -458 km s^{-1}. The color excess was estimated from interstellar Na I and K I lines to be $E(B-V) = 0\overset{m}{.}80$. The distance to the star

*E-mail: goray@sai.msu.ru

1063-7737/02/2810-0691$22.00

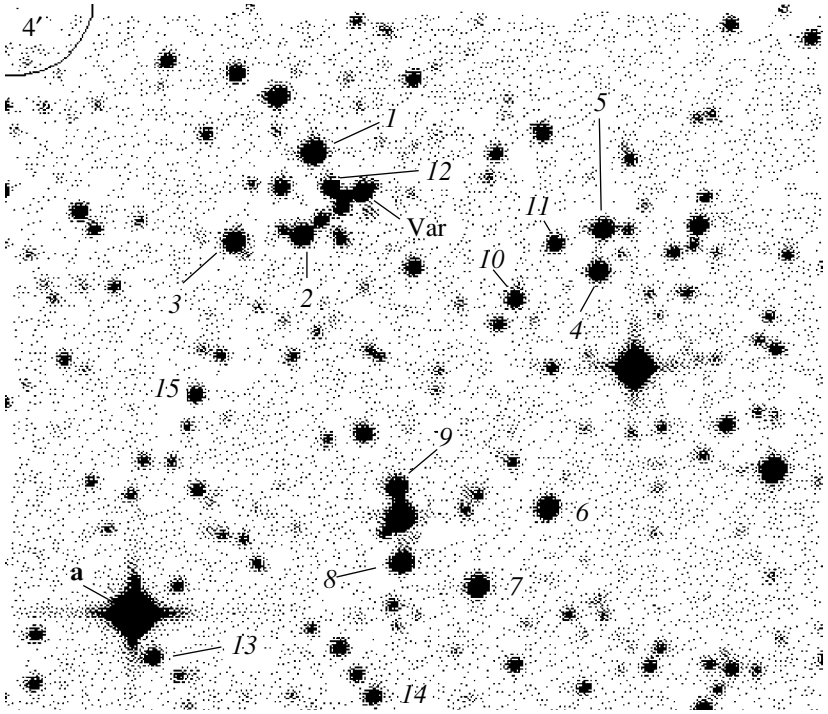

Fig. 1. A portion of the DSS digital image showing the field around V838 Mon (Var). The B magnitudes of the comparison stars are (*1*) 14.61; (*2*) 15.48; (*3*) 15.65; (*4*) 15.86; (*5*) 15.82; (*6*) 15.27; (*7*) 15.04; (*8*) 15.48; (*9*) 15.73; (*10*) 17.02; (*11*) 17.16; (*12*) 16.76; (*13*) 16.60; (*14*) 17.02; (*15*) 17.52.

corrected for Galactic reddening toward V838 Mon was found to be 3 kpc. In March 2002, a light echo was detected near the star (Henden *et al.* 2002); its observations yielded a smaller distance, 700 pc.

Broad and shallow water molecular bands and deep CO bands were detected in the J-band IR spectrum of V838 Mon. The Brackett lines of atomic hydrogen were in absorption and exhibited no P Cyg profiles. Many lines of neutral Fe, Mg, and Si were noticeable (Geballe *et al.* 2002). All these spectral manifestations are completely atypical of novae whose photospheric temperatures at early outburst stages are so high that the molecules are dissociated and the metal atoms are ionized.

On February 2, 2002 (JD 2452308), a second strong outburst began in the star; on February 6 (JD 2452312), its brightness reached a maximum of $6^m.66$ in V. A strong Hα emission line appeared, with its wings extending up to 30 Å on both sides (Morrison 2002). The Na I D_2 and D_1 lines were still present, but lines of ionized species, Fe II, Ti II, Cr II, Mg II, Si II, etc., appeared, which is characteristic of normal novae (Iijima and Della Valle 2002). Kaeufl *et al.* (2002) reported the formation of dust; they observed an IR silicate absorption feature on February 11.

Here, we present the results of our study of V838 Mon in quiescence before its outburst, the $UBVR$ photometry performed at the Sternberg Astronomical Institute (SAI), and the optical spectroscopic observations carried out at the Special Astrophysical Observatory (SAO).

V838 Mon BEFORE ITS OUTBURST

The Nova image on Palomar prints is a blend of several faint components (Fig. 1). We measured the outburst position of the star with respect to 16 reference stars from the USNO A1.0 astrometric catalog by using the CCD image obtained with the K-585 array on the 1-m Zeiss telescope:

$$7^h04^m04^s.781, \quad -3°50'51''.02, 2000;$$

the measurement accuracy is $\pm 0''.22$. The brightest star of the blend on the digital Palomar images (Var in Fig. 1) has the mean coordinates

$$7^h04^m04^s.765, -3°50'50''.95, 2000$$

with an $\pm 0''.16$ accuracy, which confirms that the Nova is identical to this star on the Palomar prints.

For our photometric study, we used digital images of the V838 Mon field from the Digitized Sky Survey (DSS) and from the archive of the US Naval Observatory Flagstaff Station (USNO FS; http://ftp.nofs.navy.mil). We used the code for digital

Table 1. Measurements of V838 Mon from sky surveys

JD 2400000+	Time	Magnitude	Accuracy	Band	Survey
33298.8	1953.0445	$15^m.95$	$\pm0^m.08$	B	POSS-I
33298.8	1953.0445	14.60	±0.08	R	POSS-I
45350.7	1983.0431	15.65	±0.08	B	UKST
45352.0	1983.045	14.77	±0.08	R	UKST
47590.5	1989.173	14.89	±0.08	R	UKST

image processing written by V.P. Goranskii. When processing the images of V838 Mon, we subtracted close components from the star profile. We measured a standard photometric B and R sequence of faint stars to the 18th magnitude on specially obtained CCD images. Our measurements of V838 Mon are given in Table 1. The $B-R$ color index was, on average, $1^m.1$.

The images of V838 Mon were also found on 26 plates of the SAI stacks taken with the 40 cm astrograph at the Crimean Station from 1949 until 1994. Eye magnitude estimates for the star on these plates tied in to the B-band CCD sequence (see Fig. 1) were obtained by S.Yu. Shugarov and are given in Table 2.

PHOTOMETRY

The photoelectric photometry of V838 Mon was performed by N.V. Metlova at the Crimean Station of the SAI with the UBV photometer designed by V.M. Lyuty on the 60-cm Zeiss telescope and by A.V. Kusakin at the Tien Shan Astronomical Observatory of the Fesenkov Astrophysical Institute, Kazakhstan, with a single-channel $WBVR$ photometer on the 48-cm AZT-14 reflector. The comparison star in the Crimean observations was GSC 4822.3559 (star **a** in Fig. 1) with the following magnitudes obtained by the method of absolute photometry: $U = 10^m.214$, $B = 10^m.743$, and $V = 10^m.694$ (tied in to the standard star HD 45067). In the Tien Shan observations, we used the comparison stars HD 54810A and HD 54990, whose $WBVR$ magnitudes are available in the catalog by Kornilov *et al.* (1991). The W photometric band was introduced by Straizis (1977) on the short-wavelength side of the Balmer jump to increase the accuracy of photometric reduction outside the atmosphere.

In January and March, V.P. Goranskii and E.A. Barsukova carried out BVR CCD observations of V838 Mon with the 1-m Zeiss reflector at the SAO and tied in the standard GSC 4822.3559 to the local sequence near HQ Mon. The tie-in results are as follows: $B = 10^m.745$, $V = 10^m.626$, and $R = 10^m.629$. Our photoelectric and CCD observations are given in Table 3.

To study the light curves of V838 Mon, we also used the CCD observations by F. van Wyk, D. West, S. Kiyota, P. Corelli, L. Kral, J.M. Llapasset, F. Lomoz, A. Oksanen, O. Pejcha, L. Smelcer, P. Sobotka, and K. Hornoch published in VSNET (vsnet-campaign-v838mon), as well as the observations by Kimeswenger and Lederle (2002a, 2002b). These observations were performed with different detectors and instruments, were tied in to different comparison stars, and have significant systematic deviations. We reduced all these data to the single system of the most accurate and homogeneous Crimean series obtained by N.V. Metlova by applying corrections to each independent series to achieve the closest match between the light-curve segments under study. The reduction results are shown in Fig. 2, which presents the $UBVR$ light and color curves. In Table 3, no corrections were applied for systematic deviations.

We made up for the deficiency of R-band observations using the eye estimates obtained by V.P. Goranskii with an instrument composed of a photoelectric

Table 2. Photographic observations of V838 Mon before its discovery

JD 2400000+	B	JD	B
33184.592	15.67	48298.374	15.81
34824.247	15.7 ::	48320.301	15.73
40292.326	15.91	48321.265	15.90
46764.541	16.00	48325.259	15.85
46764.574	15.88	48327.319	15.76
48244.399	15.80	48626.423	15.79
48250.464	15.83	48653.436	15.69
48273.392	15.88	48716.281	15.96
48274.362	15.92	49006.442	15.85
48276.382	15.83	49031.372	15.92
48294.384	15.92	49359.424	15.93
48295.396	15.85 :	49362.400	15.81
48297.371	15.96	49394.325	15.90

Table 3. Observations of V838 Mon

JD 2452000+	*U*	*B*	*V*	*R*	Observer	JD 2452000+	*U*	*B*	*V*	*R*	Observer
288.390	–	11.77	9.92	8.84	B, G	321.4253	10.41	9.38	7.95	–	M
288.412	–	11.70	9.95	8.81	B, G	321.4301	10.37	9.35	7.95	–	M
288.413	–	11.73	9.93	8.81	B, G	322.1234	10.44	9.58	7.91	6.65	K
289.380	–	11.76	9.92	8.82	B, G	322.1437	10.34	9.51	7.92	6.67	K
289.384	–	11.76	9.92	8.81	B, G	324.2827	10.81	9.64	8.01	–	M
291.391	–	11.89	10.00	8.83	B, G	324.2876	10.83	9.64	8.00	–	M
294.2557	13.26	11.90	10.12	8.74	K	324.2924	10.81	9.63	7.98	–	M
294.2761	13.34	11.92	10.14	8.76	K	324.2973	10.82	9.65	8.00	–	M
307.3552	15.01	12.75	10.88	–	M	324.3021	10.81	9.65	8.03	–	M
307.3837	14.87	12.75	10.90	–	M	324.3070	10.83	9.64	8.01	–	M
307.4073	14.36	12.76	10.86	–	M	326.1102	10.91	9.95	8.08	6.69	K
308.3694	10.08	9.44	8.22	–	M	326.1322	10.79	9.92	8.09	6.67	K
308.3864	10.02	9.40	8.19	–	M	326.1646	10.84	9.95	8.10	6.70	K
308.3909	10.00	9.41	8.18	–	M	327.2137	11.06	10.03	8.12	6.67	K
308.3958	9.99	9.40	8.17	–	M	327.2426	10.95	10.00	8.09	6.64	K
308.4010	9.96	9.38	8.16	–	M	328.2104	11.16	10.11	8.15	6.65	K
308.4062	9.97	9.38	8.15	–	M	328.2439	10.93	10.01	8.10	6.63	K
308.4114	9.96	9.35	8.14	–	M	332.3335	11.74	10.22	8.24	–	M
308.4166	9.96	9.34	8.13	–	M	332.3377	11.59	10.23	8.25	–	M
308.4215	9.94	9.33	8.13	–	M	335.3010	11.51	9.88	8.01	–	M
308.4267	9.92	9.33	8.13	–	M	335.3069	11.47	9.90	8.01	–	M
308.4315	9.91	9.33	8.11	–	M	335.3132	11.49	9.89	8.00	–	M
308.4368	9.90	9.30	8.10	–	M	339.3411	10.63	9.15	7.45	–	M
308.4416	9.88	9.29	8.13	–	M	339.3466	10.62	9.15	7.47	–	M
309.2211	9.17	8.77	7.64	–	M	339.3529	10.61	9.14	7.46	–	M
309.2260	9.18	8.78	7.64	–	M	343.2738	10.50	8.93	7.24	–	M
309.2305	9.19	8.78	7.61	–	M	343.2790	10.50	8.93	7.25	–	M
309.2357	9.17	8.78	7.64	–	M	343.2842	10.48	8.94	7.24	–	M
309.2513	9.16	8.78	7.62	–	M	346.2823	10.80	9.03	7.25	–	M
313.2285	8.45	8.04	6.98	–	M	346.2885	10.76	9.02	7.24	–	M
313.2324	8.47	8.04	6.99	–	M	346.2951	10.79	9.03	7.24	–	M
313.2362	8.47	8.05	6.98	–	M	346.3010	10.78	9.03	7.27	–	M
313.2403	8.48	8.04	6.99	–	M	347.2249	10.90	9.08	7.24	–	M
313.2438	8.47	8.05	6.98	–	M	347.2312	10.94	9.10	7.26	–	M
313.2483	8.47	8.05	6.98	–	M	347.2371	11.00	9.15	7.29	–	M
313.2521	8.48	8.05	6.99	–	M	347.2440	10.93	9.10	7.28	–	M
313.2563	8.47	8.05	6.99	–	M	347.330	–	8.81	7.53	6.11	B, G
313.2605	8.48	8.06	6.99	–	M	348.3460	11.16	9.25	7.38	–	M
313.2640	8.49	8.06	6.99	–	M	348.3519	11.16	9.22	7.37	–	M
313.2681	8.49	8.05	6.99	–	M	353.2211	11.90	9.75	7.68	–	M
313.2841	8.50	8.06	6.99	–	M	353.2270	11.90	9.75	7.68	–	M
313.2890	8.51	8.07	7.00	–	M	353.2332	11.91	9.73	7.67	–	M
313.2924	8.51	8.08	7.01	–	M	353.2391	11.91	9.73	7.69	–	M
321.4107	10.40	9.37	7.95	–	M	353.2454	11.98	9.74	7.69	–	M
321.4155	10.39	9.37	7.94	–	M	353.2516	11.89	9.75	7.68	–	M
321.4204	10.41	9.37	7.94	–	M	353.2579	11.90	9.72	7.69	–	M

Note. The following abbreviations are used in the Observer column. B: E.A. Barsukova; G: V.P. Goranskii; K: A.V. Kusakin; and M: N.V. Metlova. In the *U* column, Kusakin's observations were carried out in the UV *W* band.

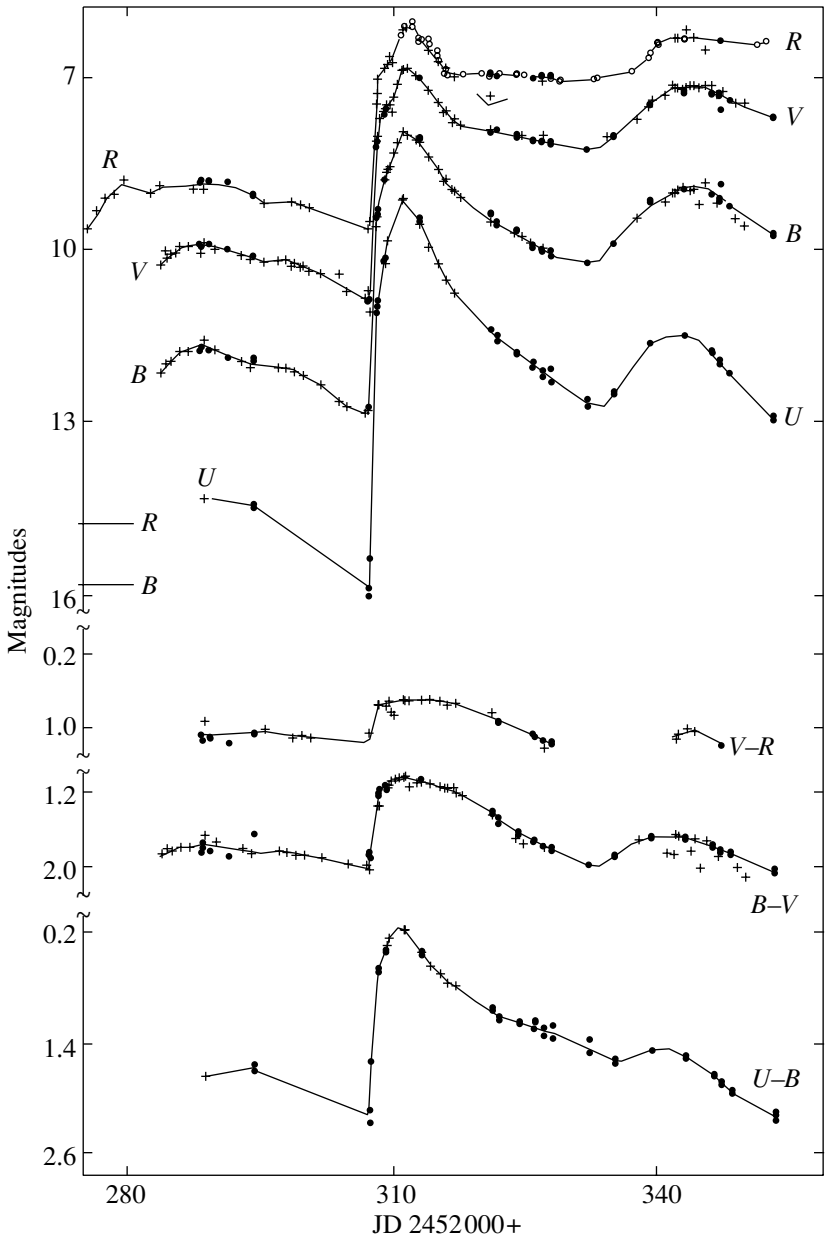

Fig. 2. The $UBVR$ light and color curves of V838 Mon. The horizontal lines near the y axis mark the preoutburst B and R brightness levels. The crosses represent the observations taken from VSNET and IAU Circulars. For clarity, the U light curve was displaced downward by 1^m.

image intensifier (with a microchannel plate) and a 5-cm lens. The instrument response curve has a maximum in the red, and the observations are close to the R system. These observations are highlighted by circles in Fig. 2.

THE LIGHT AND COLOR CURVES

According to our data, the brightness of V838 Mon from 1949–1994 was relatively stable; its variability amplitude did not exceed $0^m.4B$. The observations from the SAI plate stacks and digital databases span 45 years. The mean brightness was $15^m.85$ in B and $14^m.76$ in R. The $B-R$ color index of the star was, on average, $1^m.1$, which corresponds to $B-V = 0^m.6$.

The premaximum $B-R$ color index in January 2002 was much redder than that before the outburst: $B-R = 2^m.9$; it was increasing with time. The rise to maximum began between JD 2452307.6 and JD 2452308.2. Fading similar to the fading observed before the shock wave emerges on the surface in pulsating RR Lyrae variables was noticeable before the rise. The calculations by Christy (1966) show

Table 4. The SAO spectroscopic observations of V838 Mon

JD 2452000+	Date, 2002	Time, UT	Number of spectra	λ, Å	Resolution, Å
296.458	Jan. 21	22.59	5	5640–7300	5.0
296.481	Jan. 21	23.32	3	4100–5760	3.3
298.451	Jan. 23	22.50	4	4120–4930	2.2
298.497	Jan. 23	23.50	3	6190–7040	2.5
311.287	Feb. 5	18.53	23	6190–7040	2.2
311.354	Feb. 5	20.30	18	4100–4960	2.5
322.313	Feb. 16	19.31	5	6190–7040	2.3

that the preshock gas is sharply compressed; as a result, its opacity increases, which causes a fading. This explanation is also valid for V838 Mon. After the primary rise until JD 2452308.5, the brightening slowed down and a maximum in the V band, $6\overset{m}{.}7$, was reached on JD 2452312.0 (February 6, 2002). The outburst amplitude, measured from the premaximum level before the outburst, strongly depends on wavelength: $6\overset{m}{.}8$ in U, $5\overset{m}{.}0$ in B, $4\overset{m}{.}1$ in V, and $3\overset{m}{.}6$ in R. The total amplitude was $8\overset{m}{.}07$ in B (variability range, $7\overset{m}{.}93$–$16\overset{m}{.}0$) and $8\overset{m}{.}77$ in R ($6\overset{m}{.}12$–$14\overset{m}{.}89$). After the outburst maximum, the star became bluer ($B-R = 1\overset{m}{.}75$) but was still redder than in quiescence. Whereas the star is comparable to classical novae in outburst amplitude, its color behavior is atypical of novae.

The color indices clearly contain a component attributable to interstellar reddening. The color excess inferred from interstellar lines is $E(B-V) = 0\overset{m}{.}80$ (Zwitter and Munari 2002), but the photometric color excess $E(B-V)$ measured from the two-color diagram is only $0\overset{m}{.}63 \pm 0.05$ and the visual extinction is $A_V = 1\overset{m}{.}9$.

A gradual fading (except the R band) and an increase in the color indices are observed after the maximum on February 6. A local maximum occurred on JD 2452344, 32 days after the primary maximum, and a new decrease in the color indices is associated with it. In the middle of March (JD 2452355), the color indices were as large as those at the premaximum state. A flat maximum was observed in the R band. The brightness decline rate decreases with increasing wavelength. Such a behavior suggests a cooling of the star's expanding, optically thick envelope during which the maximum of the energy distribution is gradually displaced toward longer wavelengths.

SPECTROSCOPY

The spectroscopic observations were carried out by N.V. Borisov with the UAGS spectrograph on the 1-m Zeiss reflector at the SAO. A list of the spectra obtained, the wavelength ranges covered, and resolutions are given in Table 4. The observations were reduced by E.A. Barsukova using standard procedures in the MIDAS environment. After the reduction, all of the spectra obtained during each night in the chosen range were added.

To identify spectral lines, we used the database of Coluzzi (1993) supplemented by some elements with weak lines from the tables published by Striganov and Sventitskii (1966). The spectra were analyzed by using the computer codes for cross-correlation and spectral analyses developed by V.P. Goranskii. The latter code makes it possible to identify all lines of a given ion in the spectrum by taking into account the object's radial velocity.

Figure 3 shows the star's spectrum taken on January 21 at the premaximum stage. Judging by the energy distribution, this is a late K-type spectrum. A weak Hα absorption line at zero velocity, a strong broad line of the Na I $D_1 + D_2$ doublet, and strong λ6500, 6137, and 5851 Å lines whose identification is so far questionable are seen in the red. A "forest" of absorption lines, which in some places suppress the continuum emission, is seen in the spectral range λ4800–5600 Å.

To confirm the presence of s-process elements in the spectrum, we compared the spectrum of V838 Mon with the spectra of barium stars from Bidelman and Keenan (1951), Zach (1989a, 1989b, 1990), and Smith *et al.* (1984). In the spectra of barium stars, the lines of the s-process elements Ba, Y, Zr, La, Ce, Pr, Nd, and Sm are saturated as compared to the iron-group elements (Bidelman and Keenan 1951). The nucleosynthesis elements are known (McClure 1983) to fall into the envelopes of barium stars during the AGB stage of the component and mass transfer in the binary system. Two well-known stars, FG Sge and V4334 Sgr, underwent helium shell flashes at the post-AGB stage, and the

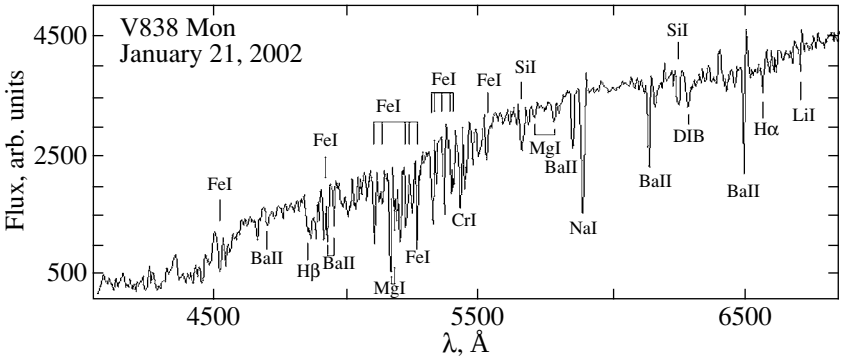

Fig. 3. The pre-maximum spectrum of V838 Mon with the principal lines identified.

lines of *s*-process elements appeared in their spectra. Therefore, we compared the spectra of V838 Mon with the spectra of FG Sge (Acker *et al.* 1982). The spectrum of V838 Mon turned out to have little in common both with barium stars and with FG Sge. Only Ba lines and, occasionally, Zr lines could be confirmed.

Next, we looked at how the spectrum of V838 Mon correlates with the spectrum of the normal K0 V star HD 23524 from the database obtained by Jakoby *et al.* (1984). The spectra were found to correlate well with each other. Figure 4 shows the cross-correlation function between the spectra of HD 23524 and V838 Mon. In order to use the entire spectrum in a wide range (λ4100–6300 Å), we converted the wavelength scale to the scale of natural logarithms. Indeed, it follows from the formula for the Doppler effect $dv/c = d\lambda/\lambda = d(\ln\lambda)$ that $dv = cd(\ln\lambda)$. In Fig. 4, the radial velocity represents the argument of the cross-correlation function. We did not consider the spectrum beyond λ6300 Å, because absorption bands of the Earth's atmosphere dominate there. The correlation coefficient was found to be very high, 0.68! The shift in the maximum of the function (corrected for the radial velocity of HD 23524) corresponds to a low envelope expansion velocity, ~ -150 km s^{-1} (the uncertainty of our radial-velocity measurements is 20–30 km s^{-1}). Finally, in the last test, the relation between the equivalent widths of identical lines for the two stars shows that both spectra are dominated by the same lines but the lines in the spectrum of V838 Mon are a factor of 3 or 4 more intense.

Clearly, such an unusual spectrum with strong lines is formed in a rather dense, extended atmosphere above the star's photosphere or in the surrounding nebula that expands under the radiation pressure from the central star. Infrared observations confirm the existence of such a medium.

Taking the velocity -150 km s^{-1}, we reliably identified the strong λ6500 Å line as Ba II λ6496.9 Å. The identification of this line with Ca I (Zwitter and Munari 2002) is unlikely, because there are no traces of the stronger Ca I λ6717 Å line, which is well observed in K-type stars. Moreover, other weaker Ba II lines are also observed at the same radial velocity: we reliably identified the λ6769.6 Å line (with a P Cyg profile), the 6135.8/6141.7 doublet, and the 5853.7, 5784.2, 4957.2, 4934.1, 4554.0, 4216.0, 4130.0 Å lines. The λ6500 Å line may have the Fe I 6495.0 Å feature, which can broaden its profile, but the identification of the iron line with this feature gives a velocity of only -50 km s^{-1}. Note that Ba lines are also observed in the solar spectrum.

The strongest lines in the January 21 and 23 spectra are identified with the neutral species Mg I, Na I, Fe I, Ti I, Ca I, Cr I, and Si I (Fig. 3). The most interesting identification that has not yet been noticed by other researchers is the Li I λ6707 Å line with a P Cyg profile! The presence of Li is also confirmed by another, weak Li I λ6103.6 Å line.

The spectra recorded on February 5, one day before the maximum, exhibit an intense Hα emission line with broad wings; its full width at zero intensity is $FWZI = 3100$ km s^{-1} (Fig. 5a). The emission-line profile consists of a narrow component with $FWHM = 340$ km s^{-1} and a broad component with $FWHM \approx 1400$ km s^{-1}. The profile also shows an absorption component at a velocity of -300 km s^{-1}. Wings of the same width are traceable in the Hβ

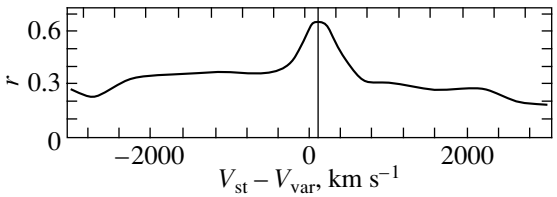

Fig. 4. The cross-correlation function for two spectra: the normal K0 V star HD 23524 and V838 Mon.

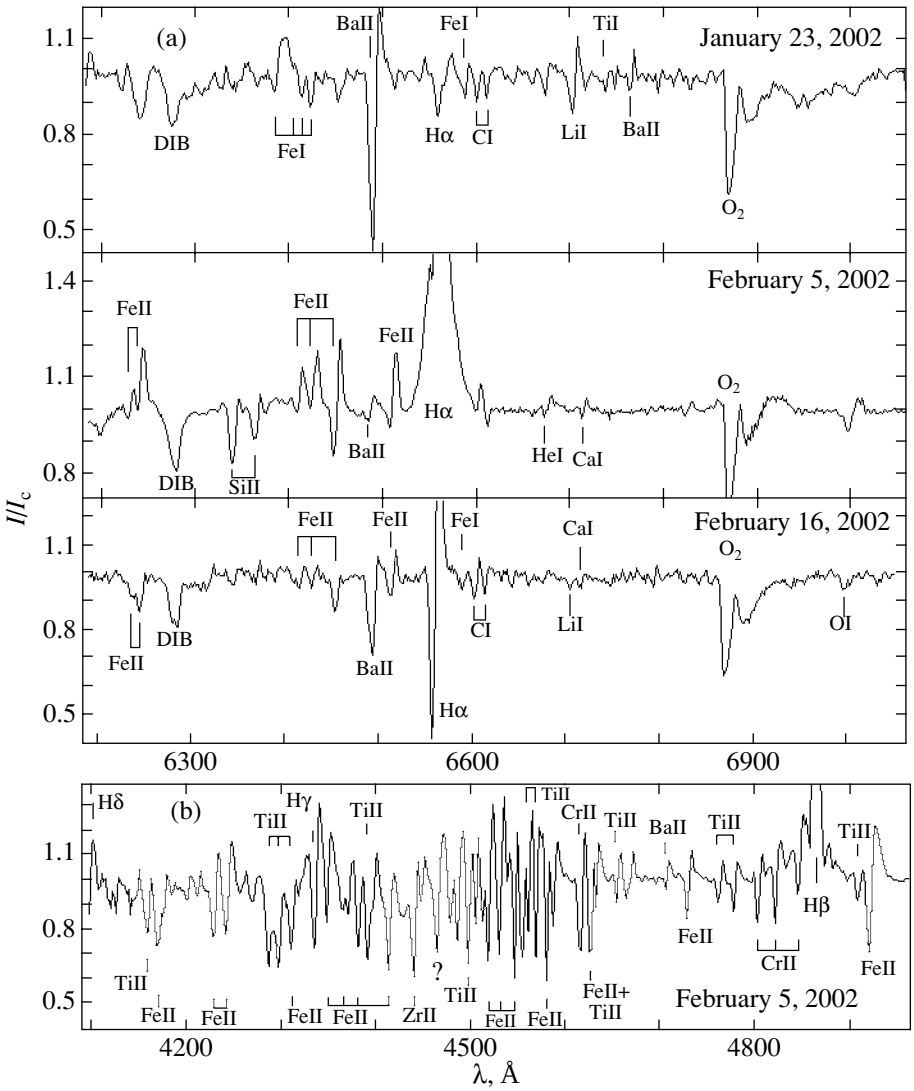

Fig. 5. (a) Comparison of the spectra near the Hα line at the premaximum stage on January 23, one day before the outburst maximum on February 5, and during the outburst decay on February 16. (b) The spectrum of V838 Mon one day before the maximum on February 5 near the Hβ line.

line; strong Cr II and Ti II lines with P Cyg profiles are superimposed on these wings (Fig. 5b). Morrison (2002) explains these wings as resulting from the scattering of Hα photons by electrons. Significant changes reflecting an increase in the excitation level occurred in the spectrum. Numerous lines of the same elements that were observed at the premaximum stage, but now of singly ionized species rather than of neutral species with distinct P Cyg, profiles appeared. The emission components of the profiles became particularly intense. He I lines appeared. Finally, the Ca I λ6717 Å line appeared in the red, while the Li I λ6707 Å line disappeared. At that time, Ba II λ6496.9 Å, the strongest line in the red, was barely seen. The velocities at the intensity minima of the absorption components reached -180 to -200 km s^{-1}. We explain these changes in terms of the shock emergence on the surface, which was accompanied by a rise in temperature and by an increase in the degree of ionization in the ambient matter.

The Hα line exhibits a P Cyg profile without high-velocity wings in the red spectrum taken on February 16 during the outburst decay. The emission component had $FWHM = 265$ km s^{-1}, and its mean velocity was $v_r = +110$ km s^{-1}. The absorption component at the intensity minimum shows $v_r = -220$ km s^{-1}. Deep Fe II, Si II, and Ti II absorption lines are still seen in the spectrum, but the same Ba II lines and still weak Fe I absorption lines appeared.

A weak Li I λ6707 Å line is seen again. The Ca I λ6717 Å line is still present. In the Internet, we found a later recorded spectrum of the star, on March 10 (C. Buil; http://www.astrosurf.com/buil/us/nmon/nmon.htm). At that time, the photosphere expansion velocity decreased to 60–70 km s^{-1}. In this spectrum, containing many absorption lines, we simultaneously identified two systems of absorption lines of the same elements, neutral and singly ionized, suggesting envelope stratification.

Only one feature, at λ6282 Å, appears to be the same in all spectra; its equivalent width is 2.78 ± 0.05 Å. We identify this with a diffuse interstellar band.

DISCUSSION

Let us consider the conclusions regarding the nature of the object and its outburst that can be drawn from our observations. The preoutburst photometric parameters can be assumed to be the following: $V = 15^m.25 \pm 0^m.1$ and $B-V = 0^m.60 \pm 0^m.1$. Taking into account our color excess $E(B-V) = 0^m.63$, we obtain $(B-V)_0 = -0^m.03 \pm 0^m.1$. If we took the color excess determined from interstellar lines, $E(B-V) = 0^m.80$ (Zwitter and Munari 2002), then the star would be even bluer: $(B-V)_0 = -0^m.20$. Thus, before its outburst, V838 Mon was a hot blue star. The visual extinction estimated from photometric data is $A_V = 1^m.9$. Taking the interstellar reddening in the Galactic plane (where the object under study is located) to be $1^m.6$ per kpc (Sharov 1963) and assuming the circumstellar extinction to be negligible compared to the interstellar extinction, we obtain the distance to the object, 1200 pc. This distance is consistent with the value determined from observations of the nebula, a light echo. In the V-band image obtained by Orio *et al.* (2002) on April 20, 2002 (111 days after the onset of the outburst on December 31, 2001), we measured the nebula radius, $16''.2 \pm 1''.0$, and distance, 1190 ± 70 pc. The object's luminosity in quiescence is then $M_V = 2^m.96 \pm 0^m.5$ or $L = 5.6L_\odot$. It is highly likely that the star was a cataclysmic system before its outburst, although its luminosity is higher than that for the brightest systems of this type (by $\approx 1^m$). The interpretation of the star as a white dwarf is ruled out because of its high luminosity, although it could be a hot subdwarf on its evolutionary path to white dwarfs at the post-AGB stage. The luminosity and color also rule out an AGB red giant.

The appearance of the Li I λ6707 Å line is of great importance. This line is usually encountered in the spectra of young stars. Lithium is rapidly depleted in nuclear reactions. In some of these reactions, it is an intermediate product. Cameron and Fowler (1971) predicted a mechanism for the appearance of lithium in stellar photospheres at late evolutionary stages, when all of the overlying stellar layers up to the outer layers of the envelope are mixed during a helium shell flash. During helium flashes in AGB red giants, lithium is ejected into the outer layers together with *s*-process elements. The ejection of Li and *s*-process elements into the photospheres was also observed at the post-AGB stage in FG Sge and V4334 Sgr (in which planetary nebulae, traces of the ejected envelopes, are also observed).

Asplund *et al.* (1997) point out that lithium can be produced in the stellar region where hydrogen burning has just begun, but earlier, the temperature of this region was lower than the temperature at which hydrogen burning takes place. This condition is satisfied via accretion of hydrogen-rich matter onto the surface of a white dwarf in calaclysmic systems and during nova outbursts. The appearance of the Li I line in the photosphere may be due to fast mixing in the slowly expanding envelope of V838 Mon, during which intermediate nucleosynthesis products were transported to the surface. Clearly, nucleosynthesis products must be present in ejected envelopes of all novae. In our case, however, the LiI line is observed only because of the low photospheric temperature. As yet, we have obtained no evidence of V838 Mon being a binary system, but this assumption is confirmed by the intense hydrogen lines occurring during the outburst.

Thus, we have two hypotheses regarding the nature of V838 Mon (Della Valle and Iijima 2002) and, accordingly, two scenarios for the subsequent development of its outburst.

(1) A helium shell flash at the post-AGB stage. In that case, we may expect the appearance of a spectrum with lines of *s*-process elements and, subsequently, the appearance of large carbon grains in the atmosphere and of related abrupt fadings.

(2) An outburst of a hydrogen-rich source on a white dwarf in a binary system and the scenario for a slow nova with passage to the nebular stage. If, however, the velocity of the envelope is too low for its detachment, then the envelope expansion can stop and the star can return first to a merged binary with a common photosphere and then back to a semidetached configuration.

Currently, the slow-nova scenario seems preferable.

THE COUNTERPART OF V838 Mon IN THE GALAXY M 31: V1006/7

If V838 Mon were placed in the galaxy M 31, then its magnitude at maximum would be $19^m.1$ in B. Nova

V1006/7 in M 31 (1988) also had an unusual spectrum, M0 Ie, and reached $18^m.2$ in B at maximum. Its spectrum, taken by Rich *et al.* (1989) (see the figure from their paper), is a precise copy of the spectrum for V838 Mon; it shows the same Ba II, Na I, and Li I λ6707 Å lines. Interestingly, Rich *et al.* identify the strong absorption line at λ6500 Å with a blend of Ba II, Ca I, and Fe I lines. Sharov (1990) detected another outburst of this Nova in 1968. The researchers of V1006/7 in M 31 solved the same problems as we did, and the star was classified in different studies as a nova and as a Lc:-type variable. This confused the compilers of Volume V of the GCVS; they included this star in their list under two different names but with the same coordinates (see also corrections to the GCVS Volume V).

CONCLUSIONS

Our data provide evidence that, given the low envelope expansion velocity, V838 Mon could be a very slow nova. Its premaximum stage resembles the F-supergiant stage for the slow Nova V723 Cas but develops at a lower temperature.

Before the outburst, the star was blue with the color index $(B-V)_0 = -0^m.03 \pm 0^m.1$ and may have been a cataclysmic variable.

The premaximum photospheric spectrum suggests a normal chemical composition, with the lines being enhanced by a factor of 3 to 4 compared to the spectra for stars of the same spectral type. This enhancement can be explained by absorption in a dense, extended atmosphere or in a circumstellar envelope. As yet no strong lines of s-process elements have been detected.

The spectra of V838 Mon exhibit the Li I λ6707 Å line. This may result from the ejection of hydrogen-burning products to the stellar surface during the outburst. It is well known that Li, Ba, and s-process elements appeared in the envelopes of two nova-like objects, V4334 Sgr and FG Sge, which passed through the helium shell flash stage, at late outburst stages and the events in V838 Mon could follow the same scenario.

ACKNOWLEDGMENTS

This study was supported in part by the Science and Technology Program "Astronomy" (project no. 1.4.2.2) and the Russian Foundation for Basic Research (project no. 02-02-16462). A.V. Kusakin is grateful to K.S. Kuratov, director of the Tien Shan Astronomical Observatory of the Fesenkov Astrophysical Institute, National Academy of Sciences, the Republic of Kazakhstan, for help and cooperation during the observations.

REFERENCES

1. A. Acker, M. Jashek, and F. Gleizes, Astron. Astrophys. **48**, 363 (1982).
2. M. Asplund, B. Gustaffson, D. L. Lambert, and N. Kameswara Rao, Astron. Astrophys. **321**, L17 (1997).
3. J. Bedient, IAU Circ., No. 7790 (2002).
4. W. R. Bidelman and P. C. Keenan, Astrophys. J. **114**, 473 (1951).
5. N. J. Brown, IAU Circ., No. 7785 (2002).
6. A. G. W. Cameron and W. A. Fowler, Astrophys. J. **164**, 111 (1971).
7. R. Coluzzi, Bull. Inf. CDS **23**, 7 (1993).
8. M. Della Valle and T. Iijima, IAU Circ., No. 7786 (2002).
9. T. R. Geballe, S. P. S. Eyres, A. Evans, and V. H. Tyne, IAU Circ., No. 7796 (2002).
10. A. Henden, U. Munari, and M. Schwartz, IAU Circ., No. 7859 (2002).
11. T. Iijima and M. Della Valle, IAU Circ., No. 7822 (2002).
12. G. H. Jakoby, D. A. Hunter, and C. A. Christian, Astron. Astrophys., Suppl. Ser. **56**, 257 (1984).
13. H. U. Kaeufl, G. Locurto, F. Kerber, and B. Hejiligers, IAU Circ., No. 7831 (2002).
14. T. Kato, IAU Circ., No. 7786 (2002).
15. S. Kimeswenger and C. Lederle, IAU Circ., No. 7796 (2002a).
16. S. Kimeswenger and C. Lederle, IAU Circ., No. 7812 (2002b).
17. V. G. Kornilov, I. M. Volkov, A. I. Zakharov, *et al.*, Tr. Gos. Astron. Inst., Mosk. Gos. Univ. **63**, 4 (1991).
18. R. D. McClure, Astrophys. J. **268**, 264 (1983).
19. N. D. Morrison, IAU Circ., No. 7829 (2002).
20. M. Orio, D. Harbeck, J. Gallagher, and C. Woodward, IAU Circ., No. 7892 (2002).
21. R. M. Rich, J. Mould, A. Picard, *et al.*, Astrophys. J. **341**, L51 (1989).
22. V. V. Smith, G. Wallerstein, K. Ebneter, and E. Olmstead, Astron. Astrophys., Suppl. Ser. **55**, 439 (1984).
23. V. Straizys, *Multicolor Stellar Photometry* (Mokslas, Vil'nyus, 1977; Pachart Publ. House, Tucson, 1992).
24. A. R. Striganov and N. S. Sventitskii, *Tables of Spectral Lines of Neutral and Ionized Atoms* (Atomizdat, Moscow, 1966; Plenum, New York, 1968).
25. A. S. Sharov, Astron. Zh. **40**, 900 (1963) [Sov. Astron. **7**, 689 (1963)].
26. A. S. Sharov, Pis'ma Astron. Zh. **16**, 199 (1990) [Sov. Astron. Lett. **16**, 85 (1990)].
27. R. M. Wagner, J. P. Halpern, and M. Jackson, IAU Circ., No. 7785 (2002).
28. L. A. Zach, Soobshch. SAO RAN **60**, 70 (1989a).
29. L. A. Zach, Soobshch. SAO RAN **63**, 160 (1989b).
30. L. A. Zach, Soobshch. SAO RAN **65**, 45 (1990).
31. T. Zwitter and U. Munari, IAU Circ., No. 7812 (2002).

Translated by N. Samus'

Astronomy Letters, Vol. 28, No. 10, 2002, pp. 701–712. Translated from Pis'ma v Astronomicheskiĭ Zhurnal, Vol. 28, No. 10, 2002, pp. 775–787.

Neutral Hydrogen around the Oxygen-Sequence Wolf–Rayet Star WR 102 and the Nebula G2.4+1.4

I. V. Gosachinskij[1]* and T. A. Lozinskaya[2]

[1]*Special Astrophysical Observatory, St. Petersburg Branch, Russian Academy of Sciences, Pulkovo, St. Petersburg, 196140 Russia*

[2]*Sternberg Astronomical Institute, Universitetskiĭ pr. 13, Moscow, 119992 Russia*

Received May 13, 2002

Abstract—We carried out the first 21-cm line observations of an extended region around the Wolf–Rayet star WR 102 and the associated nebula G2.4+1.4 with the RATAN-600 radio telescope. An irregular H I shell was identified. Its maximum expansion velocity reaches $\sim$50 km s^{-1}, and its outer diameter (at a distance of 3 kpc) is 56 pc. The mechanical luminosity of the stellar wind required to produce the observed shell is estimated to be $\sim 0.8 \times 10^{38}$ erg s^{-1}; the age of the shell is $\sim 3.4 \times 10^5$ yr. We compare the inferred parameters of the H I shell with the structure and kinematics of the ionized nebula and with the dust distribution in the region. © *2002 MAIK "Nauka/Interperiodica"*.

Key words: *interstellar medium, gaseous nebulae; radio sources.*

INTRODUCTION

The effects of strong winds from Wolf–Rayet (WR) stars on the neutral component of the interstellar medium have been studied for several decades. To date, 21-cm H I line observations have been carried out for twenty WR stars and their surrounding nebulae. The first positive result was obtained by Cappa and Niemela (1984), who discovered an H I cavity, 100 pc in diameter, around the star WR 48 (θ Mus). Current observations are performed mostly with the 100-m radio telescope in Bonn (see, e.g., Arnal 1992; Arnal *et al.* 1999) and with the DRAO aperture-synthesis system in Canada (Pineault *et al.* 1996; Arnal 2001). References to the results of other observers who analyzed the H I distribution around WR stars with these instruments can be found in these papers.

H I cavities have been detected more or less reliably around almost all of the WR stars studied. The cavity sizes range from 30 to 100 pc and are oval rather than round in shape. The deficit of gas in cavities compared to the background typically reaches several thousand $M_\odot$. The expansion velocities of the clumpy H I shells around cavities lie within the range 10–15 km s^{-1}, and only for WR 128 did Arnal *et al.* (1999) find the expansion velocity to be 80 ± 22 km s^{-1}.

It should be noted that almost none of the authors detected regular H I shells around cavities with confidence. Virtually all WR stars are greatly displaced from the centers of the associated cavities. When studying the H I region around the star WR 134, Gervais and St Louis (1999) used Hipparcos data to show that the eccentric position of this star in the cavity could be explained by its proper motion.

In several cases, IRAS data also revealed extended dust shells or cavities around WR stars. Extended infrared shells and cavities were found around the nebula NGC 6888 and the star WR 136 (Nichols-Bohlin and Fesen 1993; Marston 1995; Lozinskaya *et al.* 1997), as well as around the stars WR 134 (Pineault *et al.* 1996), WR 125 (Arnal and Mirabel 1991), and WR 140 (Arnal 2001). Goss and Lozinskaya (1995) investigated infrared radiation in the vicinity of two oxygen-sequence WR (WO) stars, including WR 102 discussed here.

The WO stars are of particular interest, because they are rare and possess the strongest winds among the WR stars.

Only six WO stars have been identified among the six hundred WR stars in the Local Group galaxies; three of them, including WR 102, are located in our Galaxy (Van der Hucht *et al.* 1981). According to Barlow and Hummer (1982), the WO stars should be considered as a single sequence that represents the final evolutionary stage of the most massive stars: the final core helium or carbon burning stage.

*E-mail: gos@fsao.spb.su

1063-7737/02/2810-0701$22.00

Since the carbon-burning duration for massive stars is 0.3–1% of the helium-burning duration (Maeder and Meynet 1989), the number of WO stars cannot exceed 1% of the total number of WR stars; i.e., the six known WO stars in the Local Group galaxies form a representative sample. Therefore, studying each of them is of importance in understanding the physics of massive stars and the interaction of stars with the interstellar medium. Moreover, only two of the six known WO stars are associated with bright nebulae; one of these two stars is WR 102 in the nebula G2.4+1.4.

The WO stars are characterized by high-velocity winds, $V \simeq 4500$–7400 km s^{-1} (Barlow and Hummer 1982; Torres *et al.* 1986; Dopita *et al.* 1990; Polcaro *et al.* 1992), and high effective temperatures, 100 000 K (Maeder and Meynet 1989; Dopita *et al.* 1990; Melnick and Heydari-Malayeri 1991).

Optical, infrared, and radio observations of the WR 102 field revealed numerous traces of the action of ionizing radiation and strong stellar wind on the ambient gas.

Images of the nebula G2.4+1.4 in optical lines (Dopita and Lozinskaya 1990; Treffers and Chu 1991) and in radio continuum (Goss and Lozinskaya 1995) clearly reveal a diffuse H II region ionized by the radiation from WR 102 and a thin-filament shell swept up by the wind in this region.

Faint optical filaments were detected far beyond the previously known bright nebula through detailed kinematic studies of the nebula (Dopita and Lozinskaya 1990). The thin-filament shell was shown to be a bubble blown out by the wind at the boundary of a dense cloud. The expansion velocity of the approaching side of the shell is 42 km s^{-1}; no systematic expansion of the far side of the nebula was found. The dense cloud the interaction with which prevents the expansion of the far side of the shell was detected by the radiation of hot dust with a temperature of 30–31 K (Goss and Lozinskaya 1995).

The neutral component of the interstellar medium in the vicinity of WR 102 and the nebula G2.4+1.4 has not yet been studied in 21-cm line emission. Here, we present our 21-cm line observations of an extended region toward WR 102 and G2.4+1.4 in an effort to analyze the H I distribution and kinematics.

INSTRUMENTATION AND TECHNIQUES

To investigate the H I distribution in extended fields around WR 102 and G2.4+1.4, we obtained three drift curves in right ascension at declinations $-26\overset{\circ}{.}8$, $-26\overset{\circ}{.}2$ (the nebula center), and $-25\overset{\circ}{.}6$. The RATAN-600 antenna (Esepkina *et al.* 1979) has an angular resolution of $2.4' \times 50'$ and an effective area of $\sim$900 m^2 at these declinations. An uncooled HEMT amplifier was used at the input (Il'in *et al.* 1997). The system noise temperature was $\sim$70 K, the 39-channel filter spectrum analyzer had a channel bandwidth of 30 kHz (6.3 km s^{-1}), and the separation between channels was 30 kHz (Venger *et al.* 1982). An IBM PC was used for the system control, data acquisition, and preprocessing (Alferova *et al.* 1986).

The drift curve at each declination consisted of two series of three observations (five observations at declination $-26\overset{\circ}{.}2$) each obtained by shifting the receiver tuning frequency by half the channel bandwidth. As a result, each drift curve had 78 spectral channels that followed at 3.15 km s^{-1} intervals in the $\pm$120 km s^{-1} survey band. Independent observations at adjacent radial velocities also allowed the interference to be effectively removed. The antenna-temperature fluctuation rms in spectral channels after averaging the observations over the series was 0.2 K. The antenna and equipment parameters were checked in each series of observations by measuring a set of reference sources (Venger *et al.* 1981).

Subsequently, we subtracted an extended background from the drift curves in each spectral channel by using an upper spatial frequency Fourier filtering code. The Fourier filter passed spatial periods shorter than 192^s ($43'$) virtually without changes and reduced the power of spatial harmonics with periods longer than this boundary by approximately two orders of magnitude. It should be noted that a frequent subtraction of the background component results in underestimation of the brightness and angular size of the remaining small-scale features, because none of the background subtraction methods locates the zero line of the resulting drift curve. In order to take a certain zero line of the drift curves for the subsequent data reduction, we have to rely on a particular model for the cloud structure of the interstellar medium in advance. Since we commonly assume a negative antenna temperature of the line signal (absorption or self-absorption) to be encountered only in a few special cases (see below), it would be reasonable to draw the low-frequency zero line at the lower level of the small-scale antenna-temperature distribution for the H I emission line. The background component of the drift curves subtracted by the above method probably includes the following: (1) large-scale features of the interstellar-gas distribution, such as spiral arms or giant H I complexes; (2) emission from the intercloud medium, if present; (3) small-angular-size features unresolved by the RATAN-600 beam; and (4) a spurious large-scale background produced by far side lobes and the RATAN-600 stray field.

The parameters of H I features were determined in each channel by using a code for Gaussian analysis. In our case, depending on the amplitude threshold

set by the user, this code also separated extended structures into individual Gaussian features. In general, the assumption that the emission from individual clouds is Gaussian in shape appears arbitrary and this should be taken into account when interpreting the results. Next, we established a relationship between H I emission features at adjacent radial velocities and declinations to determine the three-dimensional structure of each H I cloud. Note that a significant subjective factor can also be introduced into this procedure. Therefore, we try to show most of the data in the figures in order that the reliability of identifying particular structures could be estimated.

The measured parameters have the following errors. The radial velocity of an isolated medium-brightness H I feature is measured with an accuracy of at least ± 1 km s^{-1} (in several cases, the accuracy is slightly lower because of the difficulties in separating the object from the background or from neighboring features). The measurement error of the H I line brightness temperature is ± 0.5 K, including the antenna calibration errors. The estimation error of the angular sizes in right ascension is $\pm 0.1°$. In declination, the antenna resolution is much lower and, accordingly, the angular sizes are measured with a lower accuracy.

RESULTS

Continuum and the H I Line

The continuum drift curve of the object is shown in Fig. 1. In contrast to the spectral channels, the Galactic-gas emission background in the 10-MHz-wide continuum channel was drawn by spline interpolation. The following observed parameters of the radio source were obtained:

Right ascension of the brightness peak (1950.0)	$17^h42^m40^s$
Peak antenna temperature	0.23 ± 0.01 K
Half-width of the drift curve	$8'.0 \pm 1.0$
Total flux density at 1.42 GHz	2.65 ± 0.2 Jy

Note that the coordinate and flux density of the source are closely similar to those obtained with the VLA by Goss and Lozinskaya (1995) at a close frequency of 1.49 GHz. The angular size is smaller, because this is the half-width of the brightness distribution integrated over the vertical RATAN-600 beam.

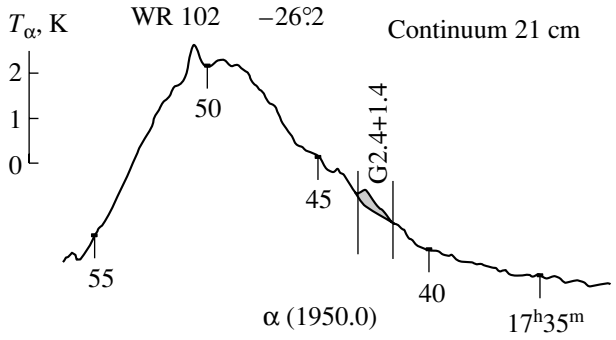

Fig. 1. The continuum drift curve for the G2.4+1.4 region at declination −26°2.

The distribution of H I features after the subtraction of the background radio-line emission is shown in Fig. 2. In this figure, no zero lines of the drift curves are shown (see above for discussion), the radial velocities relative to the local standard of rest are shown on the right, and their range is slightly reduced to save space. The vertical lines in this and succeeding figures drawn at right ascensions 17^h42^m and 17^h43^m correspond to the nebula size at zero radio brightness. The H I features nearest the nebula are hatched.

The Absorption Line and Self-absorption

Before we discuss the possible association of H I clouds with the nebula, we must solve two important problems. First, the object lies near the Galactic center, where the gas column density is high and the differential Galactic rotation is virtually negligible. Second, the well-known self-absorbing H I cloud (see, e.g., Riegel and Crutcher 1972), $30° \times 15°$ in size, is located here at a distance of about 900 pc from the Sun. These factors may lead to features that can be attributed to the absorption line, despite the comparatively low antenna temperature of the source in continuum.

The relative self-absorption is demonstrated by Fig. 3. It shows three H I line profiles that we obtained at the Galactic latitude of the object on three drift curves in right ascension. The interpolated parts of the profiles subjected to self-absorption whose maximum is observed in this region at radial velocities $V(\mathrm{LSR}) = 6–7$ km s^{-1} are hatched. The signal in absorption can be distinguished at the source position in Fig. 4, where the drift curves are shown on a large scale at radial velocities near zero (± 20 km s^{-1}). To reduce noise fluctuations, the drift curves were smoothed over 30^s intervals, which roughly corresponds to the source half-width in continuum. This yielded a fluctuation rms in the spectral channels of 0.1 K (i.e., no more than half the peak antenna temperature of the source in the continuum). In addition,

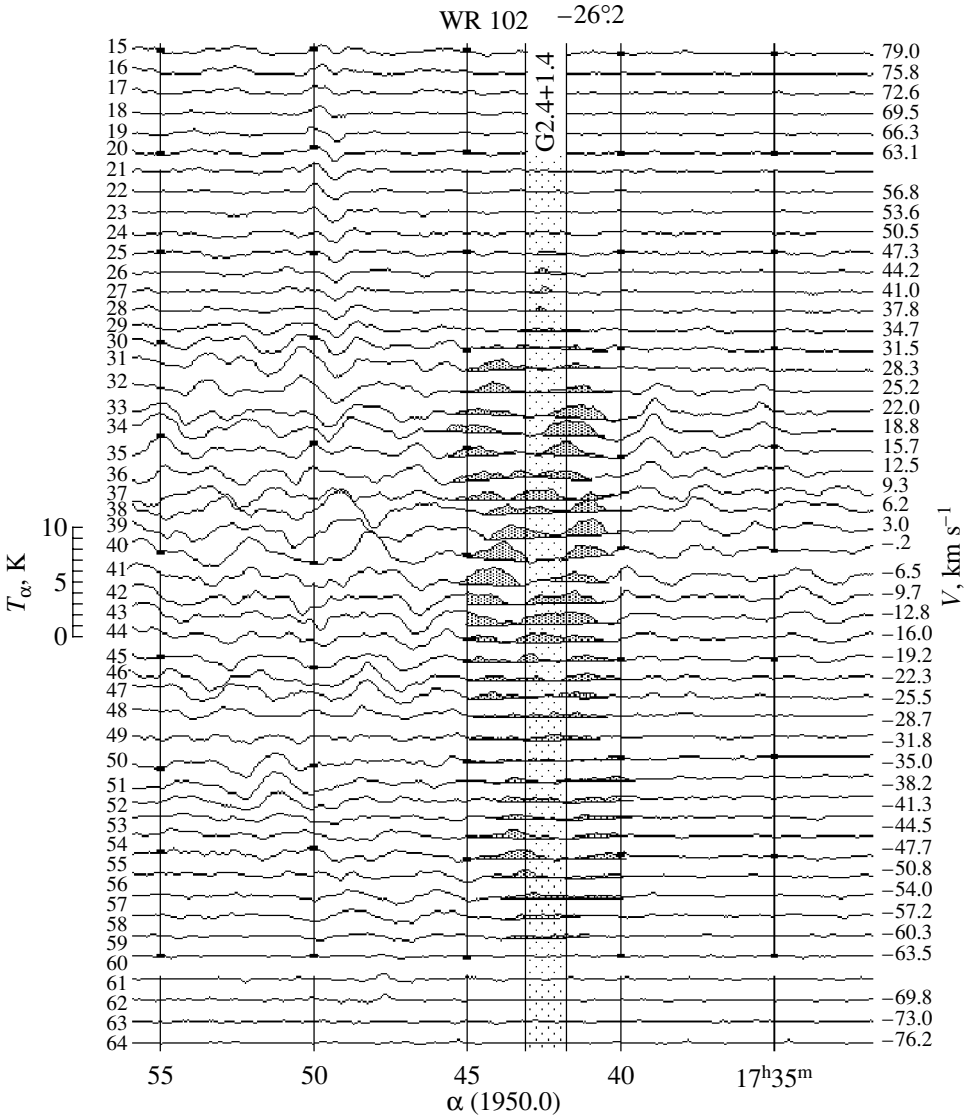

Fig. 2. The drift curves for H I features in the G2.4+1.4 region after the H I background subtraction. No zero lines are shown. Radial velocities relative to the local standard of rest and spectrometer channel numbers are along the right and left vertical axes, respectively. The H I features that may be associated with the observed nebula are hatched.

since one might expect an H I signal of any sign, median zero lines are drawn in the figure. The features with negative antenna temperatures near the source are hatched.

We see from Fig. 4 that there are no signals with negative antenna temperatures at the expected radial velocities at the source position. At the same time, those signals that are marked in the figure cannot correspond to the absorption line, because they do not coincide with the source in coordinates and almost all of them have a depth much larger than its antenna temperature and, in addition, change their positions, depending on radial velocity. Therefore, this kind of structure is attributable not to the absorption line but to an inhomogeneous H I emission background (cloud structure) (accordingly, drawing a median zero line is not appropriate in this case). Background inhomogeneities, which are clearly seen in Fig. 2, "blur" the weaker absorption line from the source. Obviously, it will be impossible to distinguish this line even if the equipment sensitivity is increased significantly.

H I Features Near the Nebula G2.4+1.4

We see from Fig. 2 that the H I clouds immediately adjacent to the nebula G2.4+1.4 are observed over a wide range of radial velocities, from −60 to +50 km s^{-1}. In the range of zero radial velocities (about ±15 km s^{-1}), the large number of background features and their complex shape in the

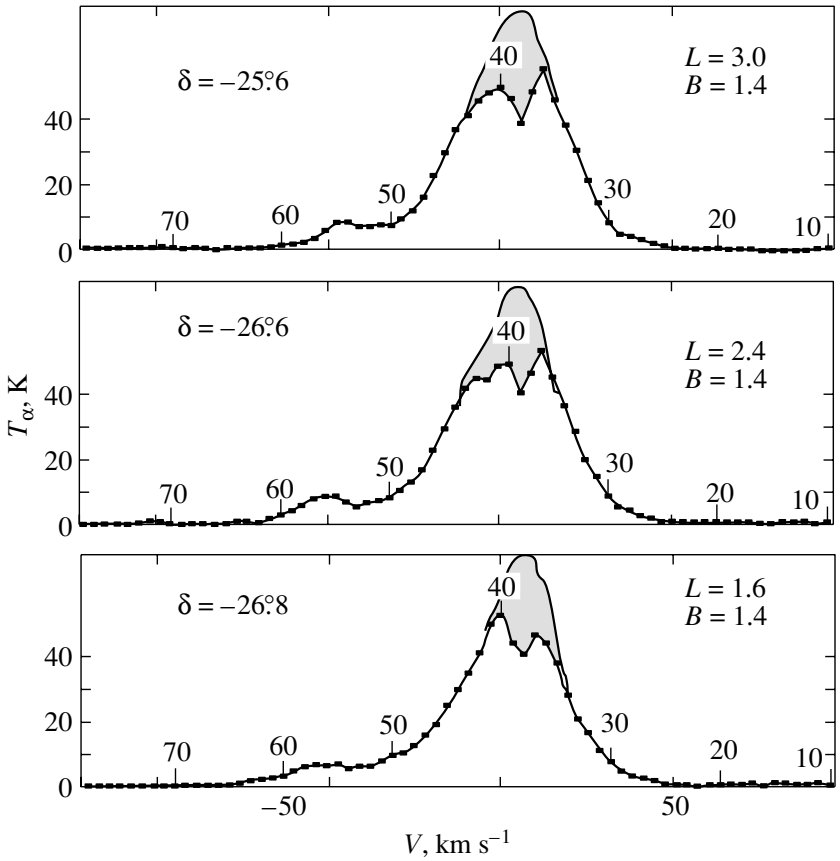

Fig. 3. H I line emission profiles in the G2.4+1.4 region. The parts of the profiles distorted by a self-absorbing H I cloud are hatched.

right ascension–radial velocity plane complicate the identification. To clarify the picture, we performed a Gaussian analysis of the observed drift curves, whose results are shown in Fig. 5. Note that in this procedure, we took a comparatively low threshold for the identification of Gaussian-shaped structures, 0.25 K (i.e., 1σ fluctuations of the spectral drift curves); thus a significant number of noise features are noticeable at high negative and positive radial velocities. Nevertheless, the H I features of significant brightness hatched in the figure reveal a distinct closed structure which may represent an expanding H I shell (provided that it also coincides with the nebula in declination). The latter can be demonstrated in the ranges of radial velocities +15 to +50 km s^{-1} and −15 to −60 km s^{-1}, where there are few background features and the putative shell is identified more clearly.

Figures 6 and 7 show the distribution of H I features in the above ranges of radial velocities on three drift curves in declination. Despite the large vertical RATAN-600 beam, the following conclusions can be drawn from these figures: first, the apparent arc-shaped structures are not displaced in right ascension with changing declination, which would be natural for background Galactic gas structures, and, second, their angular size in right ascension is at a maximum at declination −26.2°, i.e., for the drift curve passing through the center of the optical nebula. Consequently, we may assume with reasonable confidence that the H I ring structure marked in Fig. 5 is actually the expanding shell that immediately surrounds the nebula G2.4+1.4.

It should be emphasized that this assumption undoubtedly requires further confirmation. In particular, high-resolution observations with a circular beam are needed. Indeed, a bright H I feature is observed at the center of our identified shell directly toward the nebula in the velocity range +20 to −13 km s^{-1} (even up to −30 km s^{-1}, but it is fainter here). This is most likely a feature of background gas. However, it may be physically associated with the star WR 102 and the nebula G2.4+1.4 or with an extended arc of dust, because the optical and infrared observations made by Dopita and Lozinskaya (1990) and Goss and Lozinskaya (1995) revealed a rather complex structure and kinematics of the ionized gas and dust near the star (see below). Observations with a circular beam may not give an unequivocal answer either, because we

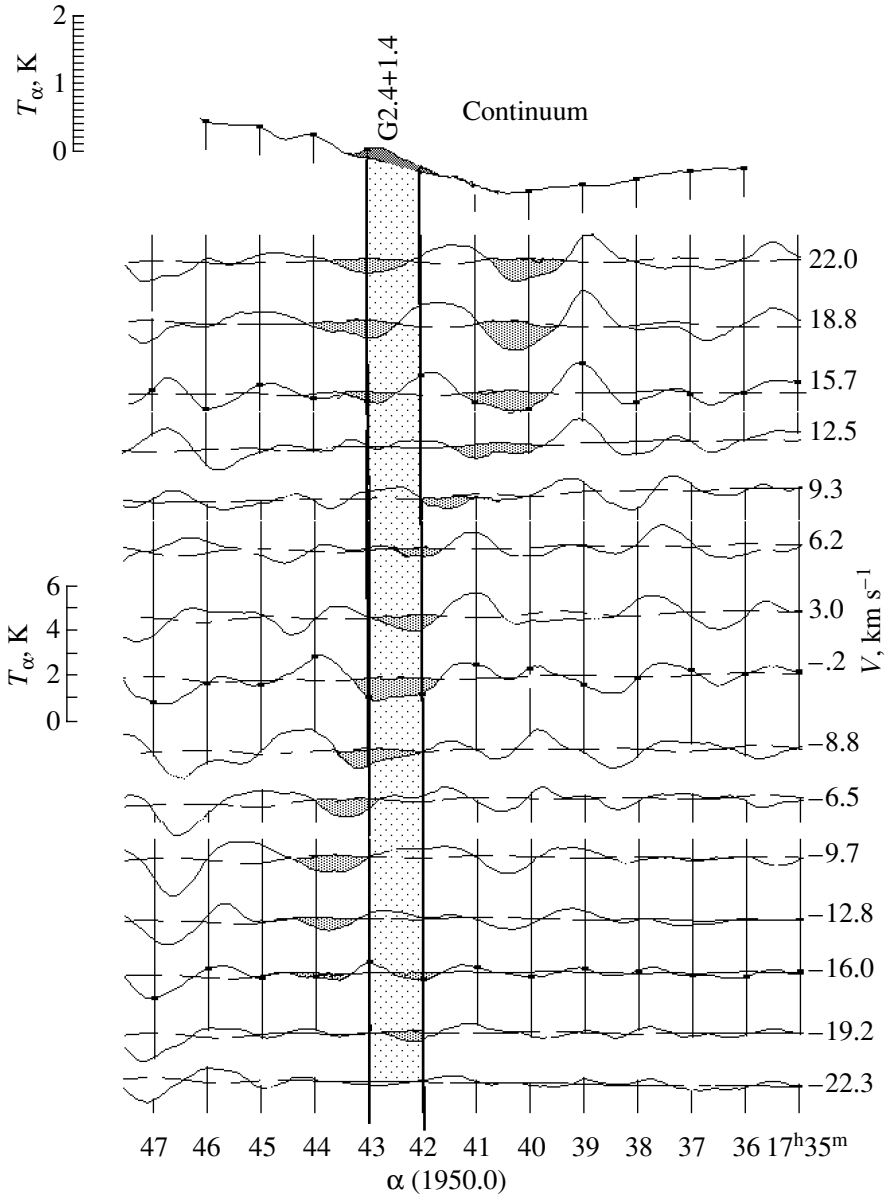

Fig. 4. Parts of the H I drift curves in the G2.4+1.4 region after the H I background subtraction. Zero lines were drawn halfway between the maxima and minima of the features. To reduce noise fluctuations, the curves were smoothed over 30^s intervals in α. The minima that may be associated with H I self-absorption or with the absorption of nebular emission are hatched.

see virtually the entire Galaxy in the 21-cm line at longitude $l = 2.4°$ and the kinematic distances here are uncertain.

Therefore, it should be borne in mind that we determined the parameters of the H I shell given below by assuming that all of the features highlighted in Fig. 5 represent a single expanding shell. In the next section, we also attempt to correlate the observed H I features with the various components of G2.4+1.4 using optical and infrared observations.

Parameters of the H I Shell

Even the mean radial velocity of the shell is difficult to determine. Formally, as the mean value between the most displaced features at positive and negative velocities, it falls within a region of nearly zero values.

Note that Caswell and Haynes (1987) determined the mean radial velocity of the ionized gas, 3 km s^{-1}, and the half-width of internal motions, −53 km s^{-1}, from observations of the H109α and H110α recombination lines in the nebula G2.4+1.4. These data are in good agreement with the observed parameters of the H I shell if it is assumed to immediately surround the nebula.

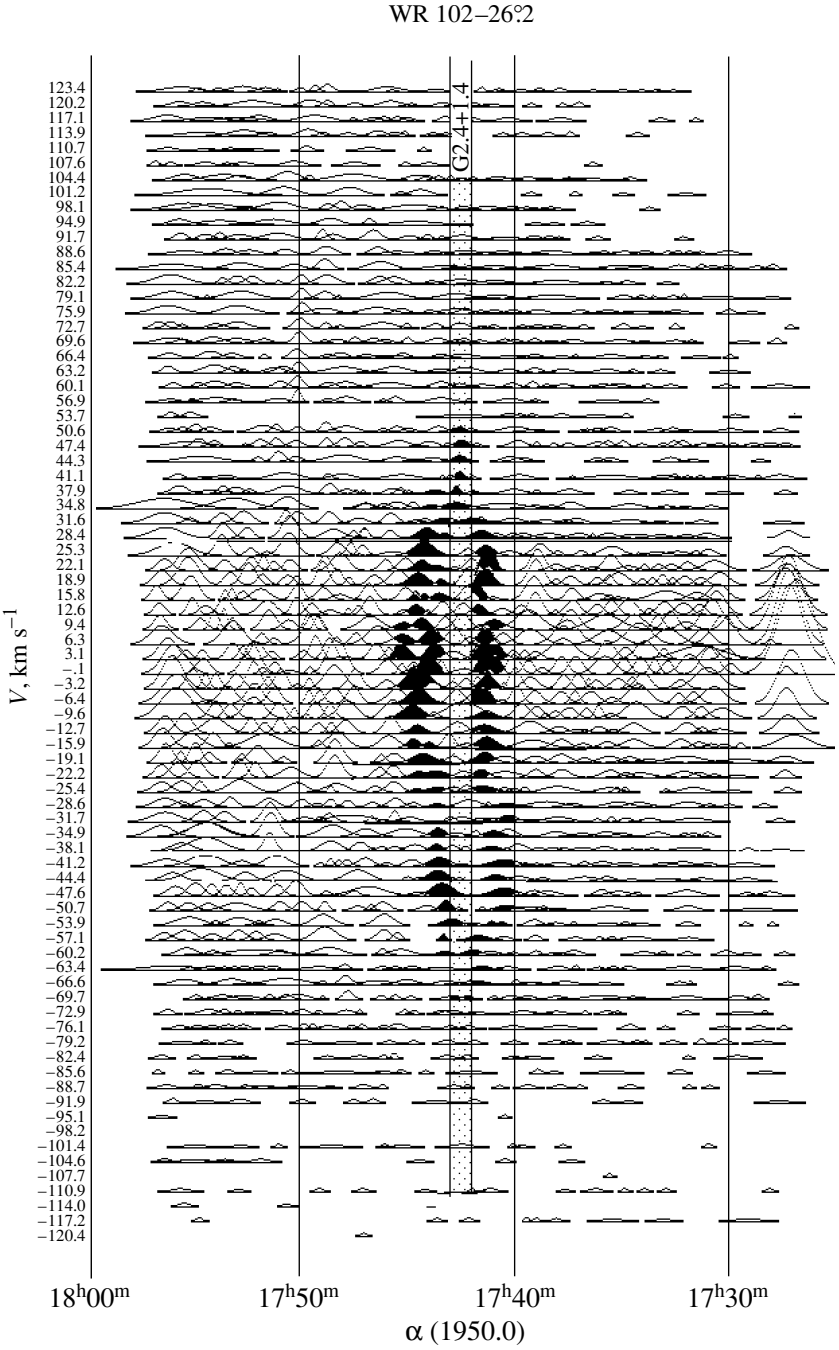

Fig. 5. The drift curves of H I features in the G2.4+1.4 region after a Gaussian analysis of the features whose emission is shown in Fig. 2. The H I features that probably form a single expanding shell around the nebula are hatched.

Optical-line observations revealed bright features in the range of velocities V(LSR) from -20 to $+25$ km s^{-1} (Treffers and Chu 1982; see also references to previous papers therein). Dopita and Lozinskaya (1990) identified the main "nonaccelerated" component of the ionized gas in the nebula at V(LSR) $= +23$ km s^{-1} and the approaching side of the expanding shell whose velocities vary over the range $+15$ to -28 km s^{-1}.

Thus, the velocities of the H I features that we treat here as a manifestation of a single expanding shell around the nebula G2.4+1.4 are generally in agreement with the radio and optical line observations.

We determined the parameters of the H I shell around the H II region G2.4+1.4 after performing a

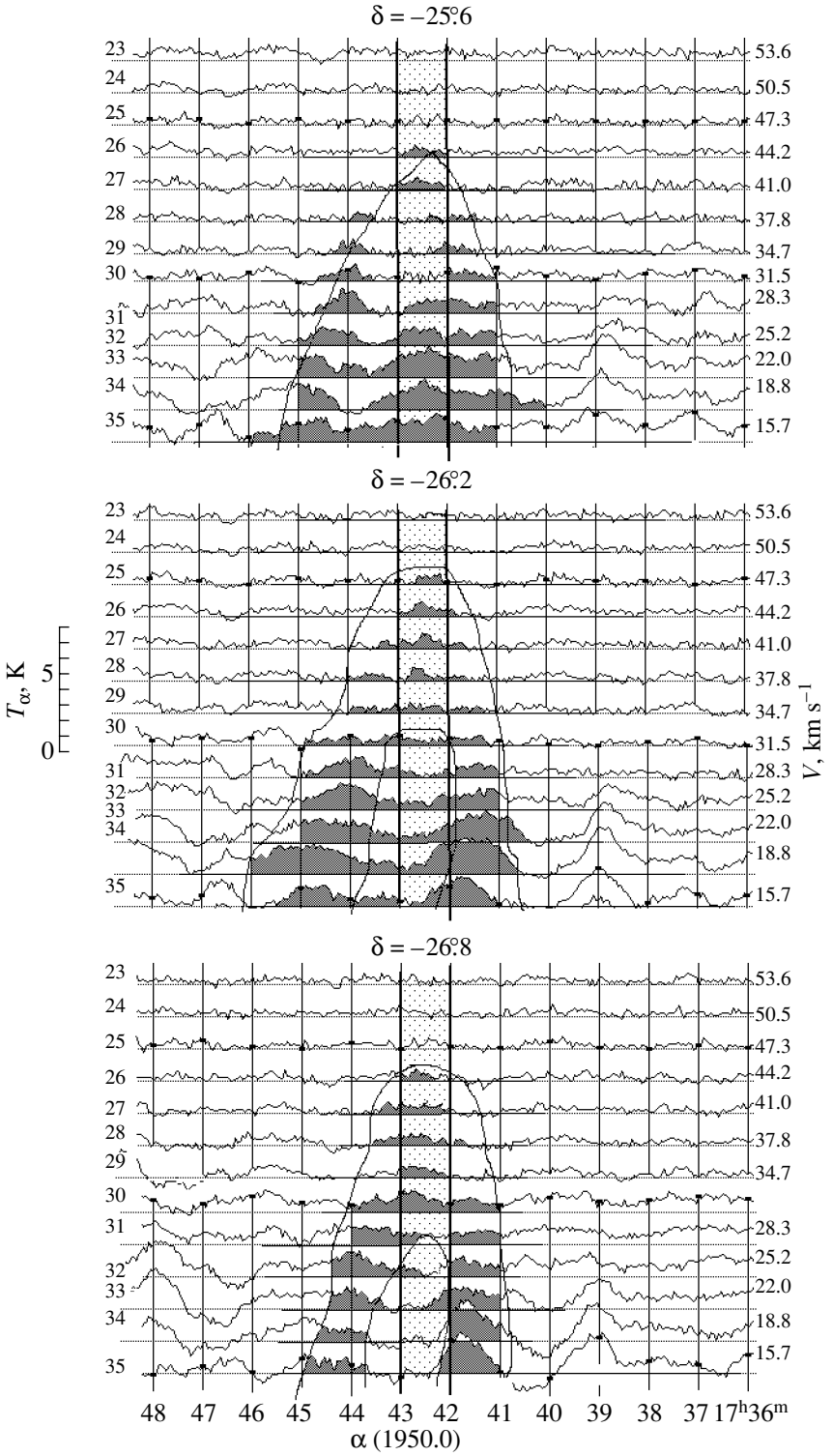

Fig. 6. Part of the putative H I shell at positive radial velocities at three declinations around G2.4+1.4. The positions of the H I features in α at different declinations are not displaced, and the angular size in α is largest at the nebula declination.

Gaussian analysis of the features that were directly obtained from observations. As we mentioned above, our code for Gaussian analysis not only determined the parameters of features but also broke down complex features into individual Gaussians. Some of the data given below differ from their preliminary values calculated from the original observational data

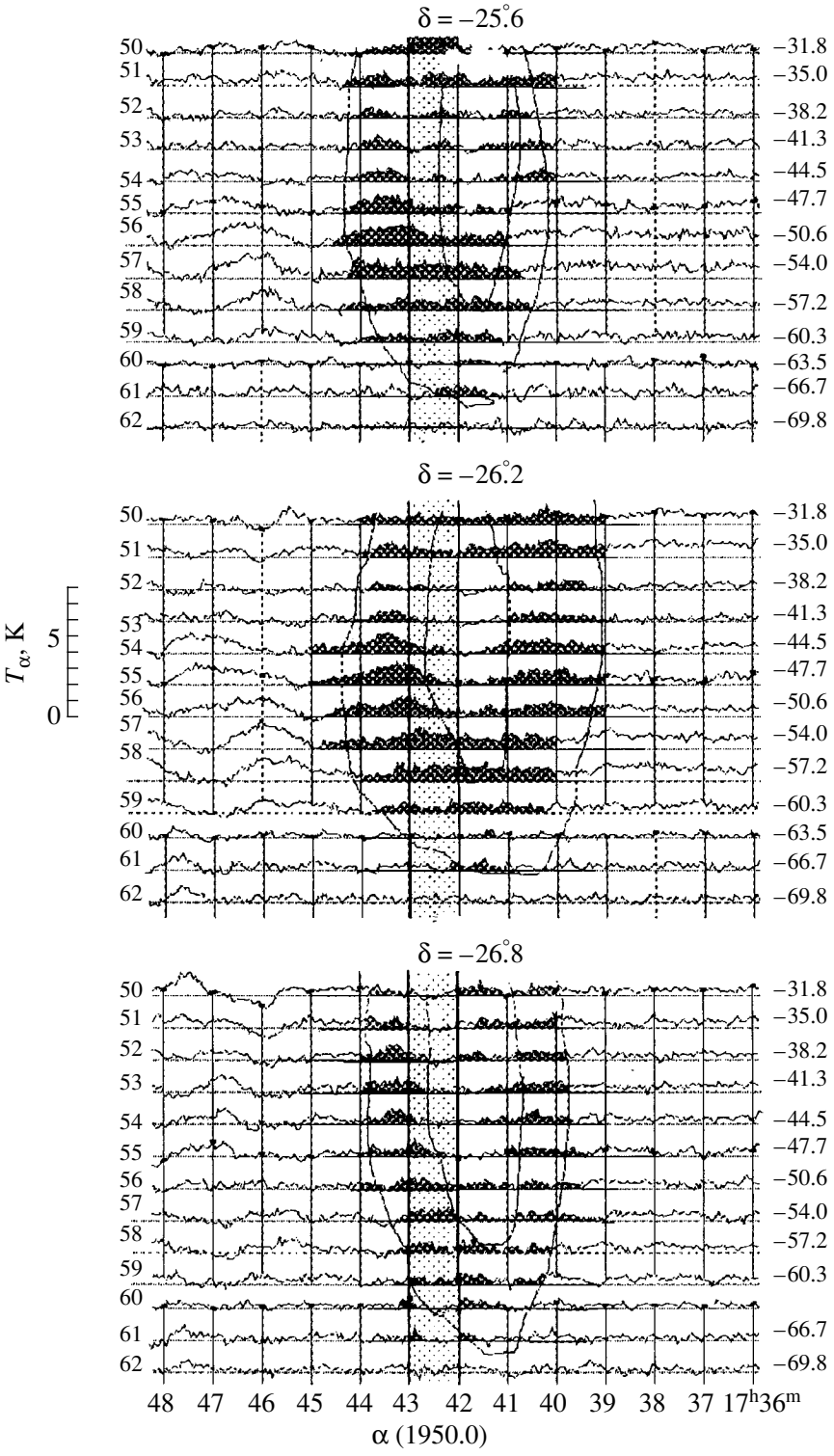

Fig. 7. Same as Fig. 6 for negative radial velocities. The behavior of the features with changing declination is the same as that in Fig. 6.

(Fig. 2) and presented in Gosachinskij and Lozinskaya (2001).

Here, the observed parameters of the H I shell around G2.4+1.4 were determined from the features marked in Fig. 5 by assuming that the shell has a circular symmetry in the plane of the sky.

Coordinates of the center	$\alpha\,(1950) = 17^{h}42^{m}30^{s}$ $\delta\,(1950) = -26\overset{\circ}{.}2$
Angular diameter: outer inner	 $1\overset{\circ}{.}1$ $0\overset{\circ}{.}7$
Mean shell thickness	$\approx 0\overset{\circ}{.}2$
Peak line brightness temperature	5.0 ± 0.5 K
Mean Radial velocity	$V(\mathrm{LSR}) = -5 \pm 5$ km s^{-1}
Radial-velocity range	$\Delta V \approx 100$ km s^{-1}

DISCUSSION

The distance to the shell, if it actually surrounds the WO star and the nebula G2.4+1.4, may be taken to be equal to the photometric distance to WR 102 determined by Dopita and Lozinskaya (1990): $d = 3 \pm 1$ kpc.

Assuming a uniform gas density distribution within the shell, we obtain the following parameters of the H I shell at a distance of 3 kpc

Maximum expansion velocity	≈ 50 km s^{-1}
Outer diameter	56 pc
Inner diameter	37 pc
H I density	≈ 2.7 cm^{-3}
H I shell mass	$4.2 \times 10^3\ M_\odot$

We find the ambient gas density in the region under the common assumption that the entire gas of the shell was initially uniformly distributed over its observed volume: $n_0 = 1.85$ cm^{-3}.

According to the optical studies by Dopita and Lozinskaya (1990), the swept-up shell is a bubble blown out by the wind from the star located at the boundary of a dense cloud facing the observer: the density inside and outside the cloud is $n_0 \simeq 60$ cm^{-3} and $n_0 \simeq 3$–4 cm^{-3}, respectively. As we see, the H I density is close to the gas density outside the cloud inferred from optical observations. This is quite natural if the dense cloud is comparable in size to the nebula, because our derived H I density was averaged over the large (in height) RATAN-600 beam.

The H I structure marked in Fig. 5 is not a perfect ring. We can interpret the H I structures observed in the coordinate–velocity plane in more detail and can attempt to compare them with the results of optical and infrared studies.

Three barrel-shaped groups of bright H I features, each showing evidence of an expanding shell structure, can be distinguished at declination $-26\overset{\circ}{.}2$:

I—the central velocity $V(\mathrm{LSR}) = 15.2$–18 km s^{-1}; the velocity range is $V(\mathrm{LSR}) = 6.3$–9.4 km s^{-1} to $V(\mathrm{LSR}) = 35$–44 km s^{-1};

II—the central velocity $V(\mathrm{LSR}) = -3 \ldots -9$ km s^{-1}; the velocity range is $V(\mathrm{LSR}) = 6.3$–9.4 km s^{-1} to $V(\mathrm{LSR}) = -20 \ldots -28$ km s^{-1};

III—the central velocity $V(\mathrm{LSR}) = -45 \ldots -47$ km s^{-1}; the velocity range is -28 to -57 km s^{-1}.

Most of the features distinguished on the drift curves in the coordinate–velocity plane may be assumed (with all of the above reservations) to be associated with G2.4+1.4 and WR 102. Indeed, previous 21-cm line observations for a large number of WR stars (see Introduction) showed that most WR stars are associated with cavities or shells of neutral gas revealing complex (clumpy) structures and kinematics.

As for the object under study, optical, radio, and infrared observations suggest a nonuniform distribution of ionized gas and dust in extended regions around the star WR 102. Detailed optical (Dopita and Lozinskaya 1990; Treffers and Chu 1991) and radio (Goss and Lozinskaya 1995) studies of the structure and kinematics of G2.4+1.4 clearly reveal a diffuse H II region ionized by the star WR 102 and a thin-filament shell in this region swept up by the wind. The size of the H II region at the $ME = 300$ level is $16'$ (14 pc); the shell size is $10'$ (10 pc). The expansion velocity of the approaching side of the shell is 42 km s^{-1}, with the far side showing no systematic expansion.

Such kinematics of the optical nebula suggests that there must be a dense cloud collision with which slowed down the expansion of the receding side of the shell. This cloud of hot dust was detected by Goss and Lozinskaya (1995) through the reduction of archival IRAS data. The morphology of the bright infrared source follows the shape of the thermal radio source and the bright part of the nebula. A map of the distribution of the dust temperature determined from the IRAS (60)/(100) flux ratio indicates that the highest dust temperature in the large region is observed in this bright source, suggesting that the star WR 102 is physically associated with the dense cloud. A large-scale map of the infrared brightness distribution also reveals an extended lagoon surrounded by a weak shell structure in the west [see Fig. 6 from Goss and Lozinskaya (1995)]. The lagoon size is about $30'$; WR 102 and its optical/radio/infrared nebula are located at the northwestern boundary of the lagoon, on the spur bounding it.

Given the above optical and infrared observations, the identified structures in the H I distribution can be interpreted as follows.

Group I of H I features at $V(\mathrm{LSR}) = 15.2$–18 km s^{-1} may represent mainly the nonaccelerated neutral gas in the region. Since the star lies at the forefront of the dense cloud, the difference from the velocity of the wind-nonaccelerated ionized gas in

G2.4+1.4 [$V(\mathrm{LSR}) = 23 \pm 5$ km s^{-1}]), as inferred by Dopita and Lozinskaya (1990), can be explained by expansion of the H II region into the cloud at the speed of sound.

Group II of H I features at $V(\mathrm{LSR}) = -3 \ldots -9$ km s^{-1} may be correlated with bright filaments of the swept-up ionized shell [according to Dopita and Lozinskaya (1990), the mean velocity of the brightest optical filaments on the approaching side of the shell is -5 km s^{-1}]. If we make the common assumption that the ambient gas has a two-component structure (dense cores in a less dense diffuse medium), then we can naturally explain the presence of bright, weakly accelerated ionized filaments and dense H I cloudlets at similar velocities that we combined into structure II and those features that are observed as separate clouds in projection onto G2.4+1.4 at velocities from +25 to -30 km s^{-1} (see Fig. 5). The latter can also be associated with the neutral gas in the dust arc mentioned above, which is projected onto the nebula in the coordinate–velocity plane when observed with a knife-edge beam.

The velocities of our identified H I structure III (the central velocity is $V(\mathrm{LSR}) = -45 \ldots -47$ km s^{-1}) closely match the highest negative velocities of faint optical filaments on the approaching side of the shell swept up by the wind.

Of course, a detailed comparison of this kind requires 21-cm line observations with a circular diagram. For now, we can only conclude that the observed H I features at all of the mentioned velocities can be naturally explained in terms of the model of a bubble at the boundary of a dense cloud (Dopita and Lozinskaya 1990) and, accordingly, can be combined into a single H I shell surrounding the WO star and G2.4+1.4.

Using the standard relations for a cavity swept up by stellar wind that follow from the classical theory by Weaver *et al.* (1977),

$$R(t) = 66 n_0^{-1/5} L_{38}^{1/5} t_6^{3/5} \text{ pc},$$

$$v(t) = 39 n_0^{-1/5} L_{38}^{1/5} t_6^{-2/5} \text{ km s}^{-1}$$

(here, R is the radius of the shell, v is its expansion velocity, t_6 is its age in Myr, and L_{38} is the stellar-wind mechanical luminosity in units of 10^{38} erg s^{-1}), we find the required stellar-wind mechanical luminosity and the shell age:

$$L_w = 0.8 \times 10^{38} \text{ erg s}^{-1}, \quad t = 3.4 \times 10^5 \text{ yr}.$$

The required stellar-wind mechanical luminosity derived from the parameters of the H I shell is lower than the WO wind mechanical luminosity inferred by Dopita *et al.* (1990) and Dopita and Lozinskaya (1990) from the observations of WR 102: $L_w = 2 \times 10^{38}$ erg s^{-1} at the wind velocity $V_w = 5500$ km s^{-1}.

At the same time, our derived kinematic age of the H I shell, $t = 3.4 \times 10^5$ yr, is an order of magnitude longer than the duration of the WO stage (the spectrum of WR 102 and its position in the Hertzsprung–Russell diagram suggest a stage close to the bare CO core of a high-mass main-sequence star: $M_{\mathrm{init}} = 40$–$60 M_\odot$ (Dopita *et al.* 1990). This indicates that the wind from the star at the preceding WN and WC stages also determines the structure of the surrounding H I shell.

According to our data, the total kinetic energy of the H I shell determined by its mass and velocity is $E_{\mathrm{kin}} \simeq 1.3 \times 10^{50}$ erg. This value is much lower than the total mechanical energy supplied by the wind from the central star over the shell lifetime even if it is considered that the mechanical luminosity of the wind from the WR star at the WN and WC stages can be a factor of 4 or 5 lower than that at the final WO stage.

Note also that there is every reason to expect that the structure and kinematics of the ambient neutral gas are determined by the action of the WO star and its progenitor at all stages, including the main-sequence stage.

CONCLUSIONS

We have presented the RATAN-600 21-cm line observations of the fields around the star WR 102 and the associated nebula G2.4+1.4. The neutral component of the interstellar medium near WR 102 has not been studied previously in 21-cm line emission.

We identified H I features in the right ascension–radial velocity plane which form a ring structure of neutral hydrogen immediately surrounding the nebula G2.4+1.4. We argue that this structure can represent an extended expanding shell of neutral gas around the WO star.

The identified H I shell has an irregular structure. Its outer and inner diameters are 1°.1 or 56 pc and 0°.7 or 37 pc, respectively, for the assumed photometric distance to the star of 3 kpc.

Based on the idealized model of a spherically symmetric shell of uniform density, we determined the mean H I density in the shell, ≈ 2.7 cm^{-3}, and the total H I mass, $4.2 \times 10^3 M_\odot$. If the entire gas of the shell is initially uniformly distributed over its observed volume, then the mean ambient gas density in the region is $n_0 = 1.85$ cm^{-3}.

The H I features that we treat as a single shell structure are observed over a wide range of radial velocities: $\Delta V \approx 100$ km s^{-1}; the mean radial velocity

is $V(\mathrm{LSR}) = -5 \pm 5$ km s^{-1}; the maximum shell expansion velocity reaches $\approx$50 km s^{-1}.

It should be emphasized that the assumption that the H I features form a single structure representing an expanding shell undoubtedly requires further confirmation. High-resolution observations with a circular beam are primarily needed. Nevertheless, comparison of the results of our 21-cm line observations with the structure and kinematics of the ionized nebula G2.4+1.4 inferred from the optical observations of Dopita and Lozinskaya (1990) and with the dust distribution in the region inferred from the data of Goss and Lozinskaya (1995) suggests that the derived parameters of the H I shell are consistent with the model of a bubble blown out by the wind from a WO star at the boundary of a dense cloud adopted in these studies.

Based on the standard theory for the interaction of a strong stellar wind with the interstellar medium, we estimated the mechanical luminosity of the stellar wind required for the observed H I shell to be formed, $L_w \sim 0.8 \times 10^{38}$ erg s^{-1}, and the shell age, $t = 3.4 \times 10^5$ yr. Similar mechanical luminosity and duration of the stellar wind were obtained by Dopita and Lozinskaya (1990) through a detailed analysis of the structure and kinematics of the thin-filament optical nebula G2.4+1.4. Spectroscopic observations of the central star (Dopita *et al.* 1990) suggest that mass loss at the WR and WO stages provides such a wind mechanical luminosity. Thus, comprehensive optical, infrared, radio-continuum, and 21-cm line observations of the WR 102 field revealed numerous traces of the action of ionizing radiation and strong WO stellar wind on the ambient gas.

ACKNOWLEDGMENTS

We wish to thank G.N. Il'in, Z.A. Alferova, and T.V. Monastyreva from the Special Astrophysical Observatory for maintaining the equipment in an operational state and for help in the observations. This work was supported by the Russian Foundation for Basic Research (project nos. 01-02-17154 and 01-02-16118).

REFERENCES

1. Z. A. Alferova, I. V. Gosachinskij, S. R. Zhelenkov, and A. S. Morozov, Izv. SAO **23**, 89 (1986).
2. E. M. Arnal, Astron. Astrophys. **254**, 305 (1992).
3. E. M. Arnal, Astron. J. **121**, 413 (2001).
4. E. M. Arnal and I. F. Mirabel, Astron. Astrophys. **250**, 171 (1991).
5. E. M. Arnal, C. E. Cappa, J. R. Rizzo, and S. Cichowolski, Astron. J. **118**, 1798 (1999).
6. M. J. Barlow and D. C. Hummer, in *Proceedings of the IAU Symposium No. 99 "Wolf-Rayet Stars: Observations, Physics, Evolution," Cozumel, Mexico, 1981,* Ed. by C. W. H. de Loore and A. J. Willis (D. Reidel, Dordrecht, 1982), p. 387.
7. C. Cappa de Nicolau and V. S. Niemela, Astron. J. **89**, 1398 (1984).
8. J. L. Caswell and R. F. Haynes, Astron. Astrophys. **171**, 261 (1987).
9. M. Dopita and T. A. Lozinskaya, Astrophys. J. **359**, 419 (1990).
10. M. A. Dopita, T. A. Lozinskaya, P. J. McGregor, and S. J. Rawlings, Astrophys. J. **351**, 563 (1990).
11. N. A. Esepkina, N. S. Bakhvalov, B. A. Vasil'ev, *et al.*, Izv. SAO **11**, 182 (1979).
12. S. Gervais and N. St-Louis, Astron. J. **118**, 2394 (1999).
13. I. V. Gosachinskij and T. A. Lozinskaya, in *Proceedings of the All-Russia Astronomical Conference* (Sankt-Peterb. Gos. Univ., St. Petersburg, 2001), p. 51.
14. W. M. Goss and T. A. Lozinskaya, Astrophys. J. **439**, 637 (1995).
15. K. A. van der Hucht, P. S. Conti, I. Lundstrom, and B. Stenholm, Space Sci. Rev **28**, 227 (1981).
16. G. N. Il'in, A. M. Pilipenko, and V. A. Prozorov, in *Proceedings of the XXVII Radio-astronomical Conference* (IPA RAN, St. Petersburg, 1997), p. 128.
17. T. A. Lozinskaya, V. V. Pravdikova, I. V. Gosachinskij, and S. A. Trushkin, Astron. Zh. **74**, 376 (1997) [Astron. Rep. **41**, 327 (1997)].
18. A. Maeder and G. Meynet, Astron. Astrophys. **210**, 155 (1989).
19. A. P. Marston, Astron. J. **109**, 2257 (1995).
20. J. Melnick and M. Heydari-Malayeri, in *Proceedings of the IAU Symposium No. 143 "Wolf-Rayet Statrs and Inerrelations with Other Massive Stars in Galaxies,* Ed. by K. A. van der Hucht and B. Hidayat (Kluwer, Dordrecht, 1991), p. 409.
21. J. Nichols-Bohlin and R. A. Fesen, Astron. J. **105**, 672 (1993).
22. S. Pineault, S. Gaumont-Guay, and B. Madore, Astron. J. **112**, 201 (1996).
23. V. F. Polcaro, R. Viotti, C. Rossi, and L. Norci, Astron. Astrophys. **265**, 563 (1992).
24. K. W. Riegel and R. M. Crutcher, Astron. Astrophys. **18**, 55 (1972).
25. A. V. Torres, P. S. Conti, and P. Massey, Astrophys. J. **300**, 379 (1986).
26. R. R. Treffers and Y.-H. Chu, Astrophys. J. **254**, 132 (1982).
27. R. R. Treffers and Y.-H. Chu, Astrophys. J. **366**, 181 (1991).
28. A. P. Venger, I. V. Gosachinskij, V. G. Grachev, and N. F. Ryzhkov, Izv. SAO **14**, 118 (1981).
29. A. P. Venger, V. G. Grachev, T. M. Egorova, *et al.*, Soobshch. SAO, No. 35, 5 (1982).
30. R. Weaver, R. McCray, J. Castor, P. Shapiro, and R. Moore, Astrophys. J. **218**, 377 (1977).

Translated by V. Astakhov

Astronomy Letters, Vol. 28, No. 10, 2002, pp. 713–720. Translated from Pis'ma v Astronomicheskiĭ Zhurnal, Vol. 28, No. 10, 2002, pp. 788–795.

An Acousto-Optical Imaging Spectrophotometer for Astrophysical Observations

V. Ya. Molchanov[1], V. M. Lyuty[2*], V. F. Esipov[2], S. P. Anikin[3], O. Yu. Makarov[3], and N. P. Solodovnikov[4]

[1] *Acousto-Optical Research Center, Moscow Institute of Steel and Alloys (Technological University), Leninskiĭ pr. 4, Moscow, 117936 Russia*

[2] *Sternberg Astronomical Institute, Universitetskiĭ pr. 13, Moscow, 119992 Russia*

[3] *Science and Technology Center for Acousto-Optics, Moscow Institute of Steel and Alloys (Technological University), Leninskiĭ pr. 4, Moscow, 117936 Russia*

[4] *Russian Technological Agency, Voronezh, Russia*

Received May 28, 2002

Abstract—We present the results of our tests of an acousto-optical imaging spectrophotometer with a CCD detector for astronomical observations. The tunable acousto-optical filter, based on a paratellurite single crystal with a 13 Å pass band operates in the wavelength range 6300–11 000 Å. We obtained image spectra for the planetary nebula NGC 7027 in the Hα line and for Saturn in the methane absorption band, as well as Hα and continuum images for the nuclear region of the Seyfert galaxy NGC 1068. © *2002 MAIK "Nauka/Interperiodica".*

Key words: *acousto-optical filter, imaging spectrophotometer, planetary nebulae, active galactic nuclei.*

INTRODUCTION

In the early 1970s, rapid variability of the Hα emission line was detected in the nucleus of the Seyfert galaxy NGC 4151 with a lag relative to continuum variability (Lyuty and Cherepashchuk 1971; Cherepashchuk and Lyuty 1973). This effect was interpreted as the photoionization of gas clouds located at some distance from the central source in the galactic nucleus by variable radiation from this source. The gas density and effective distance can be determined from the variability time scale and the lag time (light echo), respectively. After the detection of a similar effect, but with a smaller lag, in the C IV line (Ulrich *et al.* 1984) and after establishing that lines of different ionizations had different lags relative to continuum variability (Gaskell and Spark 1986), a new trend in the study of active galactic nuclei (AGNs) began to develop: echo mapping, i.e., obtaining the spatial distribution of various elements. The first observations were carried out with a wedge interference filter with a ~90 Å pass band in the spectral range 5600–7500 Å (Lyuty *et al.* 1973), i.e., in photometer mode. The subsequent observations are all spectroscopic. At present, CCD spectroscopic observations are comparable in accuracy to photometric observations and provide more information but they require much time on large telescopes. Therefore, long and complete series of observations are quite difficult to obtain.

Photometric observations with a wedge filter allow small telescopes to be used with a high measurement accuracy. However, the transmission of wedge interference filters is low. At the same time, conventional (nonwedge) interference filters are difficult to use in investigating emission-line variability in AGNs because of their redshift: each object requires its own set of filters.

In the late 1960s–early 1970s, a fundamentally new class of spectral devices was devised, electronically tunable acousto-optical filters (AOFs) (Chang 1976, 1981; Balakshii *et al.* 1985). In the mid-1970s, the first attempts were made to use tunable AOFs for astronomical spectroscopic observations: at the Harvard Observatory in 1976 (Wattson *et al.* 1976) and, subsequently, at the Royal Greenwich Observatory in 1984 (Bates *et al.* 1984a, 1984b). Conceptually and technologically, AOFs at that time were imperfect. As a result, a collinear filter based on a calcium molybdate crystal designed by the Harris company (USA) was used in the imaging spectrometer (Wattson *et al.* 1976). The filter had a

* E-mail: vmlyuty@sai.msu.ru

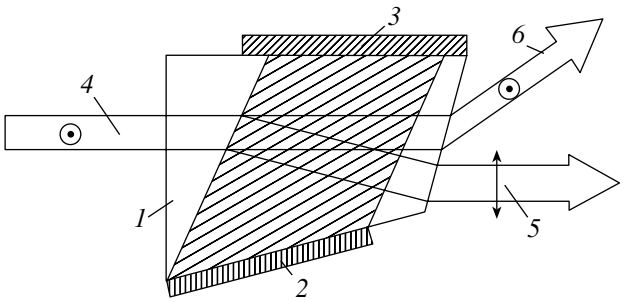

Fig. 1. The ray path in the AOF for linearly polarized incident light (see the text).

small optical aperture (4 × 4 mm) and a large crystal length (~50 mm). It was supplied with polarization elements at the entrance and at the exit. A cylindrical lens was used to compensate for astigmatism. To pass the image of an object through such a filter required a special optical system. These factors limited the angular and spatial resolutions of the system. Nevertheless, the authors gave several demonstrations of the spectrometer, in particular, they took a series of spectral photographs of Saturn's image in methane absorption bands in the wavelength range 8400–9400 Å and outside the bands. The image quality proved to be poor (see Fig. 2 in the cited paper).

The paratellurite-crystal-based filter used by Bates *et al.* (1984) was designed by the Matsushita company (Japan), but it also had a nonoptimal design. Apart from a small optical aperture (3 × 5 mm), it had a very small angular aperture (~0.4°), which made it impossible to filter high spatial harmonics. This device was unsuitable for obtaining optical image spectra, and the authors used it as a selective element of the spectrophotometer to observe the flare star AD Leo.

Smith *et al.* (1987) used a quartz-based AOF with a 12 × 4-mm aperture that operated in the wavelength range 2500–7200 Å. However, such a filter would be appropriate for use only in the ultraviolet, because it required a high control acoustic power in visible spectrum.

The first paper that showed a high quality of spectral acousto-optical instrumentation was published in 1991 (W. Smith and K. Smith 1991). AOFs of various designs were provided by NASA. The wide-angle noncollinear paratellurite filter with a large optical aperture (14 × 16 mm) and a high spatial (100 lines per mm) resolution was most promising among the filters. There are virtually no data on the parameters of this filter in the paper. Nevertheless, we can conclude that the authors of the publication had quite modern acousto-optical spectral devices. In the above paper, the authors explore the fundamental possibility of a polarimetric analysis of high-contrast images for objects by using an AOF and discuss in detail the peculiarities of AOFs compared to conventional interference filters. The authors concluded that the AOFs based on paratellurite single crystals surpass the interference filters in all respects except luminosity.

THE ACOUSTO-OPTICAL IMAGING SPECTROPHOTOMETER

In recent years, the efforts of researches have gone into creating a new class of AOFs designed for the spectral analysis of optical images. Several specific requirements are imposed on the filters for the spectral analysis of images: they must have a large angular field of view and be capable of efficiently filtering high spatial harmonics in images and of combining a high spatial resolution with a high spectral resolution (Voloshinov and Gupta 1999; Parygin *et al.* 2001; Molchanov *et al.* 2001). To study faint optical objects, the filter must have a high transmission.

The Acousto-Optical Tunable Filter

The Science and Technology Center for Acousto-Optics designed a unique AOF based on a noncollinear wide-angle interaction in a paratellurite single crystal optimized for astronomical observations (Molchanov *et al.* 2001). The principle of operation of the AOF is well known from the literature (Magdich and Molchanov 1989; Gottlieb 1994); it is based on light diffraction in an anisotropic crystal by an amplitude–phase grating excited by an acoustic wave. The noncollinear AOF is schematically shown in Fig. 1.

A paratellurite (TeO_2) single crystal (*1*) is used as the acousto-optical crystal. The unique set of optical, acoustic, and photoelastic constants makes this material most promising for designing spectral image processing devices. A shear acoustic wave is generated by a lithium niobate ($LiNbO_3$) piezoelectric transducer *(2)*. Because of the strong acoustic anisotropy, there is a drift in the group speed of sound relative to the normal to the phase acoustic front. The running acoustic wave is absorbed by an acoustic damper (*3*). The light beam (*4*) falls normally on the entrance face of the filter. The light polarization is shown in Fig. 1. The filtered light beam (*5*) has an orthogonal polarization (extraordinary ray) and emerges from the crystal at an angle of 7° relative to the propagation direction of the zero-order light beam (*6*). The light with a direct polarization (ordinary ray) is also diffracted but is deflected to the other side of the zero-order light beam (not shown in

Fig. 1), which makes polarization analysis of the images possible. The AOF case also encloses a system for electrical impedance matching of the transducer with a standard 50-Ω circuit of the control electronic system and a temperature sensor for the electronic tracking system of spectral filter tuning temperature compensation.

The basic optical and electrical parameters of the filter are the following.

Acousto-optical material	Paratellurite
Type of acousto-optical interaction	Noncollinear wide-angle
Optical aperture	15 × 15 mm
Angular filter aperture	7°
Spectral range	6300–11 000 Å
Pass bandwidth (FWHM) at λ6365 Å	12 Å
Range of control frequencies	67–133 MHz
Control power at λ6365 Å	1.7 W
Efficiency for linear polarization	80%
Input resistance in the range of control frequencies	50 Ω
Spatial resolution	Less than 1″

The angular filter aperture is the solid angle of incidence of the light within which the filter pass band changes only slightly.

A distinctive feature of the designed filter is that with it, the diffracted beam preserves the direction of the incident light beam. The filter exit face makes an angle of 4.3° with the entrance face. In this case, the filtered beam after its refraction on the exit face propagates collinearly with the incident beam. This design feature of the filter allows the device to be easily built into a standard optical measuring system of a telescope. In addition, the spectral image displacement on the CCD array at different wavelengths is partly compensated (Voloshinov and Mironov 1989). The filter can be used with any Cassegrain telescope with typical $f/10$—$f/20$ with a CCD array of the corresponding sizes.

The filter is characterized by a combination of high spatial and spectral resolutions together with a large field of view, which allows extended objects with small-scale features to be observed. The filter does not require the use of additional optical elements. The diffracted working ray (extraordinary polarization) is coaxial with the incident beam. The residual light beam, the zero-order ray, is deflected through an angle of 7°. Since the light incident on the filter is generally not polarized, there is a second diffracted ray (ordinary polarization) produced by the orthogonal input polarization. It is also deflected through 7° relative to zero order but in a different direction.

Discrete resistive acoustic-field apodization was used in the filter for the first time, which allowed the level of spurious side maxima of the transfer function to be reduced to −17 dB. Resistive apodization leads to peculiarities of the transducer electrical impedance matching. A phenomenological electrical matching method (Molchanov and Makarov 1999) was used

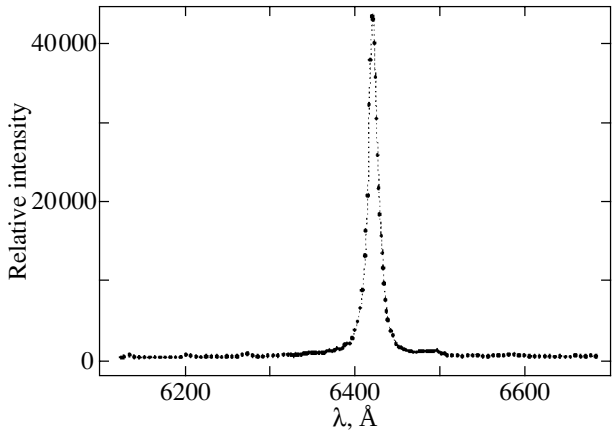

Fig. 2. AOF spectral transmission at λ6431 Å. The acousto-optical interaction frequency is 130 MHz.

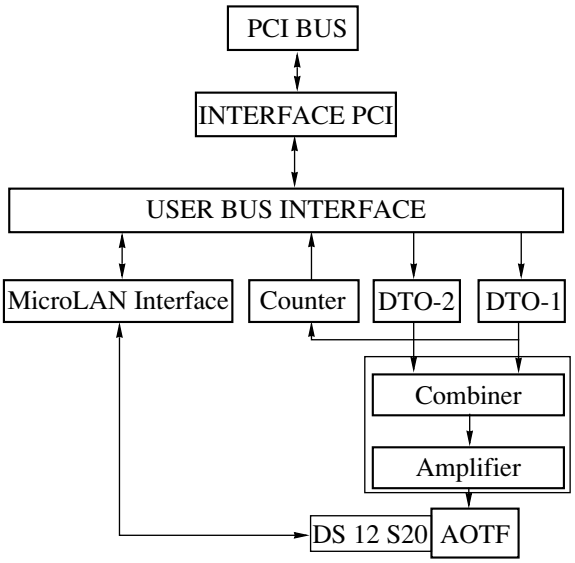

Fig. 3. A flowchart of the electronic AOF control system (see text for description).

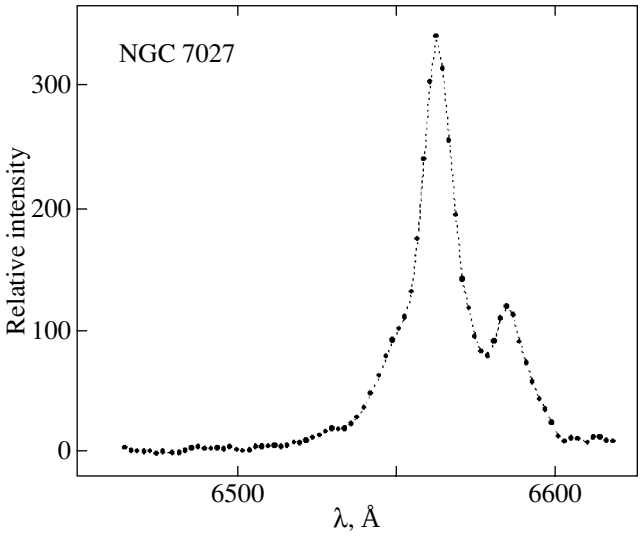

Fig. 4. The Hα (λ6563 Å) line in the planetary nebula NGC 7027: peaks on the right correspond to the [N II] λ6584 Å and the small hump on the left corresponds to [N II] λ6548 Å lines.

for the matching. After appropriate modification, this method proved to be also efficient in this case. The filter piezoelectric transducer impedance with resistive apodization was matched in a frequency range exceeding an octave: 65–140 MHz with an SWR no worse than 2.5.

The filter spectral transmission curve at λ6431 Å obtained in the laboratory by direct measurements with a while-light source is shown in Fig. 2. The filter pass bandwidth at half maximum (FWHM) is 12 Å.

The Electronic AOF Control System

A flowchart of the electronic AOF control device is shown in Fig. 3. The device is made of two separate modules. The controller card complies with the PCI bus standard and can be plugged into any free PCI slot. The high-frequency power amplifier is placed in the CD-ROM case and is located in one of the corresponding compartments in the PC cabinet. The controller card interface with the PCI bus of the PC and with the card internal bus is implemented on PLIC (programmable logical integrated circuits). These chips are ISP devices, which allows the control card to be easily reconfigured during its exploitation for a broad range of possible uses of the acousto-optical tunable filter (AOTF). A frequency grid for AOF control is generated by a digitally tunable oscillator (DTO). Fourteen of the 32 accessible bus bits are used for frequency control. This allows 16 384 frequencies to be generated. The same 14 bits (in the DTO module, different registers and control channels for frequencies and amplitudes) are used to control the output oscillator amplitude, which yields a depth of the output signal control in amplitude of no less than −55 dB.

To control the AOF temperature and temperature drifts in DTO frequency, circuits for controlling the AOF temperature and the output frequency of one of the DTO channels were introduced in the device. The remaining 18 bits of the 32-bit machine word are used for transmitting this information and for generating housekeeping information for controlling the sequence of this type of transmission. The acousto-optical cell temperature is controlled by a DS18S20 sensor over a single-wire line (the MicroLAN standard).

The software for the controller card includes a library (DLL) program for working with the card in the WINDOWS 95/98 operating environment and an interface for work with the telescope. The software can be easily upgraded to specific consumer requirements.

The controller card in the instrumentation at the observatory can operate in various modes:

selective observation of the chosen spectral region;

scanning of the chosen spectral region with various exposure times;

selective observation of two chosen spectral regions.

The presence of two control channels makes it possible to set two working wavelengths (e.g., an emission line and continuum) that are switched by the computer.

OBSERVATIONS

We tested the imaging spectrophotometer with ST-6 and ST-8 SBIG CCD cameras. We observed a planetary nebula, a star, Saturn, and the Seyfert galaxy NGC 1068. The observations were carried out at the Cassegrain focus of a 60-cm (Zeiss-600) telescope; the filter was placed in a convergent beam (1 : 12.5) without any additional optics at such a distance from the detector that the zero-order ray definitely did not fall on the detector. The detector was an ST-6 CCD camera (375 × 241 pixels, sensitivity 6.7 ph/ADU). The pixel size was 23 × 27 μm, which corresponds to $0''.6 \times 0''.7$. The observations on August 18 (the Seyfert galaxy NGC 1068) were carried out with the ST-8 CCD camera (765 × 510 pixels, 18 × 18 μm). We set the following objectives: to determine the resolution of the spectrophotometer with an AOF; to obtain the filter transmission profile for comparison with the laboratory profile; to determine the possible optical distortions introduced by the filter; and to perform test observations of AGNs with various redshifts.

The Planetary Nebula NGC 7027

First, we observed the planetary nebula NGC 7027 near the Hα emission line. Since the Hα width in this nebula is ~0.3 Å (15 km s^{-1}), the filter transmission profile is recorded almost completely. The nebula NGC 7027 is most suitable for this purpose: this is one of the brightest star-like nebulae, $18'' \times 11''$ in size, with the central star being fainter than 16^m (see, e.g., Kostyakova 1982).

Figure 4 shows the Hα region scanned at 2-Å steps. Each exposure was 2 min long, with the average background (moonless sky) being 17.9 ± 0.3 counts per pixel (ADU); the rms deviation was 2.5. The minimum flux, the mean in the λ6470–6480 Å continuum, was 1.8 ± 0.8 ADU. The line width, i.e., the filter pass bandwidth, was FWHM = 14 Å, which corresponds to the laboratory measurements (Fig. 2). We clearly see the forbidden nitrogen ([N II]) line to the right from Hα; there is also a hint of the nitrogen line on the left. The nebula NGC 7027 was observed near the Hα line on four different nights with a temperature difference from +26 to +15°C. It turned out that there was a noticeable shift of the band as the ambient temperature changed: −0.6 Å/1°C. The subsequently performed series of laboratory measurements of the spectral temperature coefficient for the AOF in the range −40 to +20°C in a heat–cold chamber yielded the dependence −0.55 Å/1K. We introduced a temperature control system precisely after these observations (see Fig. 3). If we take into account the temperature dependence, then the instrumental filter calibration using a helium–neon laser line gives the Hα wavelength (λ6563 Å) with 1-Å accuracy.

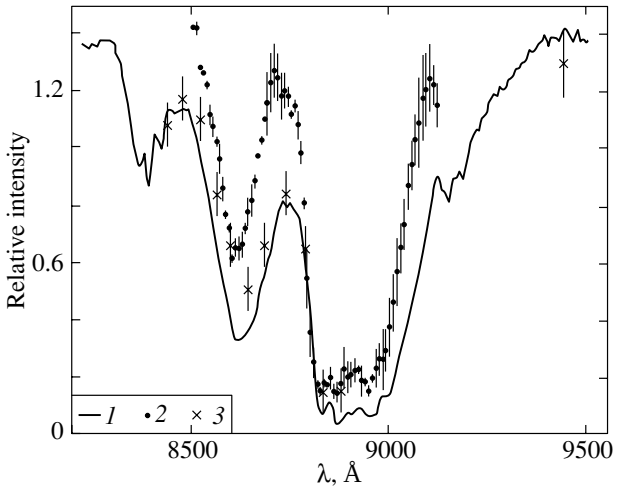

Fig. 5. (*1*) Saturn's spectrum near the methane absorption complex; (*2*) AOF observations at 10-Å steps; (*3*) observations with an acousto-optical spectrometer from Wattson *et al.* (1976).

The Star Profile

To check the possible optical distortions introduced by the tunable AOF, we obtained images of the seeing disk of the star γ Cyg (August 24, 2001). Its diameter is $2''.5$ and $1''.5$ with and without the filter, respectively. However, a different exposure could have an effect there: 20 and 0.01 s with and without the filter, respectively. Therefore, on another night (September 15, 2001), we obtained an image of Vega (α Lyr) with the AOF at λ6300 Å and without the filter but with a neutral V-band filter ($\lambda_{\rm eff} = 5500$ Å) in order for the exposure time to be of the same order of magnitude. It turned out that the AOF distorted the seeing disk only slightly: the diameter of the star seeing disk is 2.5 ± 0.1 arcsec with the AOF and 2.1 ± 0.2 arcsec with the neutral filter.

Saturn

Whereas we observed the planetary nebula NGC 7027 in an effort to obtain the filter spectral profile, Saturn's observations in the methane absorption band show the potentialities of the acousto-optical imaging spectrophotometer itself. The observations of Saturn were carried out on September 15. We took 73 frames with an exposure time of 10 s in the wavelength range 8500–9120 Å at 10-Å steps. The planetary disk center was measured with a ~6″

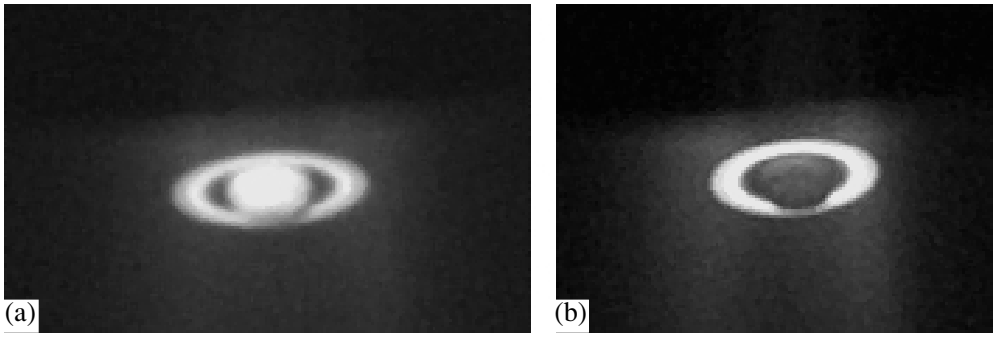

Fig. 6. Saturn's images at (a) λ8500 and (b) λ8870 Å obtained with the acousto-optical imaging spectrophotometer on September 15, 2001.

aperture relative to the eastern and western edges of the ring (we took a mean). The sky background was also measured near the eastern and western edges of the ring. The results are shown in Fig. 5 (*2*). Also shown for comparison are the observations by Wattson *et al.* (1976) (*3*) and Saturn's spectrum from Trafton (1975) (*1*). The calibration was performed using the minimum of the main 8800–9000 Å absorption band. Since all (not only our) measurements were made relative to the ring, they can be compared. Note that the blue edge of the third (deepest) band matches both the spectrum and the measurements by Wattson *et al.* (1976). However, the red edge differs markedly; as a result, the band proves to be narrower (approximately by 50 Å). The second band (~8600 Å) proved to be even narrower, although its blue edge, according to our measurements, matches the data by Wattson *et al.* (1976). The band intensities are also different, but here inaccurate calibration in the vertical direction may have an effect. Wattson *et al.* (1976) only pointed out that they measured the planetary disk relative to the ring, while Trafton (1975) measured Saturn's spectrum relative to the eastern edge of the ring. Nevertheless, it may be argued that at least the band width varies with time, with the variability being most likely long-term. The differences between the spectrum taken by Watsson *et al.* (1976) in January 1975 and the spectrum by Trafton (1975) (January 1973) are much smaller than those between the former and our spectrum (September 2001). As was noted above, the filter pass band in Wattson *et al.* (1975) is approximately the same as our pass band; i.e., the spectral resolutions are approximately identical. The spectral resolution in Trafton (1975) is slightly higher, 9 Å.

As an example, Fig. 6 shows Saturn's images obtained with the AOF at λ8500 Å and in the methane λ8870 Å absorption band. We can note the fairly high image quality provided by the filter. Saturn's ring shines as reflected light from the Sun and its brightness depends little on wavelength. The atmosphere of the giant planet consists mainly of methane, and Saturn's brightness in the methane absorption band decreases by almost an order of magnitude.

Seyfert Galaxies

Since our subsequent objective was to study emission-line variability in peculiar objects (Seyfert galaxies, quasars, Be stars, etc.), we attempted to obtain an Hα image of the nucleus of the Seyfert galaxy NGC 7469 (redshift $z = 0.0167$, the V magnitude through a 27″ aperture is $V_{27} = 12^m.8$) and a brighter galaxy, NGC 1068 ($z = 0.0036$, $V_{27} = 10^m.3$). With a 60-cm telescope, the nucleus of the Seyfert galaxy NGC 7469 is poorly seen in the Hα emission line: the signal-to-noise ratio is less than 5; i.e., the emission line can be recorded with confidence, but the measurement accuracy is too low to investigate its variability. The line intensity in the nucleus of NGC 1068 can be measured with a satisfactory accuracy, but this object is of little interest because of its low variability amplitude. Since in this case our objective was just to detect the line, the scanning was made at 25-Å steps. Nevertheless, it turned out that the measured peak of the Hα line almost exactly corresponds to the galaxy redshift. A larger telescope is required to observe fainter objects.

DISCUSSION

This astronomical study is the first in Russia to be performed with a fundamentally new instrument, an acousto-optical tunable imaging spectrophotometer. Its serves only as a demonstration, because at this stage, the goal set is to study the filter potentialities. Our observations with the tunable AOF showed

that the AOF is an almost ideal device for studying emission-line variability in peculiar objects. As was pointed out in the Introduction, the AOF surpasses the interference filters in all parameters. Observational experience indicates that the photometer mode rather than spectrograph mode is best suited to studying the variability of astrophysical objects, including emission-line intensity variability. In the photometer mode, variability observations are carried out according to the standard scheme: comparison star (local standard), sky background, the object being measured, comparison star, sky background. Since the comparison star is always chosen near the object, this scheme allows the effect of atmospheric transparency to be eliminated, and a double measurement of the standard allows it to be interpolated to the measurement time of the variable object. From this point of view, using a CCD detector is preferred, because the object, comparison star, and sky background can be recorded simultaneously. However, it is not always possible to find a sufficiently bright comparison star that will be close enough to the object under study for them to fall within one CCD frame (the comparison star must be much brighter than the variable object in order to reduce the measurement errors).

The investigate of emission-line variability necessarily requires continuum measurements near the line, because the continuum is also variable in peculiar objects. By measuring the flux in the "line + continuum" and separately in the continuum, we can determine the intensity of the line itself. Here, an AOF with two-channel control has a clear advantage: by using electronic (computer) switching, we can pass from the emission-line region to the continuum region and back.

The second advantage is the possibility of observing objects with various redshifts (quasars, Seyfert galaxies). The redshifts of the nearest Seyfert galaxies are $z = 0.003$–0.070, which corresponds to 20–450 Å for the Hα line. For one of the nearest and brightest quasars, 3C 273 ($z = 0.16$), the Hα line is redshifted approximately by 1000 Å. It may be for this reason (large shift) that the Hα variability has not yet been studied in quasars.

The third advantage is high transparency: the filter transmission at maximum can reach 80–90%, which is unattainable for any spectrograph. Given that the AOF can operate both in scanning mode and in discrete arbitrary spectral sampling mode, its advantages in comparison with a spectrograph or a spectrophotometer with a dispersing element (e.g., a diffraction grating) are obvious.

Here, we describe observations made with an imaging spectrophotometer and a CCD detector. In most cases, however, it is not necessary to have an image of the object. In particular, for point sources (stars, quasars), it will suffice to simply measure the line and continuum fluxes. In that case, a photon-counting photomultiplier can be used as the detector. The flux can then be immediately obtained in digital form. The currently available photomultipliers are comparable in quantum efficiency to CCDs. For extended objects (planets, nebulae), imaging in a particular line can be of interest (see Fig. 6).

CONCLUSIONS

At present, an operational imaging spectrophotometer with the AOF described here and with an ST-6 CCD camera is available at the Crimean Laboratory of the Sternberg Astronomical Institute. The spectrophotometer was tested on a 60-cm telescope (1 : 12.5). However, even this focal length (7500 cm) proved to be too large for the CCD; the optimal focal length would be 250–300 cm (maximum signal-to-noise ratio). The efficiency of the CCD camera at the Cassegrain focus of a 125-cm telescope will be even lower. On the other hand, the AOF performs poorly in a highly convergent beam (1 : 4 or 1 : 5). Here, we see two ways out:

(1) to use additional optics, a focal reducer, in front of the CCD;

(2) to use a photomultiplier as the photodetector.

Which of these alternatives is to be chosen will be determined by the goal of the investigation, to study emission-line variability or to image an extended object in a line.

ACKNOWLEDGMENTS

We wish to thank A.I. Kolesnikov and I.V. Terent'ev from the Tver State University and the Pribor Research and Production Company (Tver) for the synthesis of large single paratellurite crystals of high optical quality for the AOF of the spectrophotometer. We are also grateful to S.I. Chizhikov, Director of the Acousto-Optical Research Center, for the helpful discussions, and to V.V. Ivanov, head of the Optical Department at the Lebedev Physical Institute (Russian Academy of Sciences), for the organization of and help in carrying out climatic tests of the AOF.

This work was supported in part by the Russian Foundation for Basic Research, project nos. 01-07-90448 and 02-07-90448.

REFERENCES

1. V. I. Balakshii, V. N. Parygin, and L. E. Chirkov, *Physical Principles of Acousto-Optics* (Radio i Svyaz', Moscow, 1985).
2. B. Bates, D. Haliwell, and D. Findlay, Appl. Opt. **23**, 257 (1984a).
3. B. Bates, D. Findlay, and D. Halliwell, Proc. SPIE **369**, 315 (1984b).
4. I. C. Chang, Proc. SPIE **90**, 12 (1976).
5. I. C. Chang, Opt. Eng. **20**, 824 (1981).
6. A. M. Cherepashchuk and V. M. Lyutyi, Astrophys. Lett. **13**, 165 (1973).
7. C. M. Gaskell and L. S. Spark, Astrophys. J. **305**, 175 (1986).
8. M. S. Gottlieb, in *Design and Fabrication of Acousto-optic Devices,* Ed. by A. P. Goutzoulis and D. R. Pape (Marcel Dekker, New York, 1994).
9. E. B. Kostyakova, *Physics of Planetary Nebulas* (Nauka, Moscow, 1982).
10. V. M. Lyuty and A. M. Cherepashchuk, Astron. Tsirk., No. 633, 1 (1971).
11. V. M. Lyuty, A. M. Cherepashchuk, and Kh. F. Khaliullin, Astron. Zh. **50**, 1105 (1973) [Sov. Astron. **17**, 701 (1973)].
12. L. N. Magdich and V. Ya. Molchanov, *Acoustooptic Devices and Their Applications* (Gordon and Breach, New York, 1989).
13. V. Ya. Molchanov, O. Yu. Makarov, and A. I. Kolesnikov, in *Technical Digest of Advances in Acousto-Optics AAO-01, Gdansk, Poland, 2001,* p. 23.
14. V. Ya. Molchanov and O. Yu. Makarov, Opt. Eng. **38**, 1127 (1999).
15. V. N. Parygin, V. B. Voloshinov, and V. Ya. Molchanov, Proc. SPIE **4353**, 17 (2001).
16. W. H. Smith, W. V. Shempp, C. P. Conner, and P. Katzka, Publ. Astron. Soc. Pac. **99**, 1337 (1987).
17. W. H. Smith and K. M. Smith, Exp. Astron. **1**, 329 (1991).
18. L. Traĭton, Astrophys. J. **195**, 805 (1975).
19. M. H. Ulrich, A. Boksenberg, G. E. Bromage, *et al.*, Mon. Not. R. Astron. Soc. **206**, 221 (1984).
20. V. B. Voloshinov and O. V. Mironov, Electron. Eng. Commun. Phys. **33**, 2177 (1988).
21. V. B. Voloshinov and N. Gupta, Proc. SPIE **3900**, 74 (1999).
22. R. B. Wattson, S. A. Rappaport, and E. E. Frederick, Icarus **27**, 417 (1976).

Translated by V. Astakhov